

UNIVERSITY OF SHEFFIELD

DOCTORAL THESIS

---

**Rapid Analysis of Backfilled Masonry  
Arch Bridges**

---

*Author:*  
Qi DANG

*Supervisors:*  
Prof. Matthew GILBERT  
Dr. Colin C. SMITH

*A thesis submitted in fulfillment of the requirements  
for the degree of Doctor of Philosophy*

*in the*

Computational Mechanics and Design Research Group  
Geotechnical Engineering Research Group  
Department of Civil and Structural Engineering

June 28, 2021



## Declaration of Authorship

I, Qi DANG, declare that this thesis titled, 'Rapid Analysis of Backfilled Masonry Arch Bridges' and the work presented in it are my own. I confirm that:

- This work was done wholly or mainly while in candidature for a research degree at the University of Sheffield.
- Where any part of this thesis has previously been submitted for a degree or any other qualification at the University of Sheffield or any other institution, this has been clearly stated.
- Where I have consulted the published work of others, this is always clearly attributed.
- Where I have quoted from the work of others, the source is always given. With the exception of such quotations, this thesis is entirely my own work.
- I have acknowledged all main sources of help.
- Where the thesis is based on work done by myself jointly with others, I have made clear exactly what was done by others and what I have contributed myself.

Signed:

---

Date:

---



## *Abstract*

This thesis presents analysis methods designed to rapidly estimate the load-carrying capacity of backfilled masonry arches. To help engineers to analyse backfilled masonry arches, various methods exist. However, some of these are over-simplified; others are in contrast very complicated and time consuming for engineers to master. In industry simple, accurate, and rapid methods are potentially very useful. Thus the development of such methods has been the main focus of this thesis.

One available numerical strategy is computational limit analysis. Limit analysis is a method that can obtain the failure load without the need to carry out an iterative elastic-plastic analysis. Limit analysis theorems are employed to obtain upper- and lower-bounds on the collapse load. Discontinuity layout optimization (DLO) is a limit analysis procedure that can be used to determine the critical layout of discontinuities and associated upper-bound limit load for plane plasticity problems. However, the computational cost of DLO can be quite high. In order to address this, a fast running DLO procedure is proposed. For lower-bound analysis, a soil-fill stress field model is proposed. In this model the Mohr-Coulomb criterion is strictly obeyed in the stress field in the backfilled masonry arches. Both literature benchmark problems and backfilled masonry arch bridge problems are solved to show the efficacy of the upper- and lower-bound methods.

Another strategy is limit equilibrium. The limit equilibrium method has been used to obtain approximate solutions for stability problems. The method is usually considered as an approximate means of constructing a slip-line field. Differential planar soil elements are proposed here to simulate concave or convex arching effects in the retained soil backfill around arch barrels. An anisotropic stress distribution is applied to model the backfill material that in reality is often heterogeneous in nature. In this method, equilibrium considerations can be used to solve the masonry arch bridge problems by simple static methods. A number of examples from the literature and industry are analysed to demonstrate the efficacy of the limit equilibrium method.

The choice of method is dependent on the principal goal of the assessment. To balance degree of accuracy and computational cost, the proposed rapid analysis strategies have been designed to provide a simple and fast means of assessing bridge load-carrying capacity. The upper- and lower-bound strategies provide rigorous solutions, but sometimes underestimate the bridge load-carrying capacity especially of the weak backfill strength. The limit equilibrium strategy provides approximate solutions which could address this issue.



## *Acknowledgements*

I would like to thank all those who have helped me undertake the research presented in this thesis. I would particularly like to thank my supervisors, Matthew Gilbert and Colin C. Smith, for the invaluable guidance, support and encouragement provided throughout the various stages of this work. I would also like to thank members of the Computational Mechanics & Design and Geotechnical Engineering research groups for their companionship and friendship over the last few years.

I would also like to thank my friends and family for their support and encouragement over so many years. In particular my mother, Shu-ping Li, who supported me through school and university, providing me the opportunity to undertake this research.



# Contents

<b>Declaration of Authorship</b>	<b>iii</b>
<b>Abstract</b>	<b>v</b>
<b>Acknowledgements</b>	<b>vii</b>
<b>I Introduction</b>	<b>1</b>
<b>1 Introduction</b>	<b>3</b>
1.1 Background . . . . .	3
1.2 Motivation and Objectives . . . . .	5
1.3 Structure of the Thesis . . . . .	6
<b>2 Literature Review</b>	<b>7</b>
2.1 Bridge Construction Materials and Behaviour . . . . .	7
2.1.1 Construction Materials . . . . .	7
2.1.2 Bridge Makeup . . . . .	8
2.1.3 Bridge Behaviour . . . . .	10
2.2 Theoretical Basis . . . . .	13
2.2.1 Perfectly Plastic Assumption . . . . .	13
2.2.2 Equilibrium Condition Based on Stresses . . . . .	14
2.2.3 Mohr-Coulomb Yield Condition . . . . .	15
2.2.4 Mechanism Condition Based on Thrust Line . . . . .	16
2.2.5 Limit Analysis Method . . . . .	17
2.2.6 Limit Equilibrium Method . . . . .	17
2.3 Analysis Methods . . . . .	18
2.3.1 Linear-elastic analysis . . . . .	18
2.3.2 Plastic limit analysis . . . . .	19
2.3.3 Other analysis methods . . . . .	23
2.3.4 Choosing a Suitable Analysis Method . . . . .	24
2.4 Laboratory and Field Tests on Masonry Arch Bridges . . . . .	24
2.4.1 Bolton arch bridge . . . . .	25
2.4.2 Salford arch bridge . . . . .	26
2.4.3 Bridgemill arch bridge . . . . .	27
2.4.4 Discontinuity Layout Optimization Modelling . . . . .	28

2.5	Knowledge Gaps . . . . .	32
<b>II</b>	<b>Numerical Strategies</b>	<b>33</b>
<b>3</b>	<b>Computationally Efficient Upper Bound Method</b>	<b>35</b>
3.1	Introduction . . . . .	36
3.2	Comparison of LimitState:GEO and LimitState:RING . . . . .	36
3.2.1	Arch Barrel Model . . . . .	36
3.2.2	Backfill Model . . . . .	38
3.2.3	Commentary . . . . .	39
3.3	Fast Running Discontinuity Layout Optimization . . . . .	40
3.3.1	Simple Example . . . . .	41
3.3.2	Typical Example of Backfilled Masonry Arch Bridge . . . . .	43
3.4	Application to Case Studies . . . . .	44
3.5	Discussion . . . . .	48
3.6	Concluding Remarks . . . . .	50
<b>4</b>	<b>Lower Bound Stress Fields Method</b>	<b>51</b>
4.1	Introduction . . . . .	52
4.2	Masonry Stress Fields . . . . .	52
4.3	Soil Stress Fields . . . . .	56
4.3.1	Introduction . . . . .	56
4.3.2	Stress Fields Due to Surface Load . . . . .	57
4.3.3	Stress Fields Due to Fill Self Weight . . . . .	61
4.3.4	Combined Stress Fields . . . . .	61
4.3.5	Yield Constraints . . . . .	62
4.3.6	Determination of Lower Bound Stress Fields . . . . .	70
4.3.7	Iterative Procedure . . . . .	76
4.4	Application to Case Studies . . . . .	78
4.5	Discussion . . . . .	82
4.6	Concluding Remarks . . . . .	83
<b>5</b>	<b>Rational Limit Equilibrium Method</b>	<b>85</b>
5.1	Introduction . . . . .	86
5.2	Anisotropic Stresses Due to Surface Load . . . . .	86
5.3	Soil Earth Pressures of Masonry Arch Bridge . . . . .	89
5.3.1	Assumptions . . . . .	89
5.3.2	Active Earth Pressures Against Rigid Wall . . . . .	91
5.3.3	Passive Earth Pressures Against Rigid Wall . . . . .	97
5.3.4	Simple Example of Rigid Embedded Cantilever Retaining Wall . . . . .	101
5.3.5	Simple Example of Backfilled Masonry Arch Bridge . . . . .	103
5.4	Application to Case Studies . . . . .	105
5.5	Discussion . . . . .	106

5.6	Concluding Remarks . . . . .	110
<b>III</b>	<b>Discussion</b>	<b>111</b>
<b>6</b>	<b>Discussion</b>	<b>113</b>
6.1	Introduction . . . . .	113
6.2	Issues in Soil Earth Pressures . . . . .	113
6.3	Issues in Complex Masonry Arch Bridge Failure Mechanisms . . . . .	115
<b>IV</b>	<b>Conclusions and Recommendations</b>	<b>117</b>
<b>7</b>	<b>Conclusions and Recommendations</b>	<b>119</b>
7.1	Conclusions . . . . .	119
7.2	Recommendations of Future Work . . . . .	120
	<b>References</b>	<b>122</b>
	<b>Appendices</b>	<b>129</b>
<b>A</b>	<b>Formulations in Rigid-Block Limit Analysis</b>	<b>131</b>
A.1	Joint Equilibrium Formulation . . . . .	131
A.2	Including Finite Masonry Material Strength . . . . .	133
A.3	Limiting Horizontal Fill Stresses . . . . .	134
<b>B</b>	<b>Formulations in Discontinuity Layout Optimization</b>	<b>137</b>
B.1	Primal Problem . . . . .	137
B.2	Dual Problem . . . . .	140
<b>C</b>	<b>Formulations in Anisotropic Stress Distribution</b>	<b>143</b>
<b>D</b>	<b>Formulations in Lateral Earth Pressure Coefficient</b>	<b>151</b>



# List of Figures

1.1	Main elements of masonry arch bridges . . . . .	4
2.1	Masonry under uniaxial compression . . . . .	8
2.2	Typical bonding patterns . . . . .	9
2.3	Diagram of abutments . . . . .	9
2.4	Internal spandrel walls of London Road Brighton viaduct . . . . .	10
2.5	Arch geometries . . . . .	11
2.6	Robert Hooke's hanging chain . . . . .	11
2.7	Four hinged failure mechanism of a masonry arch bridge . . . . .	12
2.8	Perfectly plastic assumption . . . . .	13
2.9	Diagrams illustrating equilibrium condition . . . . .	15
2.10	Mohr-Coulomb yield surface . . . . .	16
2.11	Failure mechanisms . . . . .	16
2.12	Linear-elastic analysis of a single span . . . . .	18
2.13	thrust line . . . . .	19
2.14	Block $j$ and contact forces for interface $i$ . . . . .	21
2.15	DLO output for a sample of masonry arch bridge . . . . .	21
2.16	Non-linear yield constraints for contact surface . . . . .	22
2.17	The deformed shape of masonry arch bridges . . . . .	23
2.18	Geometry of Bolton arch bridge . . . . .	25
2.19	Geometry of Salford arch bridge . . . . .	26
2.20	Geometry of Bridgemill arch . . . . .	27
2.21	Four hinged failure mechanisms . . . . .	28
2.22	Geometrical model of Salford arch bridge . . . . .	29
2.23	Applied load against deformation at the quarter-span of Salford arch bridge . . . . .	30
2.24	Four hinged failure mechanism . . . . .	30
2.25	DLO model of Bolton arch bridge . . . . .	31
2.26	DLO model of Bridgemill arch bridge . . . . .	31
3.1	Arch barrel modelling in DLO . . . . .	37
3.2	Arch barrel modelling in rigid-block analysis . . . . .	37
3.3	Backfilled arch bridge modelling in DLO . . . . .	38
3.4	Soil model in rigid-block analysis . . . . .	39

3.5	CPU time comparison between 'DLO-standard' and rigid-block analysis results . . . . .	39
3.6	Stages in the DLO procedure . . . . .	40
3.7	Analogy between standard and fast DLO . . . . .	41
3.8	Hodograph and Maxwell force diagrams . . . . .	42
3.9	Backfilled arch bridge modelling in DLO-edge . . . . .	42
3.10	Number of nodes used vs. percentage error when using standard DLO and fast DLO . . . . .	43
3.11	CPU time of DLO-standard and DLO-edge and rigid-block analysis . . . . .	44
3.12	Load-carrying capacity at different load position . . . . .	47
3.13	Failure mechanisms of bridge which had free abutments . . . . .	49
3.14	Collapse load vs. load position/span . . . . .	50
4.1	Contact stress distribution . . . . .	53
4.2	Example of an arch barrel . . . . .	55
4.3	Lower bound stress fields due to live load . . . . .	56
4.4	Lower bound stress fields due to dead load . . . . .	56
4.5	Cross section through long flexible strip on infinite soil . . . . .	57
4.6	Contours of $\Delta p/q$ . . . . .	59
4.7	Contours of $\Delta s/q$ . . . . .	60
4.8	Diagrams illustrating equilibrium for soil stress fields . . . . .	61
4.9	Mohr stress diagrams of cohesive only and cohesive soil . . . . .	64
4.10	Example of footing . . . . .	65
4.11	Contours of mobilised friction $\sin \phi_m$ with $n = 1.0$ and $q/\gamma B = 10$ , $K = 1$ . . . . .	65
4.12	Superposition of initial and induced stresses in ideal soil . . . . .	66
4.13	Surface load at cemented layer $S_C$ . . . . .	67
4.14	Required lateral earth pressure coefficients with $q/\gamma B = 10$ at depths . . . . .	70
4.15	Lateral variation of $K_{min}$ and $K_{max}$ for $n = 1.0$ and $q/\gamma B = 10$ at depths . . . . .	71
4.16	Lateral variation of $K_{min}$ and $K_{max}$ for $n = 0.5$ and $q/\gamma B = 10$ at depths . . . . .	72
4.17	Lateral variation of $K_{min}$ and $K_{max}$ for $n = 2.0$ and $q/\gamma B = 10$ at depths . . . . .	73
4.18	Contours of mobilised friction $\sin \phi_m$ with $q/\gamma B = 10$ and $c/\gamma B = 0$ . . . . .	74
4.19	Contours of mobilised friction $\sin \phi_e$ with $q/\gamma B = 10$ and $c/\gamma B = 0.2$ . . . . .	75
4.20	Vertical stress distribution at depth B . . . . .	76
4.21	Iterative flow chart . . . . .	77
4.22	CPU time of DLO-normal and DLO-fast and lower-bound stress fields . . . . .	78
4.23	Parametric study of lower bound solutions for Bolton arch bridge . . . . .	79
4.24	Parametric study of lower bound solutions for Salford arch bridge . . . . .	80
4.25	Parametric study of lower bound solutions for Bridgemill arch bridge . . . . .	81
5.1	Cross section through long flexible strip on infinite soil carrying surcharges . . . . .	87
5.2	Contours of $\Delta \sigma_z/q$ . . . . .	88
5.3	PIV soil kinematics for a typical bridge test . . . . .	89

5.4	Vertical stress distribution for live load . . . . .	89
5.5	Finite planar elements for soil-fill . . . . .	90
5.6	Soil arching effect . . . . .	90
5.7	Concave arch analysis . . . . .	91
5.8	Mohr-circle for stresses at active retaining wall . . . . .	92
5.9	Force equilibrium analysis in active zone . . . . .	94
5.10	Parametric study for active retaining wall . . . . .	96
5.11	Soil wedge analysis . . . . .	97
5.12	Parametric study for passive retaining wall . . . . .	100
5.13	A simple example of embedded cantilever wall . . . . .	102
5.14	A simple example of masonry arch bridge . . . . .	104
5.15	CPU time of DLO-standard and DLO-edge and lower-bound stress fields and limit equilibrium . . . . .	105
5.16	Parametric study of limit equilibrium solutions for Bolton arch bridge	107
5.17	Parametric study of limit equilibrium solutions for Salford arch bridge	108
5.18	Parametric study of limit equilibrium solutions for Bridgemill arch bridge . . . . .	109
6.1	Geometrical model of a sample of masonry arch bridge with fixed abutments . . . . .	114
6.2	Failure mechanisms of a sample of masonry arch bridge with fixed abutments . . . . .	115
6.3	Stress distributions on extrados of masonry arch bridge with cohe- sionless backfill . . . . .	116
A.1	Block and contact forces . . . . .	132
A.2	Contact surface moment vs. normal force failure envelopes . . . . .	133
A.3	Stresses acting on extrados of a voussoir subject to backfill pressures .	134
B.1	Discontinuity relative displacements . . . . .	138
B.2	Discontinuity forces in equilibrium with equivalent nodal forces (no external load) . . . . .	141
C.1	Applied load and coordinates . . . . .	143



# List of Tables

2.1	Applicability of analysis methods . . . . .	24
2.2	Material properties of Bolton arch bridge . . . . .	25
2.3	Material properties of Salford arch . . . . .	26
2.4	Material properties of Bridgemill arch . . . . .	27
3.1	Influence of number of using nodes . . . . .	43
3.2	Comparison of DLO-standard and DLO-edge in bridges (5000 nodes used in DLO-standard, 1500 nodes used in DLO-edge) . . . . .	45
3.3	Comparison of DLO-edge and rigid-block analysis in bridges (1500 nodes used in DLO-edge) . . . . .	45
3.4	DLO-standard and DLO-edge solution of bridges ( $P$ is a unit load) . .	46
4.1	Results of an arch barrel . . . . .	55
5.1	Comparison of theory and DLO results for the embedded cantilever retaining wall with $\delta = 0$ . . . . .	102
5.2	Comparison of theory and DLO results for the embedded cantilever retaining wall with $\delta = 0.33\phi$ . . . . .	102
5.3	Comparison of theory and DLO results for the masonry arch bridge . .	104
6.1	Main material parameters of a masonry arch bridge . . . . .	114



# List of Symbols

$c$	drained cohesion	$\text{kN/m}^3$
$c_u$	undrained cohesion	$\text{kN/m}^3$
$c_C$	required cohesion	$\text{kN/m}^3$
$\phi$	angle of friction	degree
$\phi_e$	equivalent angle of friction	degree
$\delta$	angle of soil-arch interface friction	degree
$\gamma$	unit weight of material	$\text{kN/m}^3$
$z$	stress field depth	m
$\sigma_{\text{crush}}$	crushing compressive strength	$\text{N/mm}^2$
$\sigma$	normal stress	$\text{kN/m}^2$
$\tau$	shear stress	$\text{kN/m}^2$
$S$	shear force	kN
$N$	normal force	kN
$M$	moment	$\text{kN m}$
$t$	thickness of voussoir	mm
$d$	effective thickness of voussoir	mm
$I$	second moment of area	$\text{m}^4$
$E$	Young's modulus	$\text{kN/m}^2$
$q$	uniformly distributed load	$\text{kN/m}$
$\Delta\sigma$	incremental stress from strip load	$\text{kN/m}$
$B$	width of loading beam	m
$S_C$	cemented layer depth	m
$H$	height of retaining wall	m



## **Part I**

# **Introduction**



## Chapter 1

# Introduction

### 1.1 Background

Masonry arch bridges continue to form a significant part of the transportation network in the UK and many other countries. The majority of these bridges on the railway and highway network have been in service for more than 120 years (Sarhosis et al. 2016). In recent decades most of these carry traffic far heavier than they were designed for, with potential economic and environmental costs. In this situation it is important that the existing infrastructure is carefully managed. Repair and strengthening works are also needed to deal with changes in the requirements of transport systems and the gradual deterioration of existing bridges.

Although there are many variations that exist around the same structural concept, the main elements presented schematically in Figure 1.1(a) and Figure 1.1(b). The primary element of a complete masonry arch bridge is the arch barrel. Widely used arch geometries include semi-circular, pointed, segmental, parabolic and elliptical, with combinations of a number of circular segments used to achieve forms intended to optimise the structural performance of the arch and its function. Arch barrels were commonly constructed using brick units or stone voussoirs. In brickwork constructions, the arch barrel contains multi-rings of bricks with or without headers, but arch barrels without headers were especially common in the UK. In stone constructions, the arch barrel commonly comprises a single ring of large voussoirs. In order to provide a level formation, soil-fill was used above the extrados of the arch barrel. Distribution of the load from the rail or the road surface through the fill contributes to load-carrying capacity. Spandrel walls presented at the arch edges retain the soil-fill around the arch barrel and extend into the wing walls beyond the abutments.

At present a high proportion of these historical bridges show evidence of deterioration. The processes of gradual deterioration brought about by environmental effects and repeated application of applied loads are relentless and weaken the strength of the construction materials from the day of their creation. The processes are typically slow, but after long periods of time become significant and weaken the masonry elements of the structure, affecting bridge load-carrying capacity.

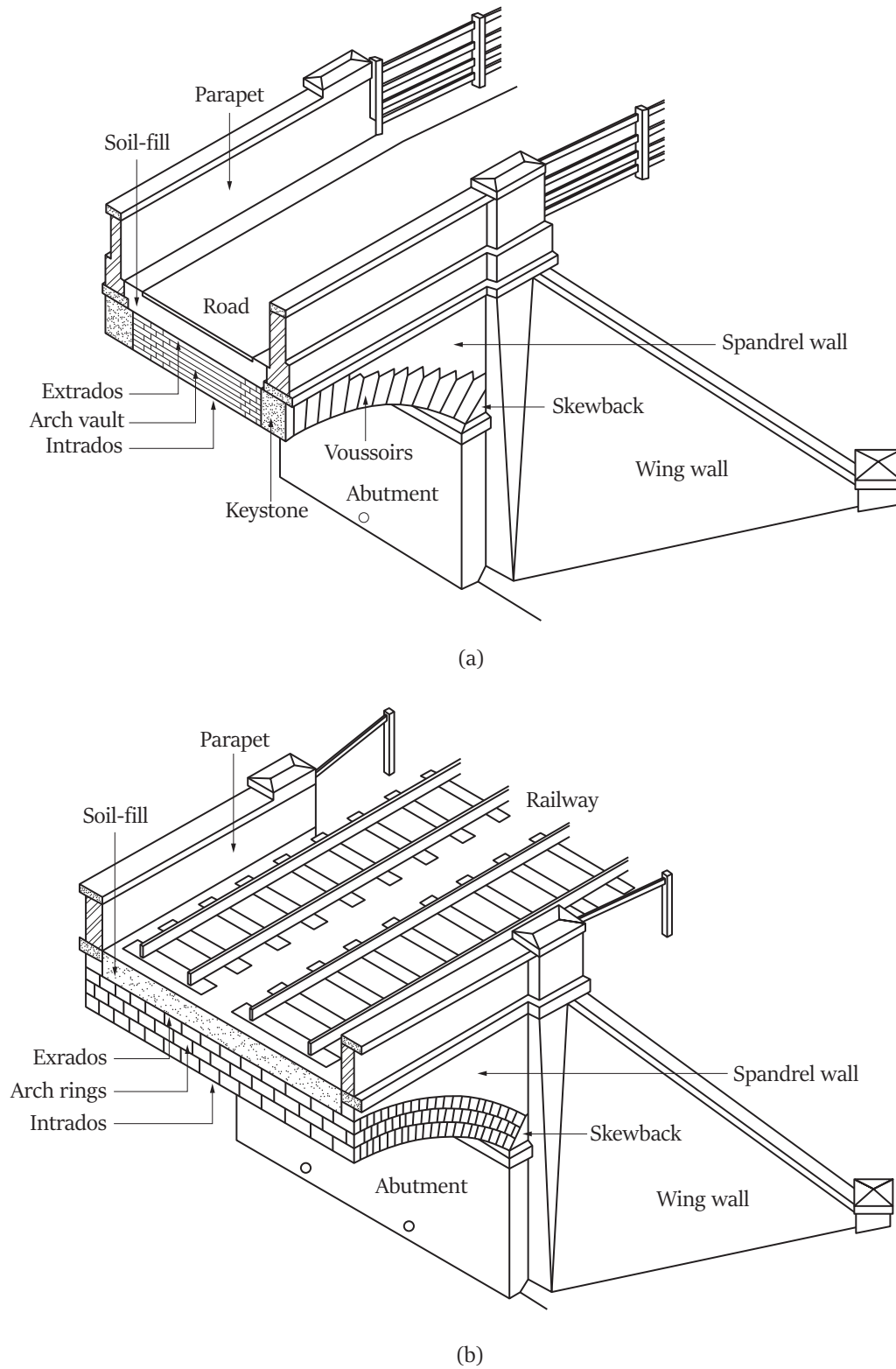


FIGURE 1.1: Main elements of masonry arch bridges: (a) highway bridge with stonework; (b) railway bridge with brickwork (after Melbourne et al. 2006)

## 1.2 Motivation and Objectives

In order to predict the in-service behaviour and load-carrying capacity of masonry arch bridges, there are various options available, ranging from empirical rules based procedures (Pippard 1948), to limit analysis based approaches (Gilbert and Melbourne 1994), to advanced non-linear computational formulations (Crisfield 1993). Selection of the most appropriate method to use is dependent on: (i) the level of accuracy desired; (ii) the material properties data; (iii) the expertise available. It can be expected that different methods will lead to different results, depending on the efficiencies of the approach and the information available. A higher level modelling approach may not always lead to a higher predicted load-carrying capacity. The approach for modelling masonry arch bridges should provide an acceptable degree of accuracy, within sustainable time and cost limits.

Most masonry arch bridges in the UK consist of an arch barrel and soil-fill above the arch extrados. The soil-fill distributes the applied load and contributes to the load-carrying capacity. Due to the importance of the soil-fill, both the constitutive model and the inputted material properties should be chosen carefully. However, current commonly used tools (e.g. Obvis 2016, LimitState 2019b) only consider self-weight, load dispersion and passive restraint effects of the soil-fill, rather than explicitly modelling the soil-fill material itself. This limits their range of application and their accuracy.

In order to directly model both masonry and soil-fill elements, a technique called discontinuity layout optimization (DLO) was proposed and its reliability was proved by comparison with experimental tests on large-scale models (Gilbert et al. 2010). However, the computational cost of DLO becomes quite high if there are many load positions to consider.

The aim of the research is to address these issues. The main objective is to develop numerical strategies for the rapid assessment of soil-filled masonry arch bridges. In order to achieve this objective, the following tasks were undertaken:

- development of a computationally efficient DLO procedure, and verification of this through application to masonry arch bridges;
- development of a lower bound stress field model, and verification of this through application to masonry arch bridges;
- development of a limit equilibrium model, and verification of this through application to masonry arch bridges.

### 1.3 Structure of the Thesis

This thesis is divided into four parts. In Part I, the motivation and goals of the research are defined and framed within the current state-of-the-art.

Chapter 2 reviews structural behaviour and discusses currently available numerical models developed for masonry arch bridges. Limit state analysis based methods for assessing the load-carrying capacity of soil-filled masonry arch bridges are reviewed, and an overview of the approaches used in this thesis is provided.

Part II presents computational strategies, namely the lower bound, limit equilibrium and upper bound methods developed in this thesis.

Chapter 3 describes the development of a simplified, computational inexpensive, DLO procedure. This is validated against literature benchmarks and compared with results obtained from carefully controlled tests carried out on soil-filled masonry arch bridges.

Chapter 4 introduces a lower bound stress field model. It outlines the assumptions of the lower bound theorem and the masonry stress fields to be satisfied to comply with the requirements of the lower bound theorem. The use of soil-fill stress fields in conjunction with rigid block limit analysis is described and the procedures for modelling global and local failure modes are explained.

Chapter 5 introduces a limit equilibrium model. It demonstrates the anisotropic effect of the soil-fill due to the surface load, describes the arching effect considered in the soil-fill, and interprets outcomes of the procedure when applied to masonry arch bridges.

Part III presents a discussion of the developed numerical models.

Chapter 6 documents case studies of applications of the upper bound, limit equilibrium and lower bound methods to estimate of the load-carrying capacity of masonry arch bridges. The limitations associated with the numerical strategies are then discussed.

In Part IV, Chapter 7 provides general conclusions and outlines future work required in this field.

## Chapter 2

# Literature Review

### 2.1 Bridge Construction Materials and Behaviour

An overview of a typical masonry arch bridge has been shown in section 1.1. Due to the absence of modern design codes and standards for materials used in construction, masonry arch bridges vary considerably in terms of geometry, structural details and construction materials. In this section, bridge construction materials and behaviour will be introduced as follows:

#### 2.1.1 Construction Materials

A masonry arch bridge was usually constructed using brick or stone masonry units and backfill. The arch barrel usually comprises masonry units separated by mortar. Backfill materials above the extrados of an arch barrel were usually granular and/or cohesive in nature.

##### Masonry materials

The term masonry describes a construction formed from brickwork or stonework. It is a composite material involving masonry units and mortar. Masonry properties are derived both from the properties of the masonry units and the properties of the mortar. Figure 2.1 shows masonry units separated by joints.

Masonry units may be brick or stone, or sometimes concrete. For brick material, the compressive strength of a locally sourced soft red brick is approx.  $10 \text{ N/mm}^2$ , whereas that of a modern engineering bricks may approach  $150 \text{ N/mm}^2$ . Solid bricks were normally used and were often fired locally. For stone material, the compressive strength of locally sourced material may range from less than  $10 \text{ N/mm}^2$  to over  $300 \text{ N/mm}^2$ . Stone properties are sometimes anisotropic.

For the mortar, this used formed using lime or Roman or Portland cement. In the case of lime mortar, composed of lime and sand, the compressive strength is typically  $0.5 \sim 1.0 \text{ N/mm}^2$ . In the case of Portland cement mortar, usually composed of cement, lime and sand, compressive strengths of greater than  $10 \text{ N/mm}^2$  are possible.

The composite masonry material is strong in compression but normally weak in tension.

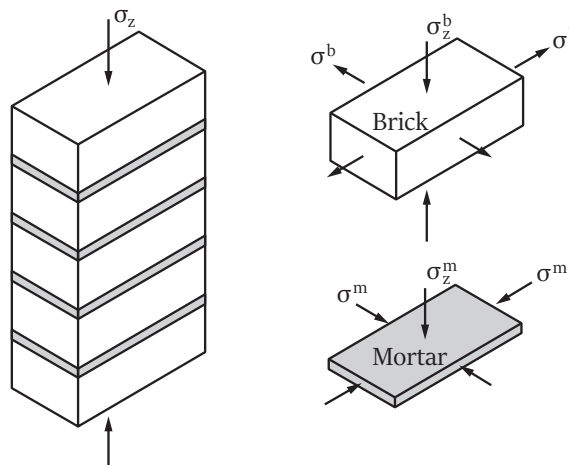


FIGURE 2.1: Masonry under uniaxial compression (Melbourne et al. 2006)

### Backfill material

The backfill material in masonry arch bridges may be cohesionless, cohesive or cohesive-frictional. Cohesionless soil is granular material (e.g. sand and gravel). Its shear strength is dependent on the inter-particle friction. Sometimes water is present; in this case, due to pore water pressures reducing the normal stresses, the shear strength will reduce. Cohesive materials (e.g. clay) are fine-grained, with the cohesive shear strength dependent on moisture content. Locally sourced cohesive-frictional materials are commonly used in retaining walls and masonry arch bridges. In this case material properties are dependent on the inter-particle friction and moisture content.

The top layer of backfill is often well compacted due to the repeated action of vehicle loading. In general, the presence of water has a significant influence on the material properties of the backfill. The strength of fully saturated backfill will be much lower than the strength of the same soil material in dry conditions, reducing bridge load-carrying capacity (Hulet et al. 2006).

### 2.1.2 Bridge Makeup

The main components of a masonry arch bridge are the arch barrel, abutments, and spandrel zone. The spandrel zone above the arch barrel is commonly filled with soil backfill.

### Arch barrel

The arch barrel is constructed using brick units or stone voussoirs. A stone arch barrel typically consists of a single ring. When using brick units, various bonding patterns may be employed, as shown in Figure 2.2.

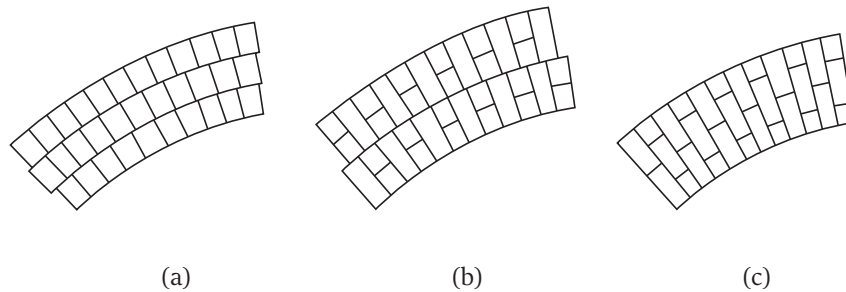


FIGURE 2.2: Typical bonding patterns: (a) Multi-ring (stretcher); (b) Intermediate (some header-bonded rings); (c) Bonded (header) (after Melbourne and Gilbert 1995)

### Abutments

Abutments may often be constructed from solid masonry as shown in Figure 2.3 (e.g. from brick or stone). Compared with a stone masonry skewback, a brick skewback may fail along a number of possible shear planes.

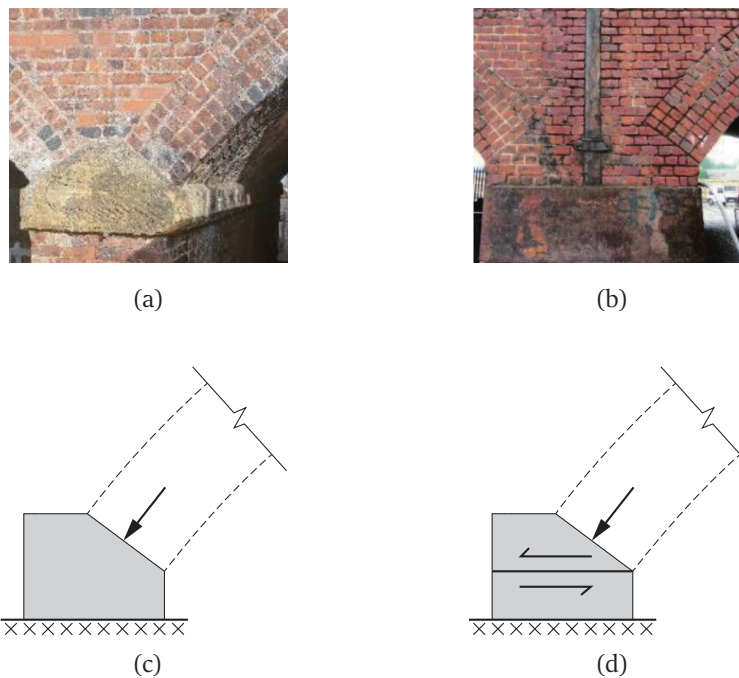


FIGURE 2.3: Diagram of abutment: (a) photograph of stone abutment; (b) photograph of brick abutment; (c) diagram of stone skewback; (d) diagram of brick skewback

## Spandrel zone

Soil backfill is commonly used to fill the spandrel zone above the arch barrel. Particularly in the case of larger structures, this is sometimes supplemented by concrete backing and/or internal spandrel walls, helping to form a level traffic surface as shown in Figure 2.4. Both soil backfill and internal spandrel walls have a strong influence on bridge load-carrying capacity (Gilbert et al. 2019, Amodio et al. 2019). In this thesis, the spandrel zone is considered to solely comprise of soil backfill.

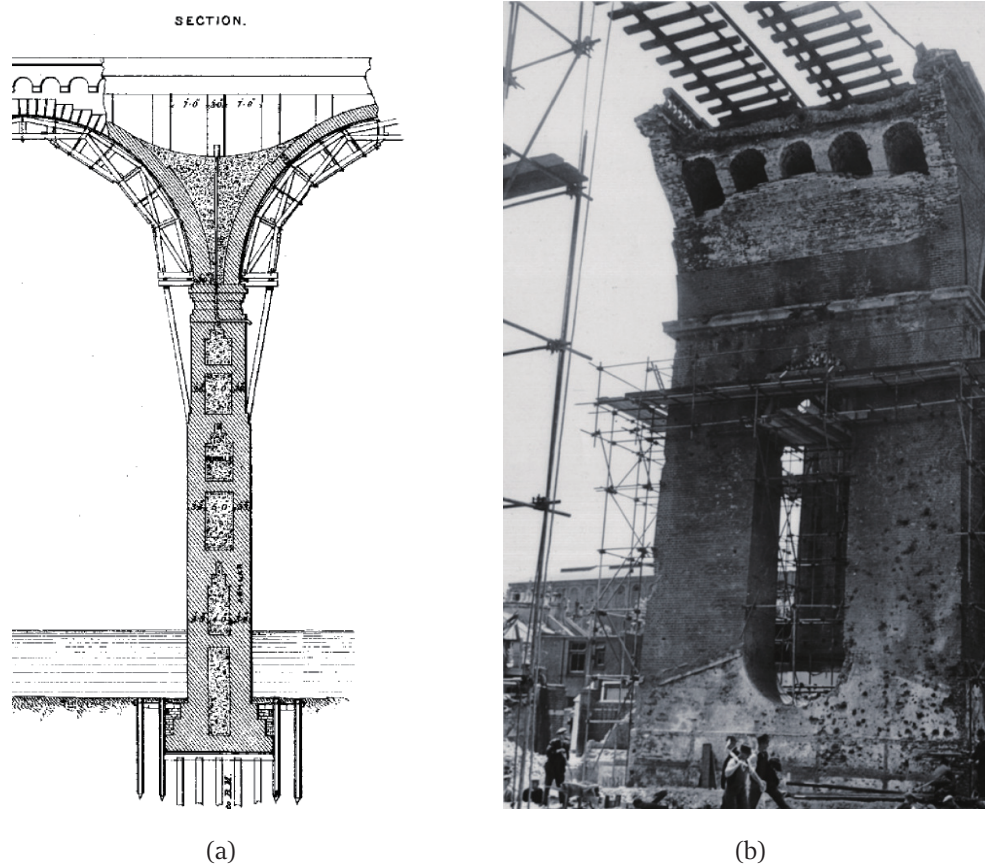


FIGURE 2.4: Spandrel zone in bridges: (a) backing of Royal Border Bridge (Bruce 1851); (b) internal spandrel walls of London Road Brighton viaduct (BrightonWorks 2020)

### 2.1.3 Bridge Behaviour

In order to represent the typical behaviour of masonry arch bridges, it is important to properly understand how arch resistance mechanisms are mobilised under loading and how failure takes place. For typical single-span masonry arch bridges, the main resistance mechanisms are as follows:

- **Geometry:** an arch geometry should be the anti-funicular shape of a dominant set of loads. Figure 2.5 shows the typical shapes of circular, pointed, elliptical and parabolic arches. The self-weight and anti-funicular arch geometry

provides 'pre-stress' and further resists arch sway under loads as shown in Figure 2.6. The geometrical way in which arches resist loads means that the load-carrying capacity is dependent on the shape of the whole arch, rather than only the arch span and rise.

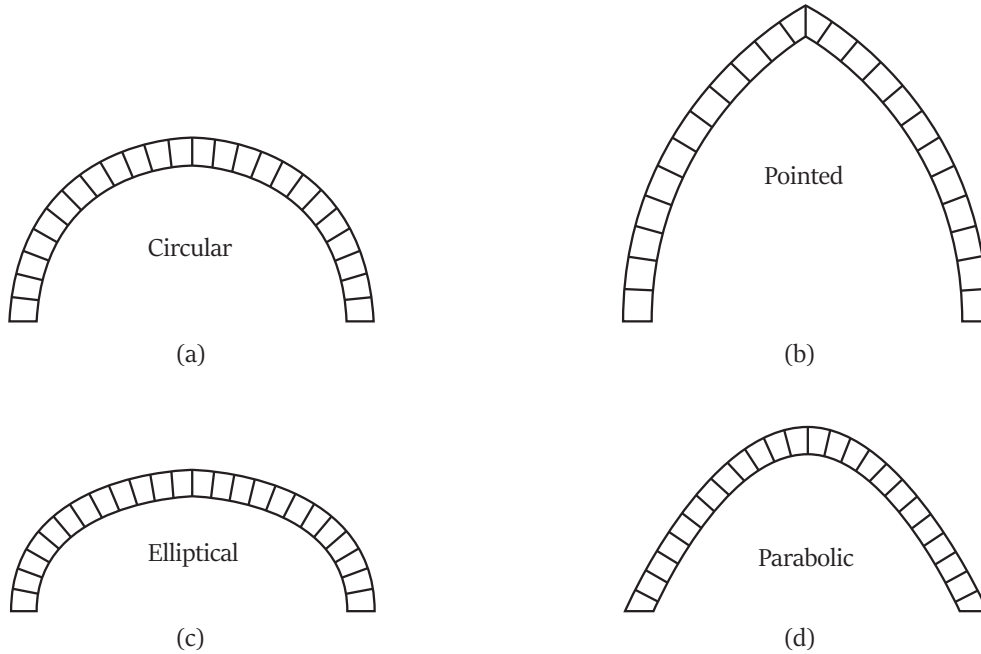


FIGURE 2.5: Arch geometries: (a) circular; (b) pointed; (c) elliptical; (d) parabolic

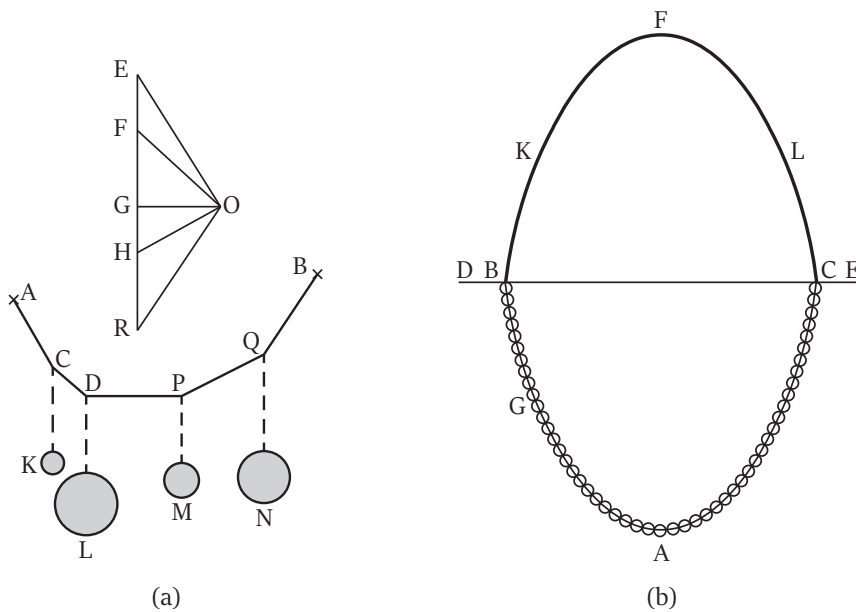


FIGURE 2.6: Robert Hooke's hanging chain: (a) one of Stevin's drawings of force equilibrium of hanging weights on a string (Stevin 1773); (b) Poleni's drawing of Hooke's analogy between an arch and a hanging chain (Poleni et al. 1748)

- Soil-fill: as a structural material, soil-fill has a significant influence on the load-carrying capacity of a bridge. Figure 2.7 shows that as the arch moves against the soil-fill under external actions, then the strength of the soil-fill is mobilised. This effect can be seen as a series of lateral earth pressures applied on the arch extrados, in addition to those induced by the weight of the soil-fill.
- Dispersal of live load: load from the road or rail surface is distributed by the soil-fill on a large area of the arch extrados. It is therefore a factor contributing to load-carrying capacity. Figure 2.7 shows the spread of the load through the soil-fill, but the extent of this in practice is unknown.
- Failure by formation of four hinged mechanism: if a load is applied at or near the quarter span of an arch, four cracks or hinges will generally gradually form as the load is increased. Figure 2.7 shows that hinges often form at both abutments, under the axle load and approximately half way between the axle load and the far abutment.
- Failure by formation of three hinges and abutment sliding mechanism: if a load is applied at the quarter span of an arch the far abutment may slide, with three hinges gradually forming in the arch as the load is increased.
- Snap-through: in the case of a flat arch, or an arch with flat regions, only three hinges may form at failure, with elastic or inelastic shortening of sections of the arch barrel lying between the outer hinges enabling a so-called snap through failure.

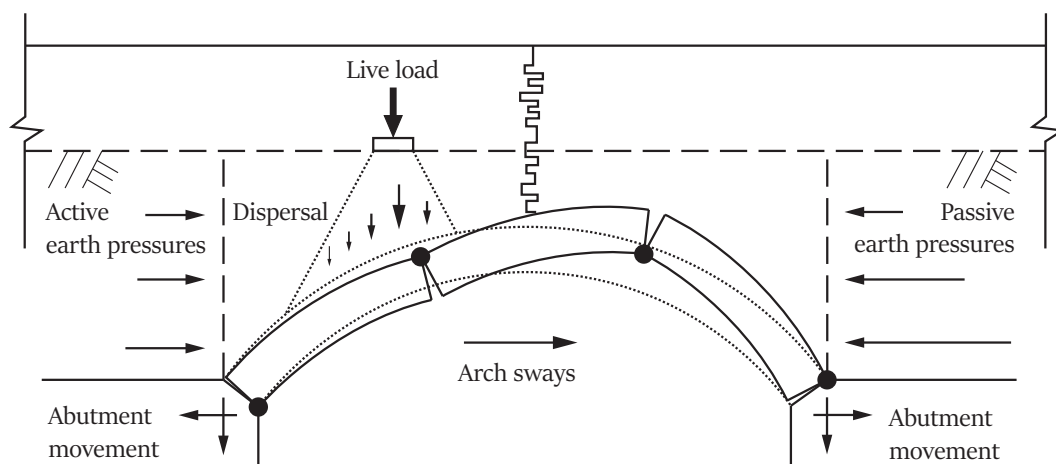


FIGURE 2.7: Four hinged failure mechanism of a masonry arch bridge (after Page 1993)

## 2.2 Theoretical Basis

Limit analysis has been used for many years to rapidly estimate the load-carrying of masonry arch bridges. In this section, the theoretical basis of limit analysis will be considered below.

### 2.2.1 Perfectly Plastic Assumption

A perfectly plastic material is a hypothetical material that undergoes no work hardening or softening after yield. Thus the stress-strain diagram of the perfectly plastic material exhibits a horizontal line at constant stress when it reaches its yield point. In a perfectly plastic material the Young's modulus below the yield point is ignored, so that it takes on any value. A rigid-perfectly plastic material is one step further removed from reality. It is a material that undergoes no deformation until it yields, and is then perfectly plastic. Because of  $E = \sigma/\varepsilon$  and  $\varepsilon = 0$ , the Young's modulus of a rigid-perfectly plastic material is infinite.

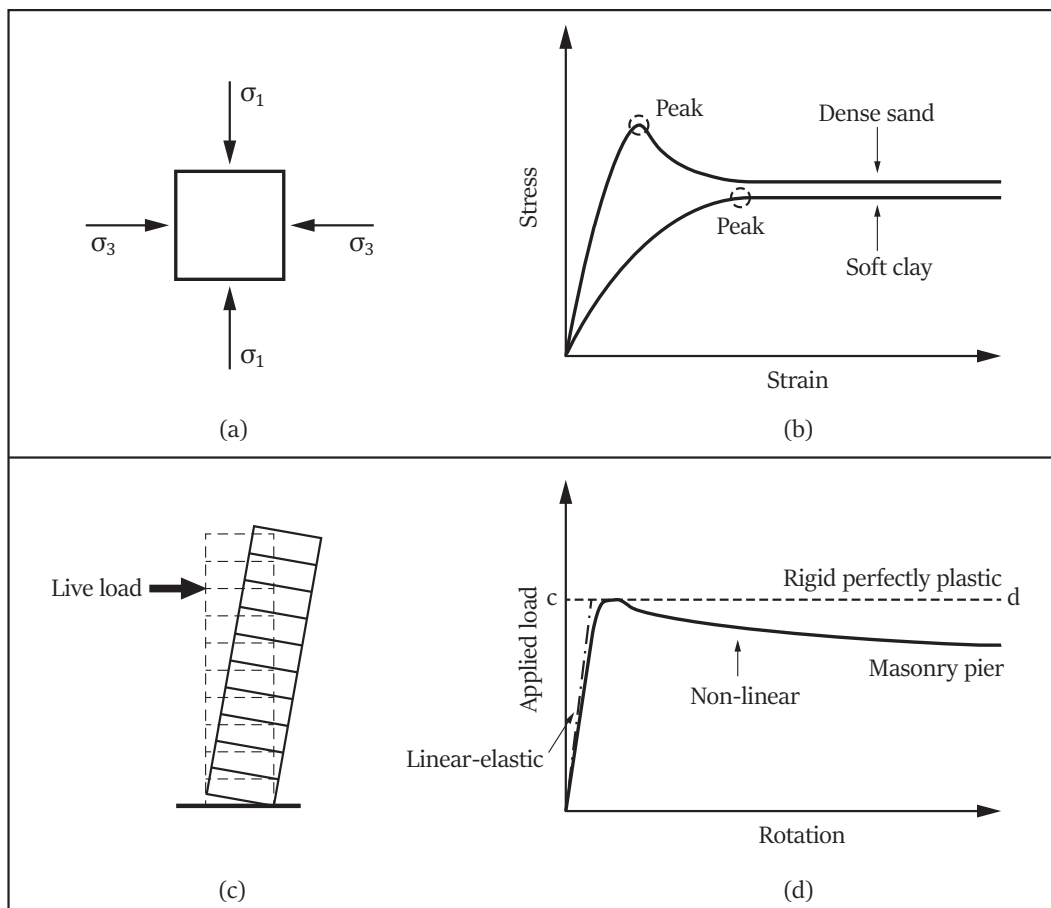


FIGURE 2.8: Perfectly plastic assumption: (a) a soil stress diagram; (b) stress-strain relationship for soils; (c) a masonry pier diagram; (d) idealised response curves of laterally loaded masonry pier

Figure 2.8 shows a typical stress-strain diagram for soils and an ‘applied load vs. rotation’ diagram for a masonry pier respectively. For the stress-strain behaviour of most dense sand, it is characterised by an initial linear portion and a peak stress followed by softening to a residual stress. For the typical soft clay, it is characterised by an initial linear portion and a peak stress. Considering the ‘applied load vs. rotation’ behaviour of a masonry pier, this is characterised by an initial linear portion, failure, followed by a falling branch. In limit analysis, it is necessary to ignore the falling branch in these diagrams. For a normal perfectly plastic material, it is usual to idealise behaviour as bi-linear. For a rigid-perfectly plastic material, a single horizontal line can be used to describe the behaviour.

## 2.2.2 Equilibrium Condition Based on Stresses

If the solution of a problem is rigorous, it is necessary to require the computed stresses strictly satisfy the equilibrium condition. The stress fields in a solid body are illustrated by Figure 2.9. Figure 2.9(a) shows a unit element of a solid body which is subjected by the self-weight of  $\gamma dx dz$ . For an infinitesimal element acted upon by given stresses, the equilibrium equations can be expressed as

$$\begin{cases} \frac{\partial \sigma_z}{\partial z} + \frac{\partial \tau_{zx}}{\partial x} = \gamma \\ \frac{\partial \sigma_x}{\partial x} + \frac{\partial \tau_{xz}}{\partial z} = 0 \end{cases} \quad (2.1)$$

These equations are satisfied if

$$\begin{cases} \sigma_x = \frac{\partial^2 F}{\partial z^2} \\ \sigma_z = \frac{\partial^2 F}{\partial x^2} \\ \tau_{xz} = -\frac{\partial^2 F}{\partial x \partial z} + \gamma x + C \end{cases} \quad (2.2)$$

where  $F$  is the arbitrary function of  $x$  and  $z$ ;  $C$  is the constant of integration. Equation 2.2 indicates that there are an infinite number of stresses that satisfy equation 2.1. However, only one of them corresponds to reality. In order to solve the problem, equations 2.1 must be supplemented by boundary condition information.

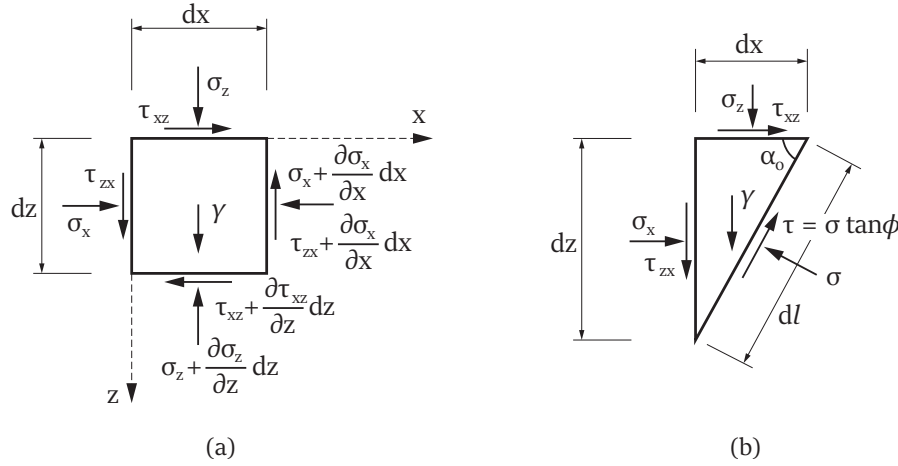


FIGURE 2.9: Diagrams illustrating the equilibrium condition (Terzaghi 1943)

### 2.2.3 Mohr-Coulomb Yield Condition

The stress-strain relationship of soil (or masonry materials when subject to shear) can be characterised by a simple shear test or a triaxial compression test. It is important to know the yield strength of the soil and masonry materials for a complex stress state. It is necessary to design a possible form of the condition, which satisfies in the yield state. This condition characterise the change of the material from an elastic state to a plastic flow state. When the plastic flow occurs at any point in a given body, the equation of the yield condition can be expressed as

$$\tau = c + \sigma \tan \phi \quad (2.3)$$

where  $\tau$  is the shear stress;  $c$  is the cohesion stress;  $\sigma$  is the compressive stress;  $\phi$  is the angle of friction. The constants  $c$  and  $\phi$  can be determined simply as parameters which characterise the shear strength of the soil and masonry materials. This equation was first suggested by Coulomb (1973).

Figure 2.10 shows a diagram of the Coulomb yield condition. If the Mohr circle at a stress state touches the boundary lines, then equation 2.3 can be expressed as

$$\sqrt{\left(\frac{\sigma_x - \sigma_z}{2}\right)^2 + \tau_{xz}^2} - \frac{\sigma_x + \sigma_z}{2} \sin \phi = c \cos \phi \quad (2.4)$$

In a perfectly plastic material, the stresses are computed by equations 2.2 with a set of supplementary equations obtained by establishing the effective boundary conditions, and satisfy the Coulomb yield condition for perfectly plastic equilibrium in every point of the given body.

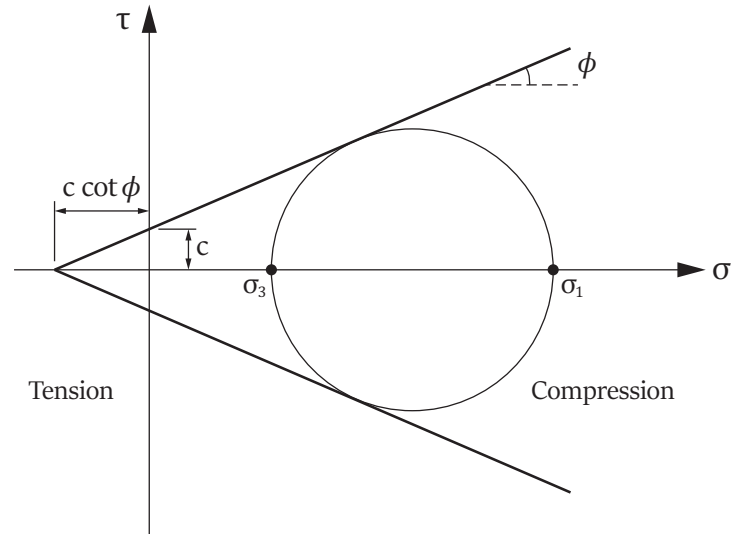


FIGURE 2.10: Mohr's representation of a stress and the Coulomb yield condition (after Terzaghi 1943)

#### 2.2.4 Mechanism Condition Based on Thrust Line

The line of thrust represents the location and trajectory of the line of compressive force in an arch. In a masonry arch, since the effective moment of resistance varies continuously, the bending moment diagram is difficult to interpret. However, because the 'no-tension' yield condition dictates that the thrust line must lie entirely within the thickness of the masonry, the line of thrust can be used to provide an indication of the safety of a masonry arch under a given set of loads. The thrust line can be plotted by computing the eccentricity of the compressive force at each 'cross-section' (where eccentricity = moment / compressive force). The resulting thrust line at collapse for a masonry pier and arch are shown in Figure 2.11.

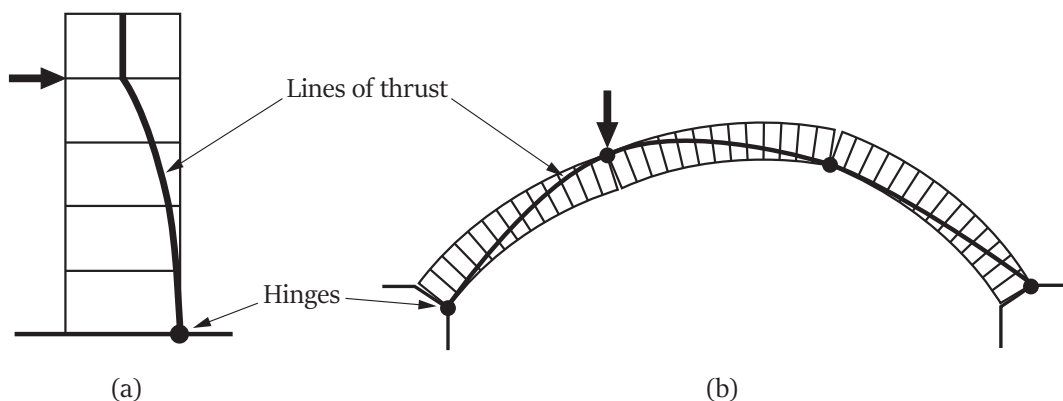


FIGURE 2.11: Failure mechanisms: (a) pier, showing thrust line; (b) masonry arch, showing thrust line (Gilbert 2007)

In the case of the masonry pier as shown in Figure 2.11(a), because the structure is statically determinate, there is only one position of the thrust line up to the point

of failure. In contrast, in the case of the masonry arch, shown in Figure 2.11(b), since the structure is statically indeterminate, there are many possible positions of the thrust line prior to failure, but only one position at failure.

### 2.2.5 Limit Analysis Method

#### Upper-bound theorem

As stated in the upper-bound theorem, if a failure mechanism can be found, and the rate of work done by the external forces exceeds the internal rate of energy dissipation, then the imposed loads cannot be carried by a given body (Chen 1975). Thus equating external to internal work done for any such mechanism gives an unsafe, or 'upper bound' solution. A velocity field satisfying all these conditions is called a kinematically admissible velocity field. The velocity fields must satisfy

- velocity boundary conditions;
- velocity compatibility conditions.

From these rules, an upper bound technique considers only failure modes and energy dissipation.

#### Lower-bound theorem

As stated in the lower-bound theorem, if a complete stress field can be found, everywhere satisfying the equilibrium and stress boundary conditions, then the imposed loads can be carried without yield in a given body. Thus any such stress field gives a safe, or 'lower bound', solution. The stress field satisfying all these conditions is called statically admissible stress field. The stress fields must satisfy

- the equilibrium equations;
- the stress boundary conditions;
- nowhere violate the yield criteria.

From these rules, a lower-bound technique considers only equilibrium and yield conditions.

### 2.2.6 Limit Equilibrium Method

Limit equilibrium methods have traditionally been used to obtain approximate solutions for rock and soil mechanics stability problems. The method can be described as an approximate approach to finding the most dangerous position of the failure surface. With limit equilibrium methods, an overall equilibrium equation involving stress resultants can be written for a given problem. The stress distribution

along the failure surface satisfies the yield criteria and the associated flow rule in the stress—strain relationship of the material involved. However, the stress distribution in a limit equilibrium method is not defined anywhere inside or outside the assumed failure surface, so that the method cannot definitely satisfy the equilibrium, stress boundary and yield criteria conditions. Also, although a failure surface is assumed, it usually does not precisely satisfy the requirements of the upper bound theorem. Therefore, a solution obtained using a limit equilibrium method is not necessarily a lower or an upper bound, but is an approximate solution.

## 2.3 Analysis Methods

The principal analytical methods for estimating the load-carrying capacity of masonry arch bridges involve linear-elastic analysis, plastic limit analysis, and non-linear analysis. A review of these methods is provided as follows:

### 2.3.1 Linear-elastic analysis

Conventional linear-elastic analysis methods assume materials are perfectly elastic. These methods are simple and widely used in practice. However, when such analyses are applied to masonry arch bridges, the results should be treated with caution. This is because in a linear-elastic analysis, it is implicitly assumed that both compressive and tensile stresses can be resisted, whereas in reality masonry is often not capable of resisting even very small tensile stresses. However, a linear-elastic analysis can be used to check stresses against predefined stress criteria to assess vulnerability to load effects. Alternatively, modified elastic analysis methods that use an iterative procedure in which masonry is progressively thinned in regions with the presence of tensile stresses can be useful (Castigliano 1966, Choo et al. 1991, Brencich 2001, Brencich and De Francesco 2004).

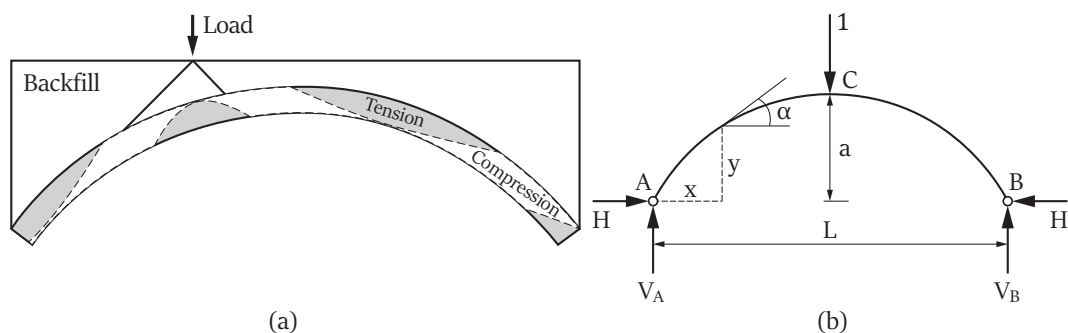


FIGURE 2.12: Linear-elastic analysis of a single span: (a) elastic no tensile resistant-plastic analysis (after Brencich and De Francesco 2004); (b) Pippard's two-pinned parabolic arch (Wang and Melbourne 2010)

As a linear-elastic analysis, the semi-empirical 'MEXE' (e.g. derived by Military Engineering Experimental Establishment) method, which employed an elastic rib

spanning between two pinned abutments, is simple and has proven to be popular over the years (Pippard & Chitty 1951). However, in recent decade research indicates that a modified version of the method can provide non-conservative bridge assessments (Wang and Melbourne 2010).

### 2.3.2 Plastic limit analysis

Plastic limit analysis methods assume materials are rigid-plastic. These methods usually model masonry as a no-tension material, overcoming a limitation of linear-elastic analysis methods. Consequently, they have been widely used to estimate the load-carrying capacity of masonry arch bridges in recent decades, with workers such as Kooharian (1952), most notably, Heyman (1982) using what we can refer to as the ‘line of thrust method’ to assess arch stability. The classical assumptions proposed by Heyman are as follows

- arch has no tensile strength,
- arch has infinite compressive strength, and
- sliding cannot occur.

If a line of thrust can be found that lies within the middle third of the masonry, as shown in Figure 2.13(b), then the solution does not violate the no-tension yield constraint if elastic methods are used. It also satisfies the lower bound theorem of plastic limit analysis. Funicular methods utilizing Heyman’s statement of the lower bound theorem have been developed to analyse masonry structures. In such methods, an equilibrium path can be found to verify the safety of the structure. This method has been developed by many researchers over the years (O’Dwyer 1999, Ochsendorf 2006). For example, Block et al. (2006) developed an interactive analysis tool for masonry structures in which the user can move the supports or alter the geometry of the structure, with the thrust line within the structure then automatically redrawn.

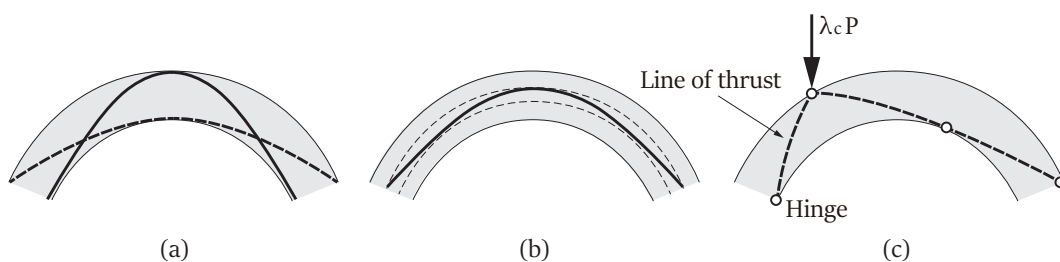


FIGURE 2.13: Possible thrust lines: (a) min/max thrust, (b) thrust line with a geometric safety factor, and (c) thrust at collapse (Block 2009)

Although the arch barrel can be modelled using continuum idealisations, the fact that the joints in the masonry form predefined planes of weakness makes discrete analysis attractive. Livesley (1978) developed a discrete limit analysis model which could be used to assess the stability of assemblages of masonry blocks. Additionally, several authors developed simpler ‘automated hand calculation’ limit analysis procedures which involve using heuristic methods to identify the critical failure mechanism; these initially found favour for masonry arch bridge analysis (Crisfield and Packham 1987, Harvey 1988).

### Rigid-block analysis

Following validation against experimental results (e.g. Melbourne and Gilbert 1995, Melbourne et al. 1997), the more general ‘rigid-block’ analysis procedures found favour (Livesley 1992, Gilbert and Melbourne 1994). In this case the solution procedure uses linear programming (LP) techniques and is implemented in the LimitState:RING software (Gilbert 2001, LimitState 2019b), as shown in Figure 2.15(a). In this model, the inter-block contact behaviour is controlled by constraint equations and a no tension criterion is adopted. The ‘no sliding’ restriction is also removed, which increases the generality of the method. An equilibrium formulation is presented below:

Assuming there are  $b$  blocks and  $c$  contact surfaces, the problem is stated as follows (LimitState 2019b)

$$\max \lambda \quad (2.5)$$

subject to equilibrium constraints:

$$\mathbf{B} \cdot \mathbf{q} - \lambda \cdot \mathbf{f}_L = \mathbf{f}_D \quad (2.6)$$

and no-tension yield constraints (e.g. for each contact,  $i = 1, \dots, c$ ):

$$\begin{cases} M_i \leq 0.5 t_i N_i \\ M_i \geq -0.5 t_i N_i \end{cases} \quad (2.7)$$

and sliding yield constraints (e.g. for each contact,  $i = 1, \dots, c$ ):

$$\begin{cases} S_i \leq \mu N_i \\ S_i \geq -\mu N_i \end{cases} \quad (2.8)$$

where  $\lambda$  is the load factor;  $\mathbf{B}$  is a suitable ( $3b \times 3c$ ) equilibrium matrix;  $\mathbf{q}$  contains vectors of contact forces and  $\mathbf{q}^T = \{N_1, S_1, M_1, N_2, S_2, M_2, \dots, N_c, S_c, M_c\}$ ;  $\mathbf{f}_D$  and  $\mathbf{f}_L$  are respectively vectors of dead and live loads (e.g. block loads) applied at the centroid of blocks. Figure 2.14 shows contact and block forces, arch thickness, frictional property. In this formulation, the LP variables are the contact forces  $\mathbf{q}$  containing  $N_i, S_i, M_i$  (e.g.  $N_i \geq 0$ ,  $S_i$  and  $M_i$  are unrestricted variables). If  $\mathbf{f}_L$  is assumed as unit, maximizing the load factor  $\lambda$  can obtain the collapsed load factor. Details of the formulation of the DLO method are provided in Appendix A.

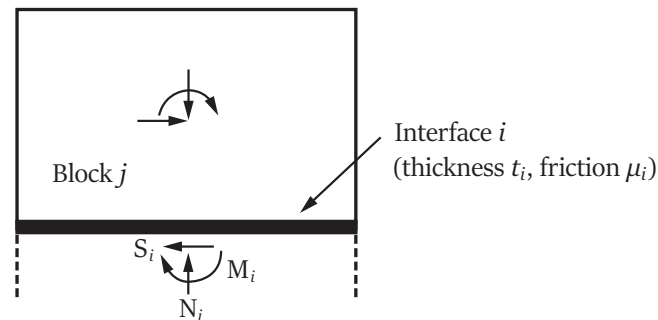


FIGURE 2.14: Block  $j$  and contact forces for interface  $i$  (Gilbert 2007)

Considering soil backfill material, the program models the anticipated effects of the soil in the soil-arch interaction. The backfill is assumed: (i) to disperse applied loading, (ii) to provide self-weight, and (iii) to provide passive restraint, as shown in Figure 2.15(a). However, fixed earth pressures need to be defined before the analysis is run; the bridge load-carrying capacity is highly dependent on the magnitudes of these pressures.

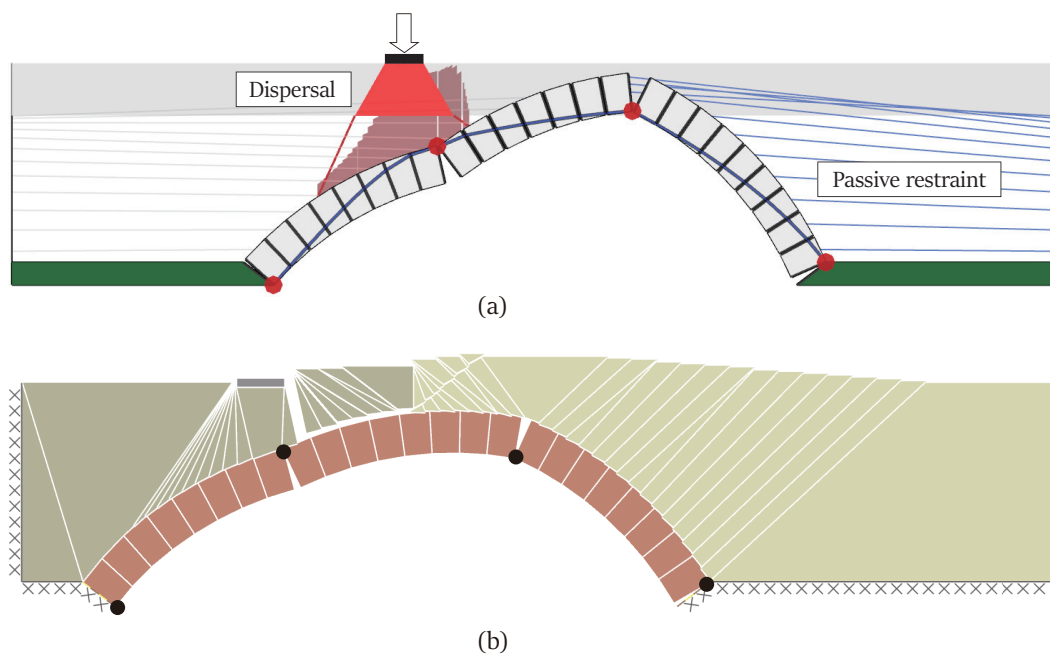


FIGURE 2.15: Analysis of masonry arch bridge using: (a) LimitState:RING, and (b) LimitState:GEO

### Discontinuity layout optimization

In order to provide a better representation of the soil-arch interaction, the soil backfill needs to be modelled explicitly. Due to the importance of the backfill, and to enable other geotechnical problems to be solved, a limit analysis technique called discontinuity layout optimization has been proposed (Smith and Gilbert 2007, Gilbert et al. 2010). The solutions obtained have been validated against experimental results (Gilbert et al. 2010, Callaway et al. 2012).

The DLO limit analysis technique procedure also uses linear programming (LP) to obtain solutions and is implemented in the LimitState:GEO software (Smith and Gilbert 2007, LimitState 2019a), as shown in Figure 2.15(b). In this model, the yield constraints employed are based on the Mohr-Coulomb criteria, which is used for both masonry and soil-fill elements.

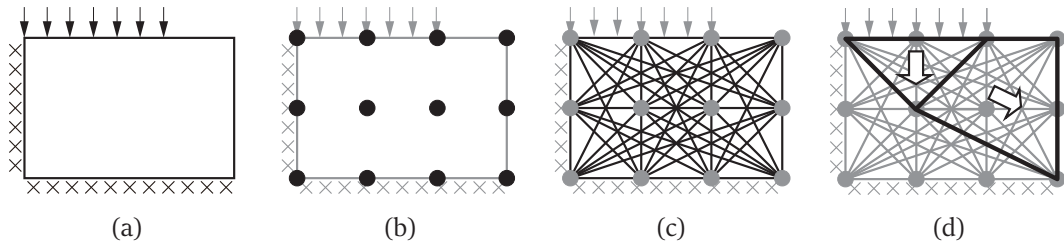


FIGURE 2.16: Stages in DLO procedure: (a) initial solid body; (b) discretize with nodes; (c) interconnect nodes with potential discontinuities; (d) identify critical subset of discontinuities using optimization (Smith and Gilbert 2007)

Stages in the DLO procedure are outlined diagrammatically in Figure 2.16. In DLO a limit analysis problem is formulated in terms of the potential discontinuities that interconnect the discrete nodes in the solid body. These discontinuities are allowed to cross over one another. The formulation of the primal DLO problem is presented below:

Assuming there are  $n$  nodes and  $m$  discontinuities in a single load case, the problem is stated as follows (LimitState 2019a)

$$\min \lambda \mathbf{f}_L^T \mathbf{d} = -\mathbf{f}_D^T \mathbf{d} + \mathbf{g}^T \mathbf{p} \quad (2.9)$$

subject to:

$$\mathbf{B} \mathbf{d} = \mathbf{0} \quad (2.10)$$

$$\mathbf{N} \mathbf{p} - \mathbf{d} = \mathbf{0} \quad (2.11)$$

$$\mathbf{f}_L^T \mathbf{d} = 1 \quad (2.12)$$

$$\mathbf{p} \geq \mathbf{0} \quad (2.13)$$

where  $\lambda$  is the load factor;  $\mathbf{f}_D$  and  $\mathbf{f}_L$  are respectively vectors of dead and live loads at discontinuities;  $\mathbf{d}$  contains displacements along the discontinuities;  $\mathbf{p}$  is a vector of plastic multipliers and  $\mathbf{g}$  contains the corresponding dissipation coefficients.  $\mathbf{B}$  is an equilibrium matrix containing direction cosines, and  $\mathbf{N}$  is a flow matrix. Details of the formulation of the DLO method are provided in Appendix B.

### 2.3.3 Other analysis methods

A wide range of other analysis approaches can be applied to backfilled masonry arch bridges, including non-linear finite element analysis (e.g. Crisfield 1993), finite element limit analysis (Cavicchi and Gambarotta 2005, Gilbert 2007), discrete element based methods (e.g. Cundall and Strack 1979), and physics engine based methods (Pytlos 2015). Results from a finite element limit analysis model and a physics engine based model are shown in Figure 2.17. Models capable of modelling material non-linearity and geometrical non-linearity can be used to identify specific modes of behaviour (e.g. ‘snap through’, as described in section 2.1.3).

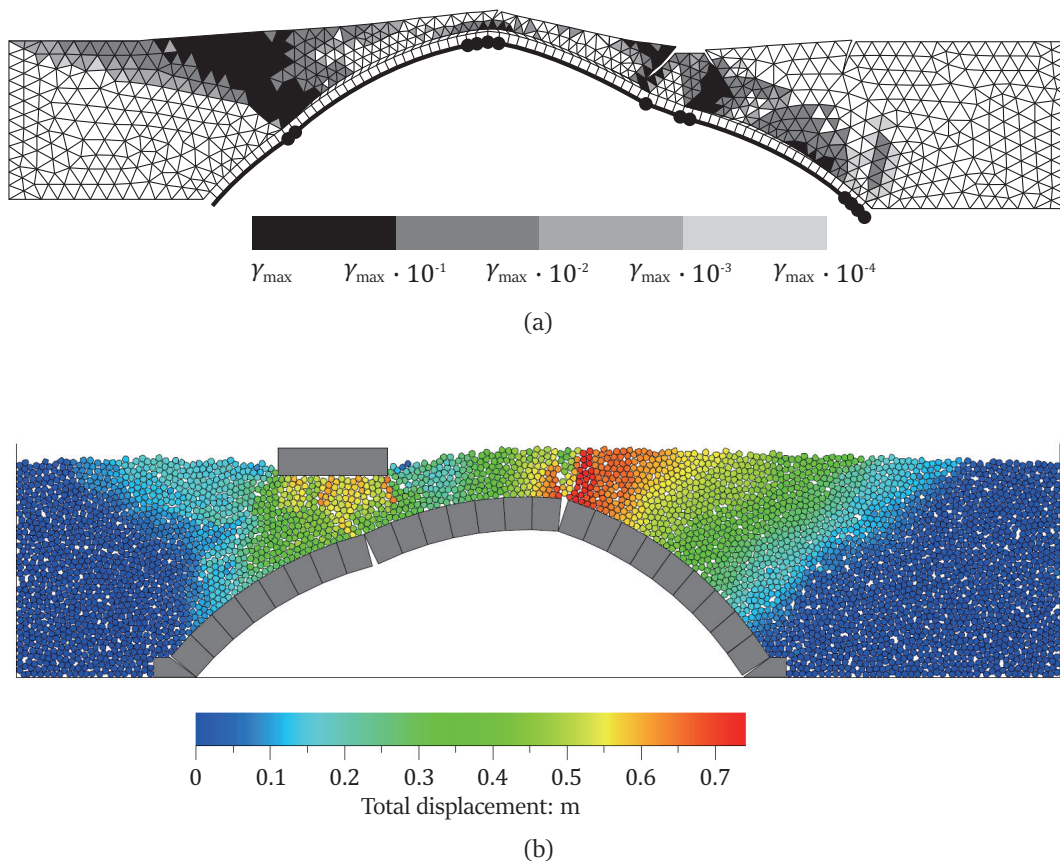


FIGURE 2.17: The deformed shape of masonry arch bridges: (a) finite element limit analysis result (Cavicchi and Gambarotta 2005); (b) physics engine based method result (Pytlos 2015)

However, non-linear analysis models can be cumbersome to use in practice. This is because the initial stress state in an existing bridge is effectively unknowable, meaning that a range of starting points for the analysis should be used, and also many of the material properties required to run the analysis will be difficult to establish. Thus considering the data preparation, run time and expertise required for non-linear analysis tools, it can be concluded that these are not yet suitable for routine use.

### 2.3.4 Choosing a Suitable Analysis Method

The choice of analysis method for masonry arch bridges is dependent on the goal of the assessment, including whether there is a need to establish the service load behaviour, to estimate the ultimate load carrying capacity, or to predict displacements under traffic loads. Considering the methods described in the previous sections, these are categorised in Table 2.1, ranging from Level 1 (simple) to Level 3 (advanced). The choice of method will in practice partly depend on the importance and complexity of the masonry arch bridge to be assessed.

TABLE 2.1: Applicability of analysis methods

Objective	Level 1 Linear-elastic analysis (e.g. MEXE)	Level 2 Plastic limit analysis (e.g. ArchieM, LimitState:RING, LimitState:GEO)	Level 3 Non-linear analysis (e.g. ABAQUS, LUSAS)
	Run time: 	Run time: 	Run time: 
Establishing service load behaviour			
Estimating ultimate load carrying capacity			
Modelling displacements under traffic loads			

## 2.4 Laboratory and Field Tests on Masonry Arch Bridges

In this thesis, plastic limit analysis of masonry arch bridges will be the main focus. In order to illustrate application of the methods developed, three bridges will be used as examples. These include a Bolton laboratory arch bridge (Melbourne and Gilbert 1995) and a Salford laboratory arch bridge (Smith et al. 2006, Gilbert et al. 2010). The Bridgemill bridge that was tested in the field is also considered (Hendry et al. 1985). In this section, the data required to model these bridges are described.

### 2.4.1 Bolton arch bridge

The Bolton arch bridge considered herein was tested at Bolton Institute (now University). The 5 m span bridge comprised four arch rings. In order to simplify the arch barrel, the four arch rings were assumed in this thesis to act as one ring made of 87 blocks (Melbourne and Gilbert 1995). Figure 2.18 shows the simplified bridge geometry, and the main material properties are listed in Table 2.2. The effective bridge width is assumed as unit.

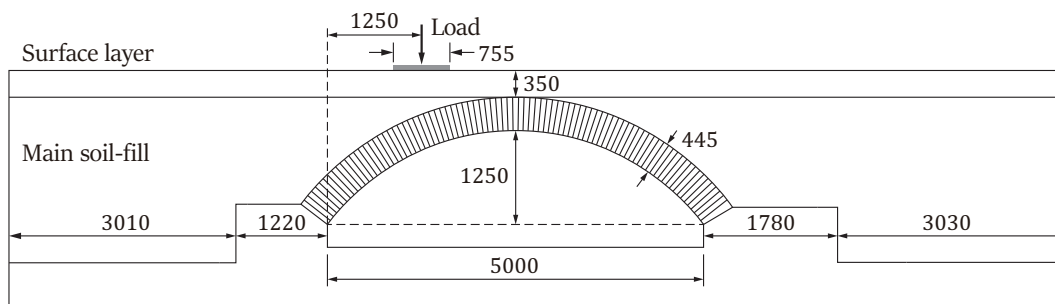


FIGURE 2.18: Geometry of Bolton arch bridge (all dimensions in mm)

TABLE 2.2: Material properties of Bolton arch bridge (Melbourne and Gilbert 1995)

Masonry properties	Values
Crushing strength ( $\text{N}/\text{mm}^2$ )	18.1
Coefficient of friction	0.64
Unit weight ( $\text{kN}/\text{m}^3$ )	22.7
Main soil-fill properties	Values
Cohesion, $c$ ( $\text{kN}/\text{m}^2$ )	0
Internal angle of friction, $\phi$ (degrees)	60
Soil-arch interface strength multiplier	0.33
Unit weight ( $\text{kN}/\text{m}^3$ )	22.2

### 2.4.2 Salford arch bridge

The Salford arch bridge considered herein was tested at the University of Salford (Smith et al. 2006). The bridge had a span of 3 m and comprised 48 units. The bridge was housed in a large test chamber which had very stiff low friction walls, providing effectively plane-strain conditions. Figure 2.19 shows the geometry of the bridge tested, and the main material properties involved are provided in Table 2.3. The position of the arch within the test chamber varied, dependent on the soil-fill material present so that the full failure mechanism could be captured. The effective bridge width is assumed as unit.

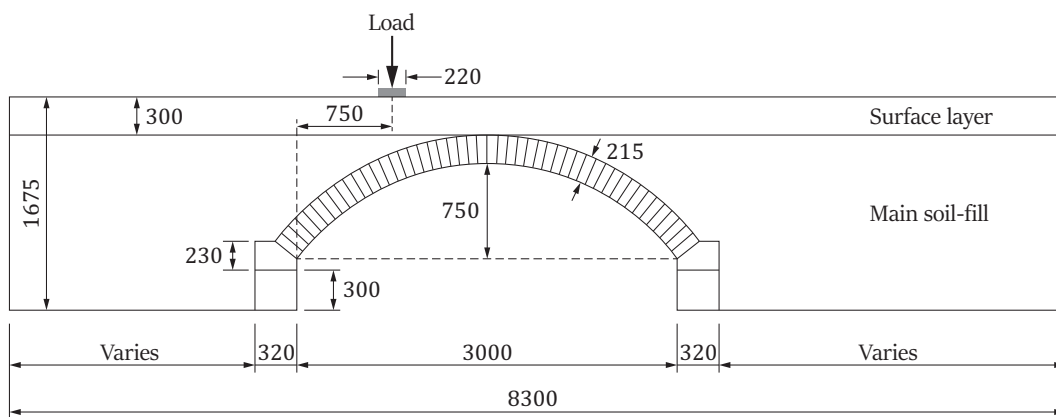


FIGURE 2.19: Geometry of Salford arch bridge (all dimensions in mm)

TABLE 2.3: Material properties of Salford arch (Gilbert et al. 2010)

Masonry properties	Values
Crushing strength ( $\text{N}/\text{mm}^2$ )	25
Coefficient of friction	0.64
Unit weight ( $\text{kN}/\text{m}^3$ )	23.7
Main soil-fill properties	Values
Cohesion, $c$ ( $\text{kN}/\text{m}^2$ )	3.3
Internal angle of friction, $\phi$ (degrees)	54.5
Soil-arch interface strength multiplier	0.33
Unit weight ( $\text{kN}/\text{m}^3$ )	19.1

### 2.4.3 Bridgemill arch bridge

The Bridgemill arch bridge was tested at Girvan, Scotland. It was a relatively shallow arch bridge incorporating an arch barrel made up of 62 sandstone blocks (Hendry et al. 1985). The geometry of the real bridge is shown in Figure 2.20. A load was applied to a 750 mm length concrete strip crossing the whole bridge width and centered at the quarter span of the bridge, considered the weakest position for the structure. The masonry and soil-fill material parameters for the bridge are provided in Table 2.4. The effective bridge width is assumed as unit.

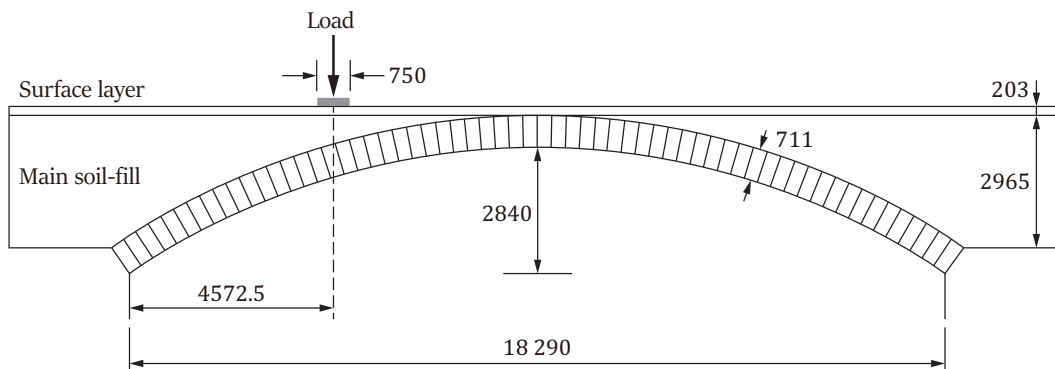


FIGURE 2.20: Geometry of Bridgemill arch (all dimensions in mm)

TABLE 2.4: Material properties of Bridgemill arch (Brencich and De Francesco 2004)

Masonry properties	Values
Crushing strength ( $\text{N}/\text{mm}^2$ )	4
Coefficient of friction	0.64
Unit weight ( $\text{kN}/\text{m}^3$ )	21
Main soil-fill properties	Values
Cohesion, $c$ ( $\text{kN}/\text{m}^2$ )	0
Internal angle of friction, $\phi$ (degrees)	60
Soil-arch interface strength multiplier	0.33
Unit weight ( $\text{kN}/\text{m}^3$ )	22

#### 2.4.4 Discontinuity Layout Optimization Modelling

In order to rapidly assess the safety of these bridges, plastic limit analysis based methods can be applied. From the description of the plastic limit analysis methods in section 2.3.2, it is clear that rigid-block analysis method and the DLO procedure are simple and easy to use compared with non-linear analysis methods. LimitState:RING and LimitState:GEO are commercial software packages that utilise the rigid-block analysis method and the DLO procedure respectively. Application of the two methods can be illustrated by considering the Salford arch bridge.

To compare rigid-block analysis method and the DLO procedure, the arch barrel of the Salford bridge can be modelled by both methods. The load is positioned at the quarter span of the structure. Numerical failure mechanisms are shown in Figure 2.21, and the load factor is 18.2 in both cases. It indicates that both the rigid-block analysis method and the DLO procedure are capable of modelling masonry arch structures.

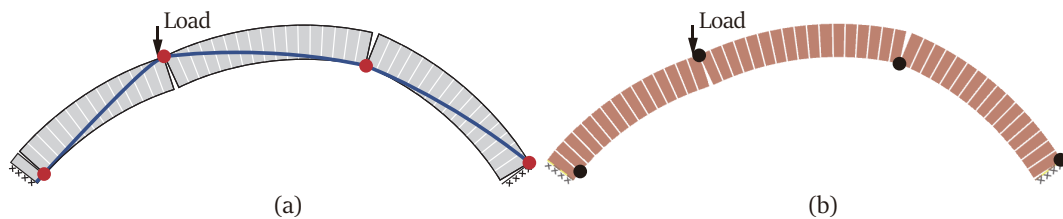


FIGURE 2.21: Four hinged failure mechanisms: (a) rigid-block analysis; (b) DLO output

However, when soil backfill is placed around the arch, differences arise. Soil-fill is modelled indirectly in LimitState:RING, where it is assumed that it disperses live load and provides self-weight and passive restraint to parts of arch barrel pushing into the backfill. In contrast, DLO can directly model both masonry and soil elements.

Consider a DLO model of the bridge with backfill, as shown in Figure 2.22. This model consists of a series of geometrical regions (potential active and passive regions),  $48 \times$  block unit, and a rigid loading beam. Appropriate material properties were then assigned to each geometrical region. All regions were then discretized using nodes.

For the masonry elements of the model, masonry units were modelled using a rigid material, and masonry joints were modelled using a Mohr-Coulomb material model and a limiting 'tension and/or compression' material model. The Mohr-Coulomb material involved zero cohesion and an angle of friction derived from ' $\phi = \tan^{-1}(0.64)$ ' (Gilbert et al. 2010). The masonry compressive strength was assigned a value of  $25 \text{ N/mm}^2$ .

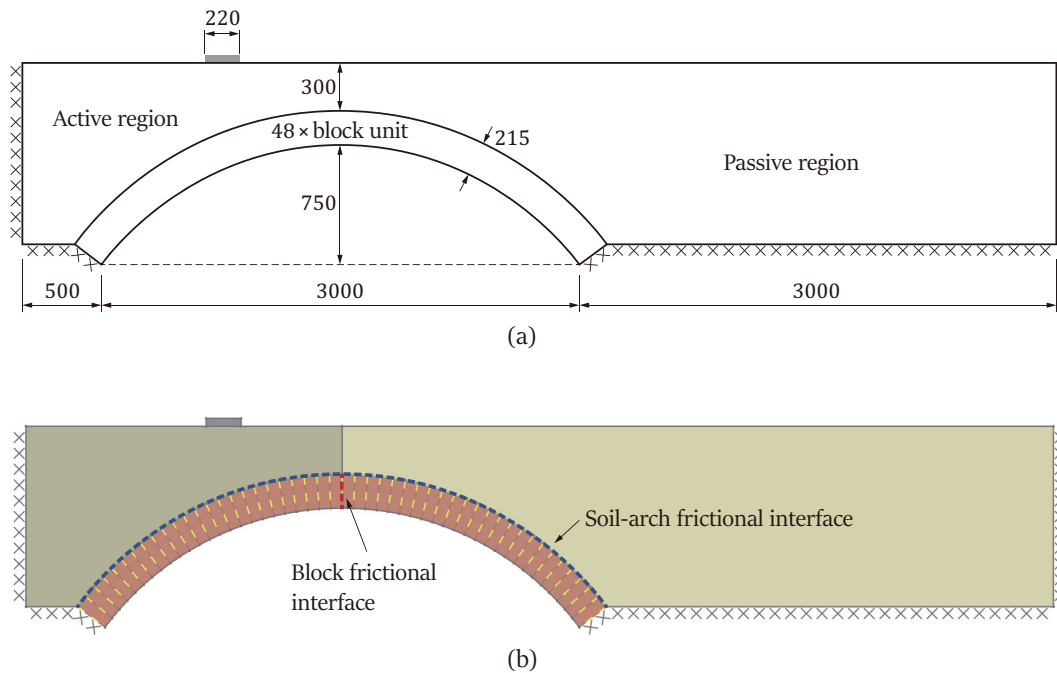


FIGURE 2.22: Geometrical model of Salford arch bridge: (a) geometry dimensions (all dimensions in mm); (b) DLO input

For the soil model, (Gilbert 2007) indicated that soil strains in the passive regions of a masonry arch bridge are very small when the collapse load is reached. Thus if peak soil strength is used in the model, bridge load-carrying capacity will be over-predicted. In order to address this issue, strain compatibility at the soil-arch interface also needs to be carefully considered. On the passive side, an approximate displacement of the arch under the load of between 1 and 5 mm will give rise to a rotation of each arch segment of approximately 0.1–0.5% (Gilbert et al. 2010). Bolton (1992) indicated that for a clay soil, approximately 0.33 of the shear strength might be mobilised at a shear strain of mobilised at a shear strain of 0.25%. Based on the above, a soil-arch interface strength multiplier of 0.33 or 0.5 was used in the model, and a mobilization factor of 0.33 or 0.5 was applied to the soil strength  $c$  and  $\tan \phi$  in passive regions.

Although the DLO result is in this case in closer agreement with the test result, in this case the DLO procedure took around 120 seconds (when using 5000 nodes) to obtain the solution. If a large number of load positions need to be considered then the DLO run time becomes an issue. The DLO result of Salford arch bridge analysis is shown in Figure 2.23.

The LimitState:RING result is in this case also in good agreement with the experimental result, but the gap will only be small when the load position is close to the quarter span of the bridge, when a characteristic 4 hinge mechanism forms. In other scenarios the gap can be expected to be far wider.

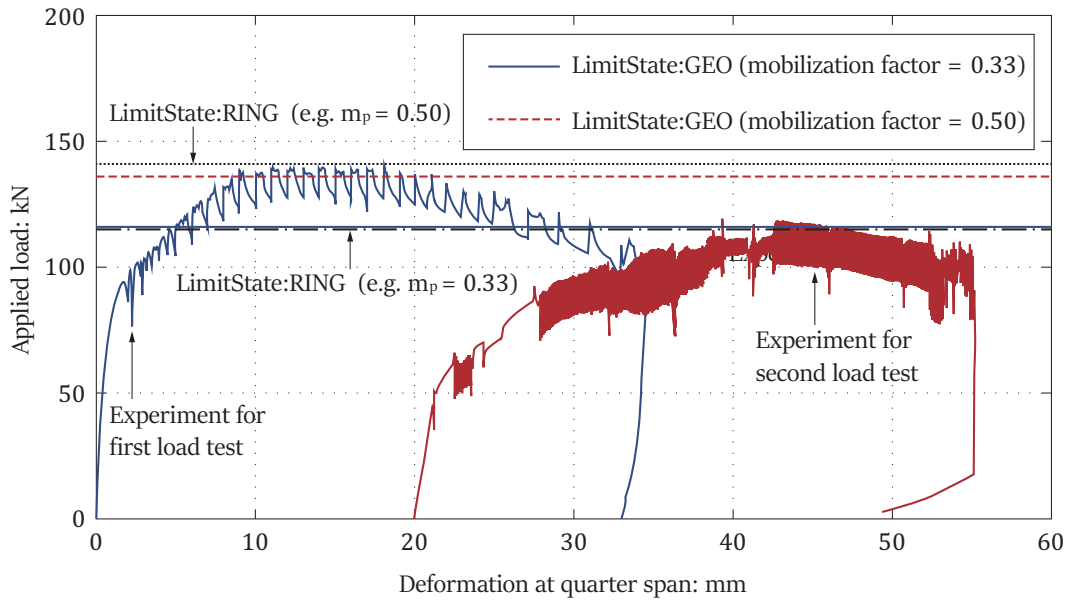


FIGURE 2.23: Applied load against deformation at the quarter-span of Salford arch bridge

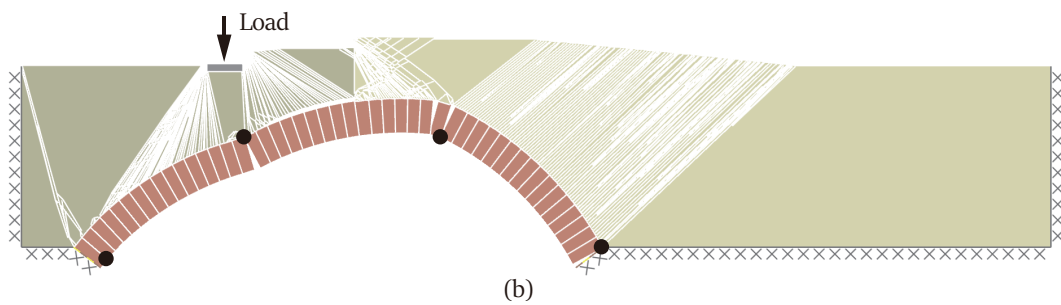
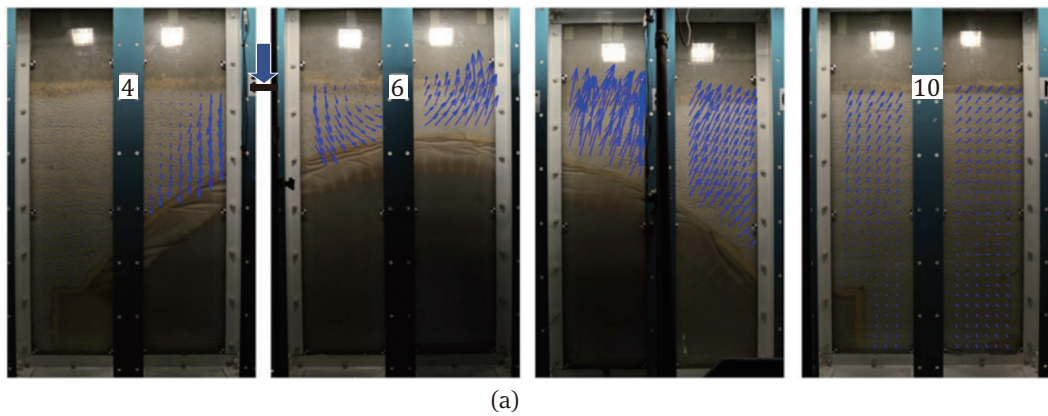


FIGURE 2.24: Four hinged failure mechanism for Salford arch bridge: (a) deformation of soil from PIV image; (b) DLO failure mechanism (e.g. mobilization factor of soil strength is 0.33)

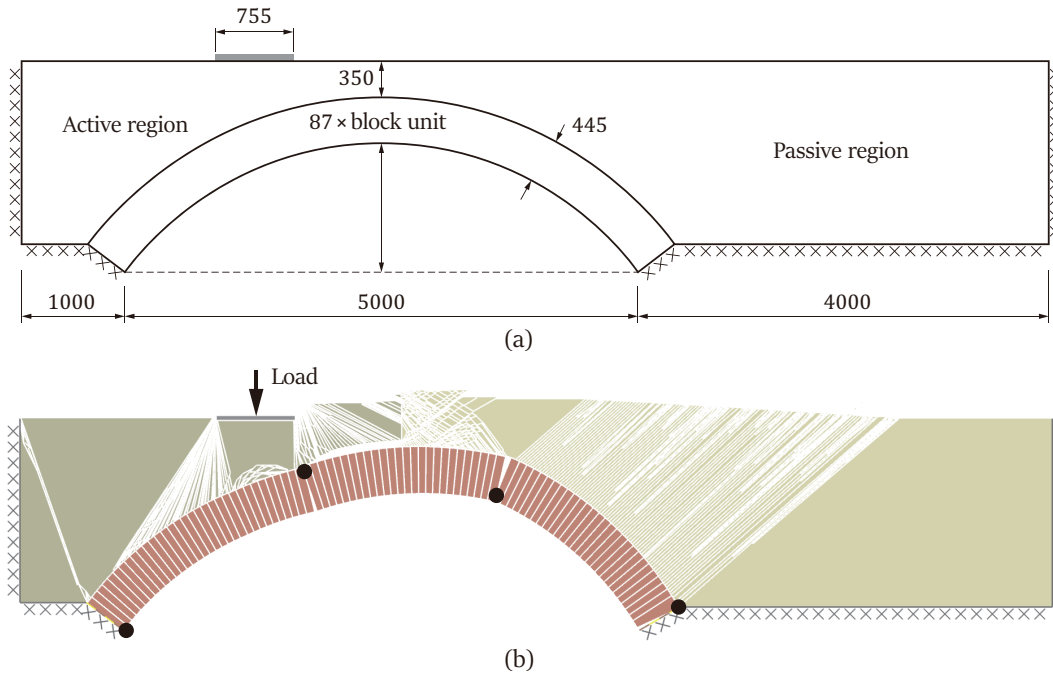


FIGURE 2.25: DLO model of Bolton arch bridge: (a) geometry dimensions (all dimensions in mm); (b) DLO output

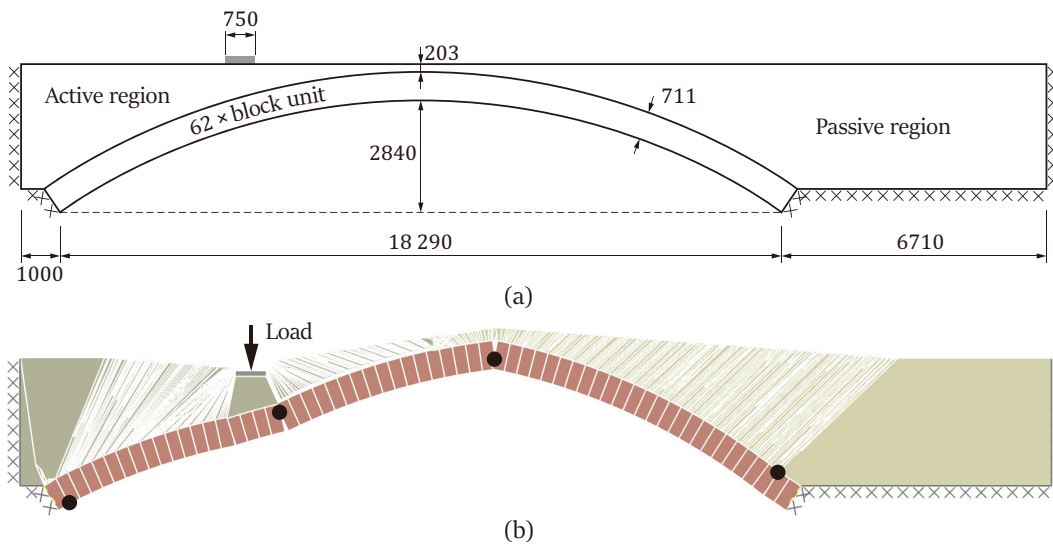


FIGURE 2.26: DLO model of Bridgemill arch bridge: (a) geometry dimensions (all dimensions in mm); (b) DLO output

For the Bolton and Bridgemill bridges, similar DLO models can be developed; see Figure 2.25(a) and 2.26(a) respectively. In this case a total of 5000 nodes were employed. The failure mechanisms identified are as shown in Figure 2.25(b) and 2.26(b).

## 2.5 Knowledge Gaps

At a strategic level, the knowledge gaps for the assessment of masonry arch bridges are as follows

- LimitState:GEO is a powerful DLO-based limit analysis software tool that can be used model masonry arch bridges. Masonry and soil elements can both be modelled directly. Introducing more nodes produces more accurate results, albeit at increased computational cost. In order to rapidly estimate the load-carrying capacity of masonry arch bridges where multiple load positions need to be considered, it would be useful to devise a means of reducing computational cost.
- Currently the LimitState:RING rigid block analysis tool uses a simplified indirect model of soil-arch interaction, considering dispersal of the applied load, self-weight and passive restraint. The current version of the software assumes that the effects of an applied load can be approximated using stress increments described by vertical Boussinesq stresses, with the horizontal and shear stresses neglected. However, the horizontal and shear stresses (e.g. along the extrados of an arch barrel) can be beneficial or detrimental depending on the scenario. According to lower-bound plastic theory, vertical, horizontal and shear stresses should all be considered. Incorporating proposed stress fields into LimitState:RING would therefore allow the software to furnish true lower-bound solutions at minimal additional computational cost.
- Using upper and lower bound analyses to bracket the true load carrying capacity is potentially computationally expensive considering that many load positions need to be considered; thus alternative strategies are worthy of consideration. The current version of LimitState:RING uses a 'Boussinesq' load dispersion model but the distribution is restricted by a dispersion angle. This is highly simplistic. In addition, 'Rankine' earth pressure is used to represent passive restraint but the principal soil pressure is restricted by direction. Thus a more realistic soil-arch interaction model is needed, to better simulate dispersal of the applied load and to represent soil earth pressures. Thus an alternative limit equilibrium method could provide a simple, effective and very fast alternative approach, potentially suitable for use in industry.

## **Part II**

# **Numerical Strategies**



## Chapter 3

# Computationally Efficient Upper Bound Method

### Preface

With the goal of developing a rapid and effective means of estimating the load-carrying capacity of masonry arch bridges, potential numerical limit analysis methods will be explored. Discontinuity layout optimization (DLO) is a useful limit analysis technique that can directly model both masonry and soil elements. Using DLO a given body is discretized using a suitable number of nodes laid out on a grid, with the failure mechanism deemed to comprise the slip-line pattern of potential discontinuities inter-connecting these nodes, identified using mathematical programming techniques. However, the computational cost of DLO is higher than the traditional rigid-block analysis method. Although coarse grid problems containing relatively few nodes often take only a few seconds to solve on a modern PC, introducing more nodes to produce more accurate results may significantly increase computational. In order to enhance the computational efficiency of the DLO limit analysis process, adopting an alternative nodal positioning strategy is considered in this chapter.

### 3.1 Introduction

Limit analysis provides a simple and effective means of estimating the load-carrying capacity of masonry arch bridges. Although empirical analysis methods are still used, a number of numerical limit analysis methods for masonry structures have been developed. However, most of these limit analysis methods only model the masonry elements directly, and the surrounding soil-fill is modelled indirectly. Because both masonry elements and soil-fill are important, the DLO technique has been proposed to model all elements directly. A key feature of DLO is that singularities can be modelled without difficulty, unlike with finite element limit analysis (e.g. Cavicchi and Gambarotta 2007), which needs to employ adaptive mesh refinement or high-order shape functions to obtain accurate solutions. However, arch bridge assessment typically involves consideration of many vehicle load positions, so computational cost becomes very important. Unfortunately the standard DLO procedure, although much less computationally expensive than incremental non-linear finite element methods, is still quite computationally expensive. Thus in this chapter, alternative nodal distribution strategies are considered.

### 3.2 Comparison of LimitState:GEO and LimitState:RING

LimitState:RING and LimitState:GEO are commercial software programs that can be used to estimate the load carrying capacity of masonry arch bridges. LimitState:RING models masonry elements using the rigid-block analysis method and adopts a simplified model strategy for the soil backfill, considering self-weight, live load dispersion and passive restraint. In contrast, LimitState:GEO utilises the upper-bound DLO limit analysis procedure to model both masonry and soil backfill elements directly. In order to develop a more computationally inexpensive DLO procedure, it is necessary to better understand what influences the computational cost.

#### 3.2.1 Arch Barrel Model

Initially, two models of the arch barrels of a bridge were developed to help establish the computational cost of the DLO procedure. Both were 3 m span arches with 0.75 m rise and 0.215 m thickness. The unit weight of masonry was  $23.7 \text{ kN/m}^3$ . Figure 3.1(a) shows  $12 \times$  block units in the arch barrel, with a total of 26 nodes and 39 discontinuities. The masonry in the arch is assumed to have infinite compressive strength and the structure is subject to a load positioned at quarter span. A series of contact discontinuities are available to model the opening of cracks. A four hinged arch failure mechanism is shown in Figure 3.1(b). Similarly, an arch barrel composed of masonry units with a finite compressive strength of  $1 \text{ N/mm}^2$  can be modelled. In order to allow crushing of the masonry to be simulated, regularly spaced nodes

(5 nodes along the radial face of each block) were used. Thus Figure 3.1(c) shows a model that comprises 65 nodes and 76 discontinuities. When the load is applied at 1/4 of the span in this case crushing can be approximately modelled using the DLO procedure, as shown in Figure 3.1(d).

When finite masonry crushing strength is specified in a rigid-block analysis model, an iterative analysis is required. In the iterative analysis the failure envelope is progressively refined using a series of linear constraints until the true non-linear failure envelope is properly represented (e.g. see Appendix A).

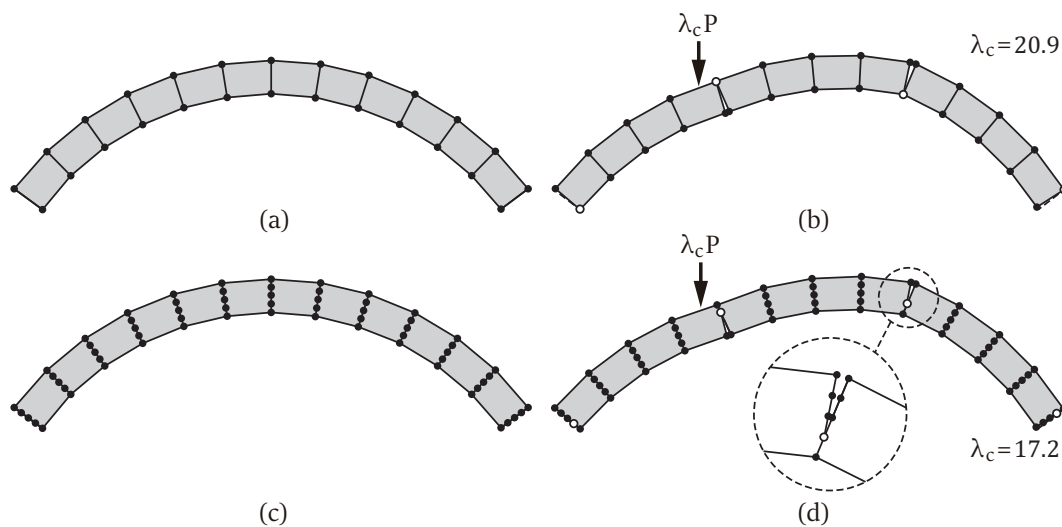


FIGURE 3.1: Arch barrel modelled using DLO: (a) arrangement of nodes (no crushing); (b) collapse mechanism corresponding to (a); (c) arrangement of nodes (with crushing); (d) collapse mechanism corresponding to (c) ( $P$  is a unit load)

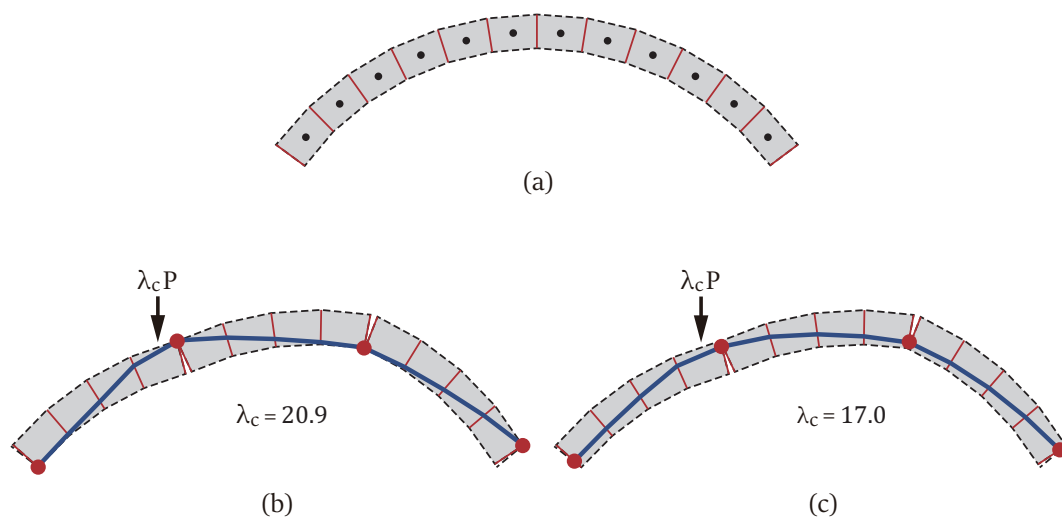


FIGURE 3.2: Arch barrel modelled using the rigid-block analysis method: (a) arrangement of masonry block elements; (b) failure mechanism (no-crushing); (c) failure mechanism (with crushing) ( $P$  is a unit load)

This means that compared with the DLO procedure, a much lower number of masonry elements are required in the rigid-block analysis model, contributing to the efficiency of the method.

### 3.2.2 Backfill Model

When the soil backfill located around the arch barrel is included the bridge model becomes more complex. Consider a bridge backfilled with a strong soil with a unit weight of  $19.1 \text{ kN/m}^3$ , soil friction angle of  $54.5^\circ$  cohesion of  $3.3 \text{ kN/m}^2$ , filled up to a level of  $0.3 \text{ m}$  above the crown. Assume that the soil-arch interface and passive soil strength mobilization factor multipliers are both taken as  $0.33$ . If the applied load is positioned at quarter span then there will be an active zone close to the applied load and a passive zone remote from the load. In the DLO model, soil regions are discretized using nodes, as shown in Figure 3.3(a). Potential discontinuities interlink these nodes to form the full limit analysis problem. Linear programming is used to identify the layout of the critical failure mechanism (shown in Figure 3.3(b)). In the case of the rigid-block model, dispersal of the applied load through the backfill is modelled, as is passive resistance, as shown in Figure 3.4, so the computational cost of this model is virtually 'free'. Figure 3.3(b) shows a coarse grid (250 nodes used) in DLO procedure, but increasing the number of nodes delivers a more accurate result.

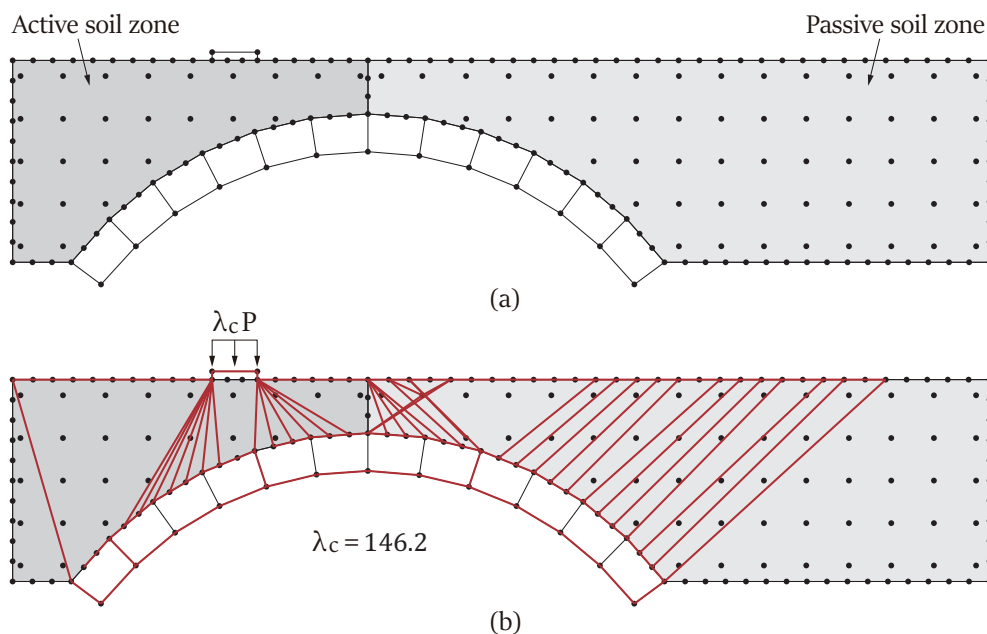


FIGURE 3.3: Backfilled arch bridge model using the standard DLO procedure (DLO-standard): (a) nodal discretization; (b) slip-lines ( $P$  is a unit load)

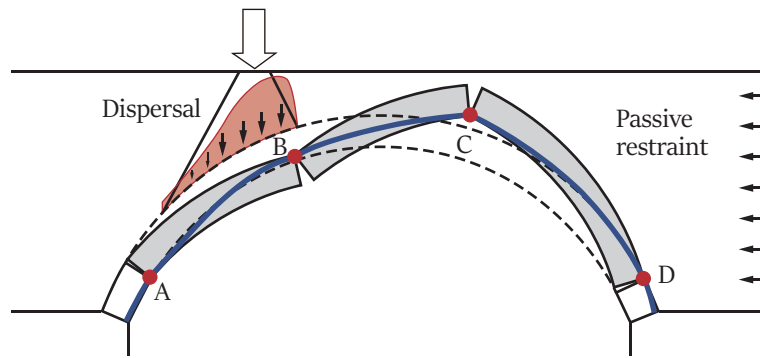


FIGURE 3.4: Soil model in rigid-block analysis

### 3.2.3 Commentary

By considering both LimitState:GEO and LimitState:RING models, contributors to their respective computational costs have been established. If a large number of nodes is used in the DLO model (e.g. 6000), then a more accurate predicted bridge load-carrying capacity (123 kN) is obtained than when using a coarse nodal grid (capacity = 146 kN). However, its computational cost is also significantly increased.

To obtain the solutions a 2.2 GHz Intel Core PC equipped with 8 GB of memory, running under 64 bit Windows 10 Professional. Mosek version 7.0, a commercially available interior point LP solver was used. Quoted CPU times involve the time required to make all connections between nodes and to solve the LP problem. In this case, the CPU time comparison between DLO and rigid-block analysis results is listed in Figure 3.5. The LimitState:RING bridge collapse load was in this case 122 kN.

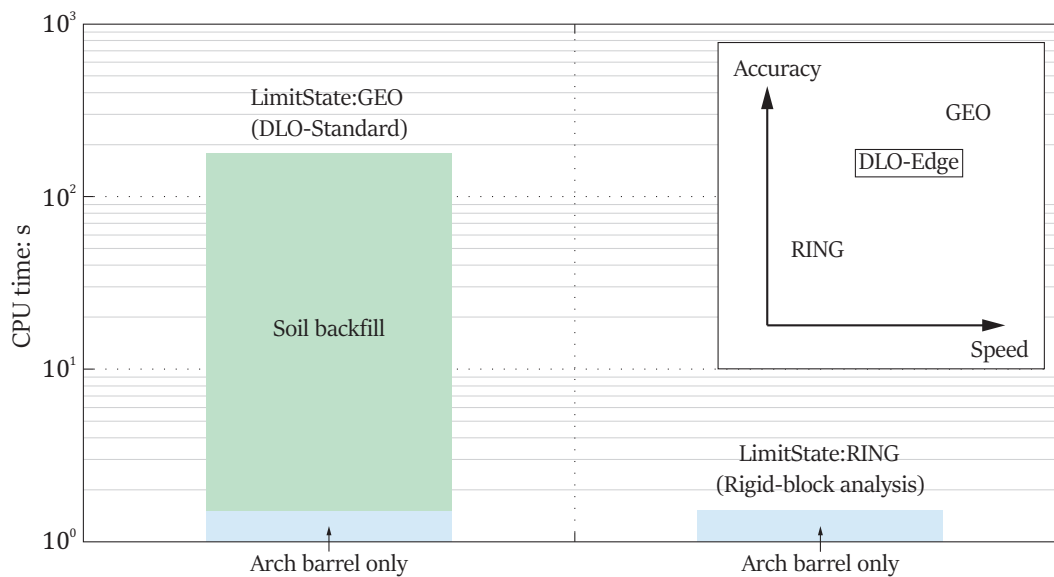


FIGURE 3.5: CPU time comparison between 'DLO-standard' and rigid-block analysis results

From Figure 3.5, it can be seen that the difference between the LimitState:GEO (220s) and LimitState:RING (1.5s) CPU times is caused by the computational expense associated with the soil backfill model. If a new DLO procedure can be devised to improve computational efficiency then the LimitState:GEO can be faster running, facilitating the analysis of masonry arch bridges subject to axle loads that move across the bridge, generating many load cases.

### 3.3 Fast Running Discontinuity Layout Optimization

In order to improve the computational efficiency of the original DLO procedure, a fast running DLO procedure will be proposed to assess the safety of masonry arch bridges. The 'DLO-edge' procedure will be similar to the 'DLO-standard' procedure; both are outlined diagrammatically in Figure 3.6. With DLO-edge a limit analysis problem is also formulated in terms of the potential discontinuities that interlink nodes used to discretize the solid body under consideration. However, the nodes used in the DLO-edge are only placed along the edges of the given body.

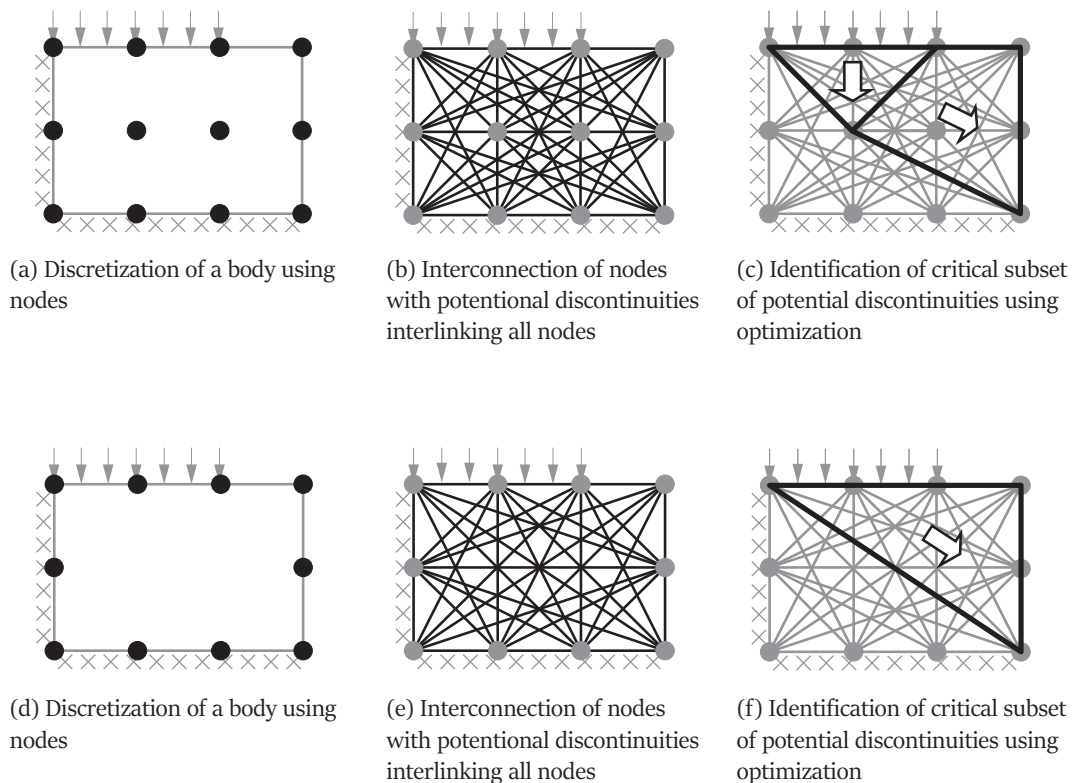


FIGURE 3.6: Stages in the DLO procedure: (a) ~ (c) for DLO-standard; (d) ~ (f) for DLO-edge

### 3.3.1 Simple Example

In order to demonstrate the computational efficacy of DLO-edge a simple example problem will be considered. The example is a planar limit analysis problem. Figure 3.7 shows a  $3 \times 2$  unit design domain and also indicates the support and load conditions. The locations of nodes are indicated and each node is connected to every other node by a potential discontinuity.

Figure 3.7(a) shows two wedges, with the critical layout of slip-line discontinuities obtained using the standard DLO procedure. Figure 3.8(a) presents a velocity diagram for the virtual displacements of the two wedges and a 'rigid' load. In the problem the self weight of soil is for simplicity ignored. There is assumed to be zero cohesion along the free boundaries and unit cohesion along the fixed boundaries. In accordance with the upper bound theorem, the total internal energy dissipated is equal to the total external work done. Thus the work equation can be expressed as:

$$c_u \sqrt{2} \cdot \sqrt{2}\delta + c_u \sqrt{5} \cdot 1.4907\delta + c_u \sqrt{2} \cdot 0.4714\delta = V 2 \cdot \delta \quad (3.1)$$

where  $c_u$  is the undrained cohesion of the soil body;  $\delta$  is the virtual displacement of the slip-line discontinuity;  $V$  is the applied load at the foundation. Calculating the equation 3.1, the collapsed load  $V_c$  is equal to 3 in this case.

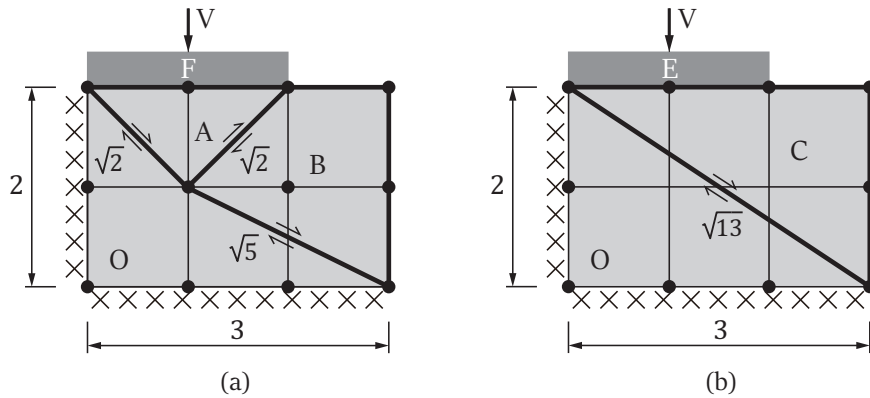


FIGURE 3.7: Analogy between standard and fast DLO: (a) standard DLO; (b) fast DLO

Figure 3.7(b) shows one wedge with the critical layout of slip-line discontinuities obtained using the fast DLO procedure. Figure 3.8(b) represents a velocity diagram for the virtual displacements of a wedge and a load. The material properties and boundary conditions in this case are same as for standard DLO. According to the upper bound theorem, the work balance equation can be expressed as:

$$c_u \sqrt{13} \cdot \sqrt{3.25}\delta = V 2 \cdot \delta \quad (3.2)$$

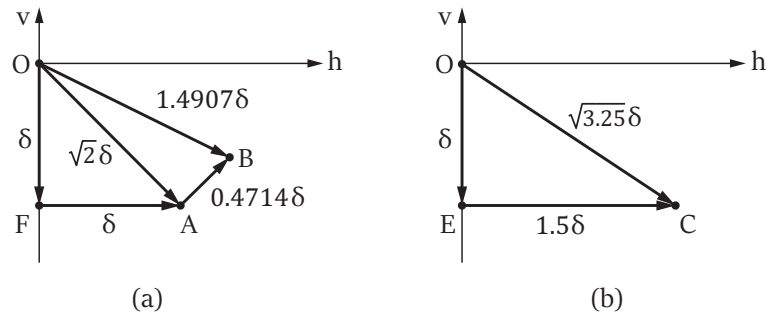


FIGURE 3.8: Hodograph and Maxwell force diagrams: (a) standard DLO; (b) fast DLO

Thus the collapse load  $V$  in this case is equal to 3.25. These solutions in the two cases can be also obtained using the LP solver. The accuracy of the fast DLO in the problem is equal to  $(3.25 - 3)/3 = 0.0833$  which is potentially acceptable (since it is  $< 10\%$ ).

In fact the total number of possible discontinuities, including overlapping discontinuities, can be shown to be  $m = n(n - 1)/2$ . In the DLO-standard model, the number of discontinuities is equal to  $12 \cdot (12 - 1)/2 = 66$ ; in contrast, the number of DLO-edge discontinuities is  $10 \cdot (10 - 1)/2 = 45$ . If the number of nodes employed is a very large value, the difference in computational cost between DLO-standard and DLO-edge will become very large.

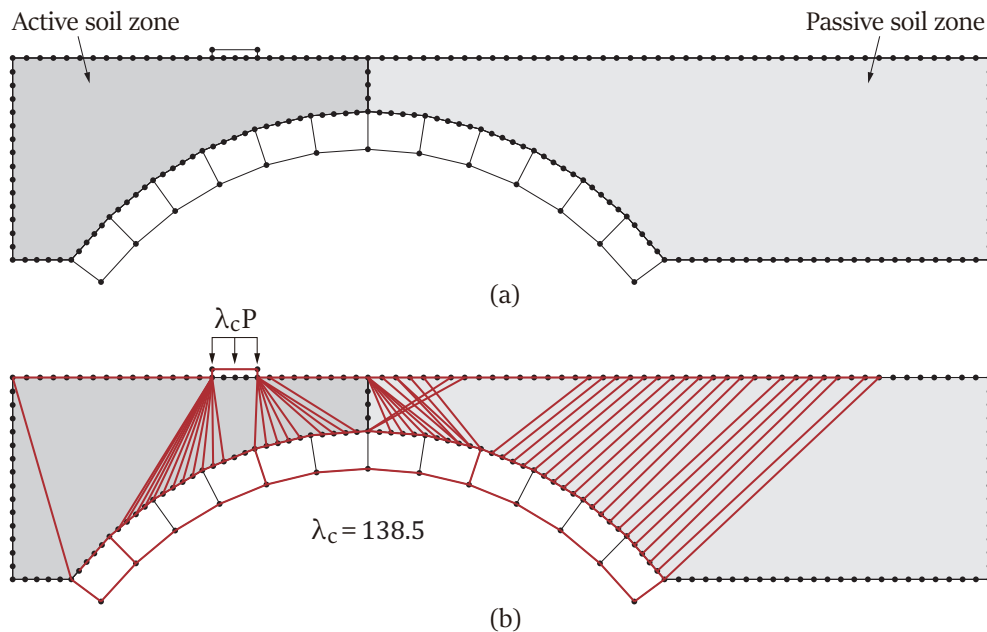


FIGURE 3.9: Backfilled arch bridge modelled using DLO-edge strategy: (a) nodal discretization; (b) slip-lines ( $P$  is a unit load)

### 3.3.2 Typical Example of Backfilled Masonry Arch Bridge

Following the description of the proposed DLO-edge procedure in the previous section, the backfilled masonry arch bridge problem considered previously can be revisited, though with nodes used in the backfill model now only placed at the edges of the solid regions, as shown in Figure 3.9. Using the same number of nodes as before, the predicted failure load of the bridge using DLO-edge is 138.5 kN versus 146.2 kN when using DLO-standard. If an increased number of nodes is used, an improved DLO-edge solution will be obtained (i.e. a solution with a reduced load factor). It is therefore useful to ascertain the extent to which the DLO-edge procedure can be used to reduce the total CPU time required to achieve a solution of a given accuracy. Table 3.1 and Figure 3.10 show results for the backfilled masonry arch bridge problem, indicating that use of the DLO-edge procedure can indeed reduce the number of nodes used required to give a solution of a given accuracy.

TABLE 3.1: Influence of number of using nodes

DLO-standard			DLO-edge		
No. of nodes	Load factor (error)	CPU seconds	No. of nodes	Load factor (error)	CPU seconds
500	138.1 (28.0%)	2.71	500	130.2 (16.4%)	2.56
1000	129.8 (11.7%)	4.98	1000	125.6 (5.15%)	5.27
5000	123.6 (3.20%)	120	1500	123.2 (2.66%)	14.9
10000	122.3 (1.33%)	330	2000	122.3 (1.33%)	25.8

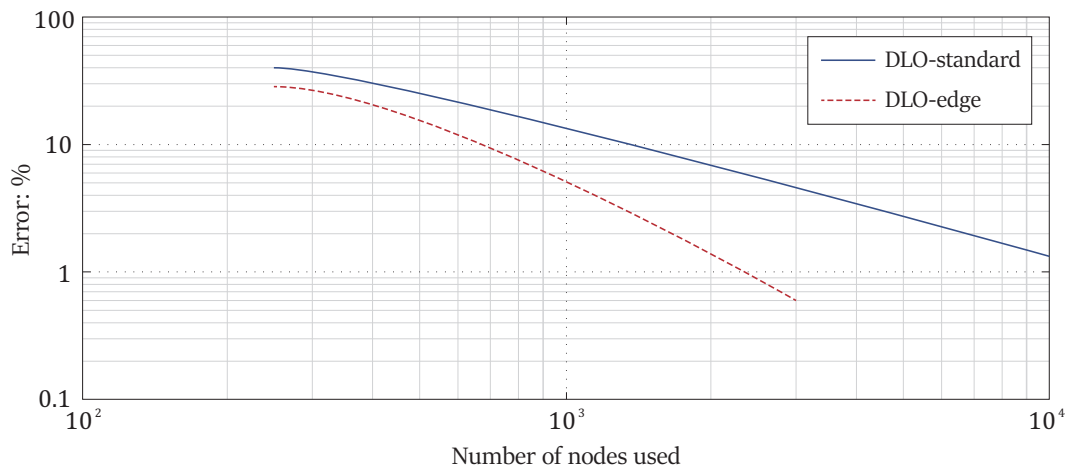


FIGURE 3.10: Number of nodes used vs. percentage error when using DLO-standard and DLO-edge

In Figure 3.10, it can be seen that DLO-edge provides a reasonably rapid means of the analysing bridges. Although the rigid-block analysis method is still faster, the range of the application is restricted by the highly simplified backfill model used. DLO-standard is a rigorous upper-bound method to model arch bridges, but the computational time is high if a high degree of accuracy is required. Potential advantages of DLO-edge will be illustrated by considering its application to three literature arch bridges in the next section, with multiple load positions employed.

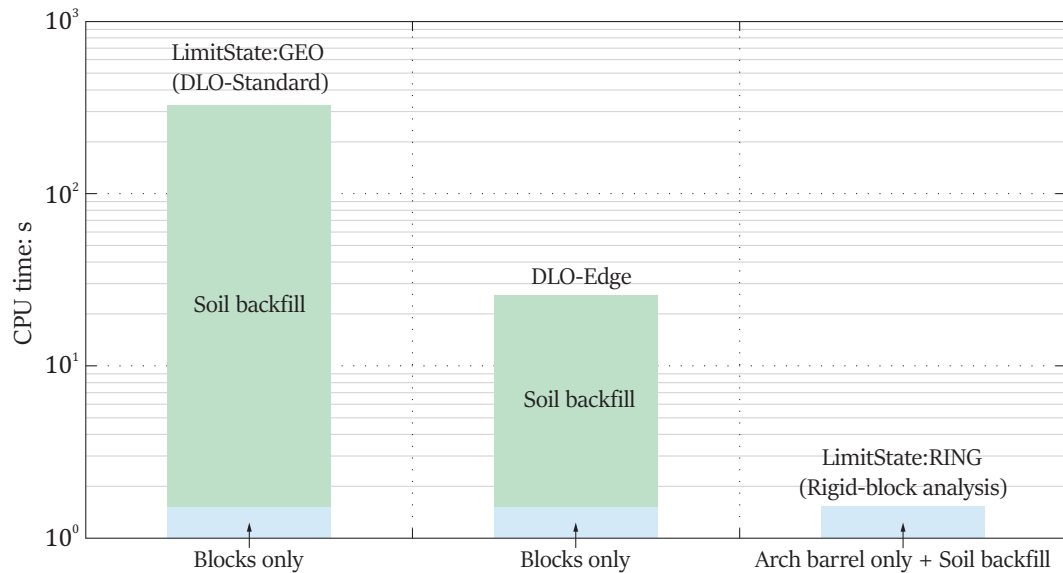


FIGURE 3.11: CPU time comparison of DLO-standard, DLO-edge and rigid-block analysis

For a single load case and fixed 1.33% error, Figure 3.11 indicates that the difference between the current version of LimitState:GEO (330 s) and fast running DLO (25.8 s) CPU times is also caused by the computational expense associated with the soil backfill model.

### 3.4 Application to Case Studies

The use of the DLO-edge method can be illustrated by using it to model the Bolton, Salford and Bridgemill arch bridges. The geometry and main properties are shown in section 2.4 of the thesis. In order to provide reasonable accuracy, 2000 nodes were used in the DLO-edge models. Results from DLO-edge can be used to compare with DLO-standard (LimitState:GEO) and LimitState:RING results. The number of nodes used in LimitState:GEO using DLO-standard model was 5000.

Predicted failure mechanisms obtained using DLO-edge and DLO-standard are shown in Table 3.2, considering quarter span loading. Considering CPU time, it is evident that DLO-standard models take a longer time to solve, and in these cases obtain solutions that are less accurate than the DLO-edge results.

TABLE 3.2: Comparison of DLO-standard and DLO-edge in bridges (5000 nodes used in DLO-standard, 1500 nodes used in DLO-edge)

Problem	LimitState:GEO CPU time (s)	DLO-Edge CPU time (s)	Speed up
Bolton arch	14532	684	21.25
Salford arch	12020	621	19.36
Bridgemill arch	13836	669	20.68

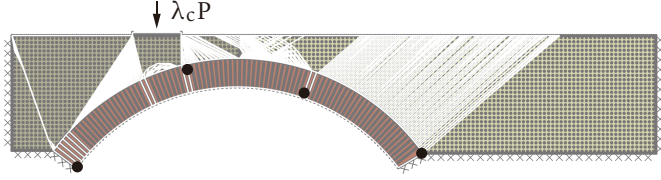
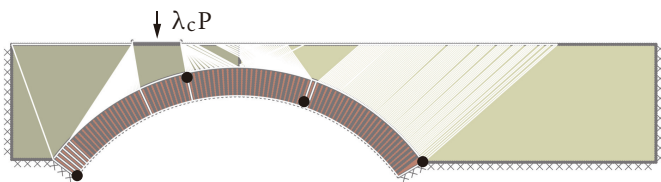
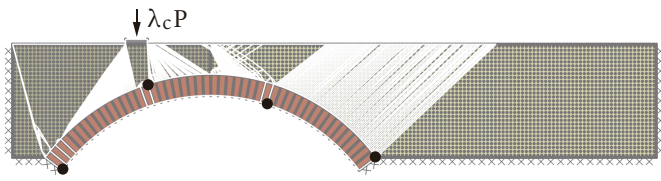
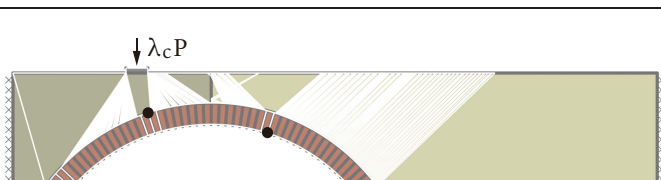
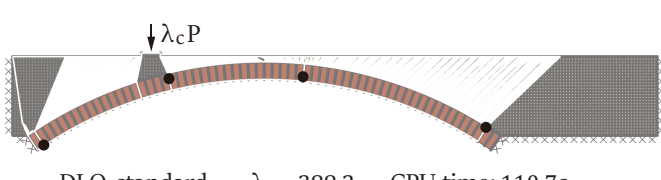
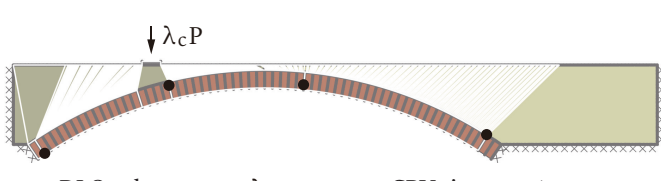
TABLE 3.3: Comparison of DLO-edge and rigid-block analysis in bridges (1500 nodes used in DLO-edge)

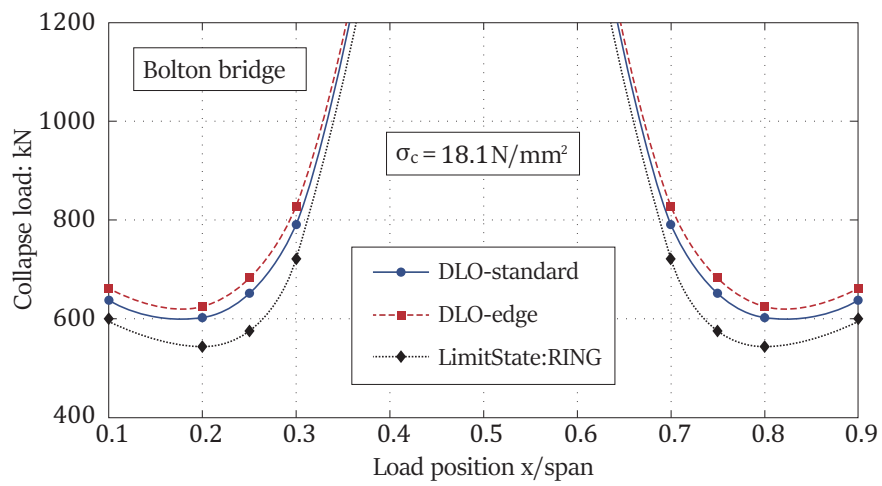
Problem	DLO-Edge CPU time (s)	LimitState:RING CPU time (s)	Speed up
Bolton arch	684	106	6.45
Salford arch	621	95	6.54
Bridgemill arch	669	101	6.62

If a hundred load positions are considered, moving the load from the left to the right abutment, the cumulative CPU time difference between the LimitState:RING, LimitState:GEO and DLO-edge models is relatively large. Figure 3.12 shows horizontal profiles of the collapse load along the extrados of each arch barrel. The weak position for each bridge ranges from 0.2 to 0.3 of the  $x$ /span (where  $x$  is measured from the left abutment to the load position) or from 0.7 to 0.8. In order to efficiently manage computational cost, a hundred load position cases were run using 1500 nodes.

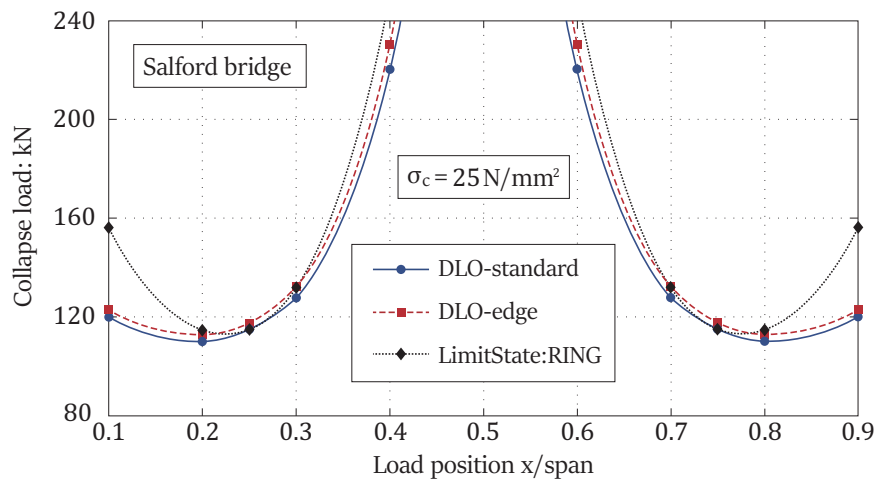
Table 3.2 shows that the time consumed by LimitState:RING for this problem is around 100 seconds, with a single load position case requiring approximately one second to run. In contrast, the time consumed by LimitState:GEO was very high, exceeding ten thousand seconds. Table 3.3 shows that the time required to consider the six additional load positions cases was around 650 seconds. Table 3.2 and 3.3 also show the speed up using LimitState:GEO CPU time divided by DLO-edge and using DLO-edge CPU time divided by LimitState:RING. For this hundred load position problem, the run time for DLO-edge is much lower than that required to run the corresponding LimitState:GEO models. Although the CPU time associated with DLO-edge is higher than that associated with LimitState:RING, the range of application of DLO-edge is wider, since LimitState:RING only provides reasonable results when the load is at or near the quarter span of the bridge.

TABLE 3.4: DLO-standard and DLO-edge solution of bridges ( $P$  is a unit load)

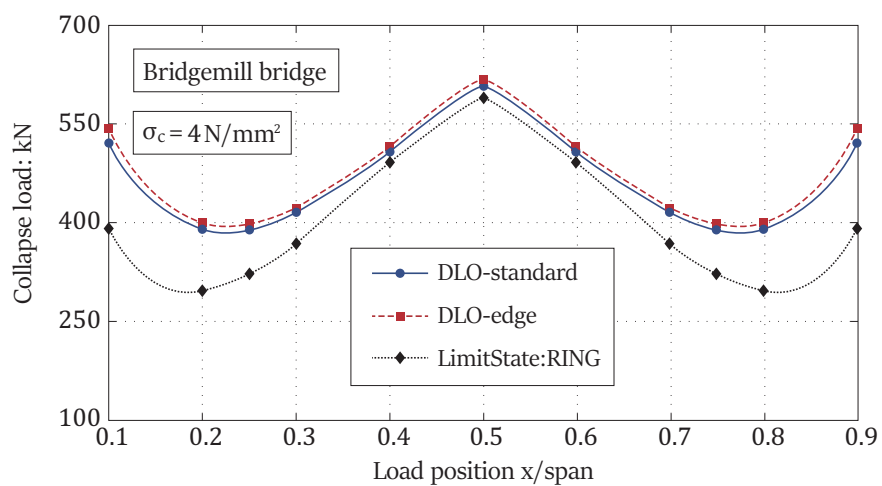
Problem	DLO solution
Bolton arch bridge: 5000 nodes used in DLO-standard; 2000 nodes used in DLO-edge.	 <p>DLO-standard    <math>\lambda_c = 648.4</math>    CPU time: 146.8s</p>  <p>DLO-edge    <math>\lambda_c = 636.4</math>    CPU time: 32.6s</p>
Salford arch bridge: 5000 nodes used in DLO-standard; 2000 nodes used in DLO-edge.	 <p>DLO-standard    <math>\lambda_c = 116.2</math>    CPU time: 126.9s</p>  <p>DLO-edge    <math>\lambda_c = 114.1</math>    CPU time: 27.9s</p>
Bridgemill arch bridge: 5000 nodes used in DLO-standard; 2000 nodes used in DLO-edge.	 <p>DLO-standard    <math>\lambda_c = 388.2</math>    CPU time: 110.7s</p>  <p>DLO-edge    <math>\lambda_c = 381.8</math>    CPU time: 23.5s</p>



(a)



(b)



(c)

FIGURE 3.12: Load-carrying capacity at different load position (5000 nodes used in DLO-standard, 1500 nodes used in DLO-edge): (a) Bolton bridge; (b) Salford bridge; (c) Bridgemill bridge

### 3.5 Discussion

The literature bridge examples considered thus far assume that fixed abutments are used to support each bridge. However, bridge abutments are in reality often ‘free’, which allows them to slide into the backfill. Although differences in the predicted collapse loads for bridges that have fixed or free abutments may often be small (e.g. see Gilbert et al. 2010), considering free abutments in the analysis presents an issue for the DLO-edge model.

The Salford arch bridge is here chosen to illustrate the application of DLO-edge for the analysis of arch bridges with free abutments. The geometry of the bridge is shown in Figure 2.19 from section 2.4.2, and the main material properties are the same as for the Salford arch bridge considered previously.

If a live load is applied at quarter span, it is found that an abutment remote from the load slides into the fill and three hinges form in the arch barrel. Figure 3.13(a) shows the bridge failure mechanism obtained using DLO-standard and the predicted collapse load is 88.1 kN lower than the 116.2 kN that could be carried when using fixed abutments. In the passive region of the backfill, the soil failure surface is initially a log-spiral curve, and then a straight slip-line from the abutment up to the traffic surface. If DLO-edge is used to analyse this bridge the nodes are placed only at the edges of the geometrical regions, as shown in Figure 3.13(b). However, the predicted capacity is 100 kN, which is higher than the DLO-standard result. This is because the family of potential discontinuities present in the DLO-edge model are not able to simulate the log-spiral failure surface.

If two are added at the bottom of the abutments and are discretized with nodes, then DLO-edge can approximately model the log-spiral rupture surface, as shown in Figure 3.14. The predicted collapse load in this DLO-edge scenario becomes 90.5 kN which is now close to the DLO-standard result.

Now consider the same bridge for multiple load positions, with free and fixed abutments. The numbers of nodes used in DLO-standard and DLO-edge were 5000 and 2000 respectively. A relationship of collapse load versus load position/span is presented in Figure 3.14. For the bridge with fixed abutments, differences between the DLO-standard and DLO-edge solutions are relatively small. However for the bridge with free abutments the difference becomes larger, at 8% (DLO-standard vs. DLO-edge).

Although the DLO-edge method does have difficulty identifying the curved slip-line pattern associated with local failure in a problem, this can be alleviated by adding suitable lines into a DLO-edge model.

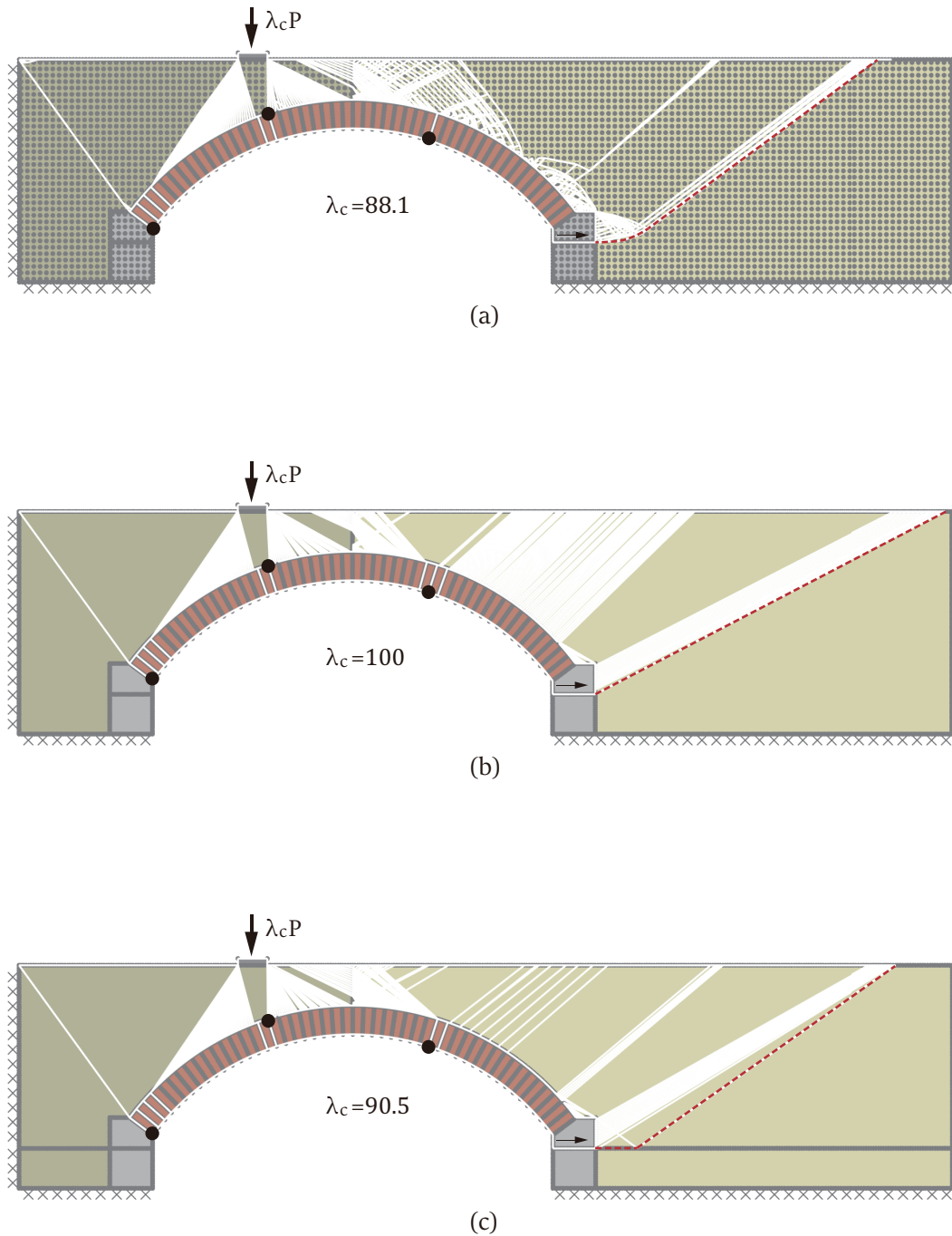


FIGURE 3.13: Failure mechanisms of bridge which had free abutments: (a) DLO-standard output; (b) DLO-edge scenario I; (c) DLO-edge scenario II ( $P$  is a unit load)

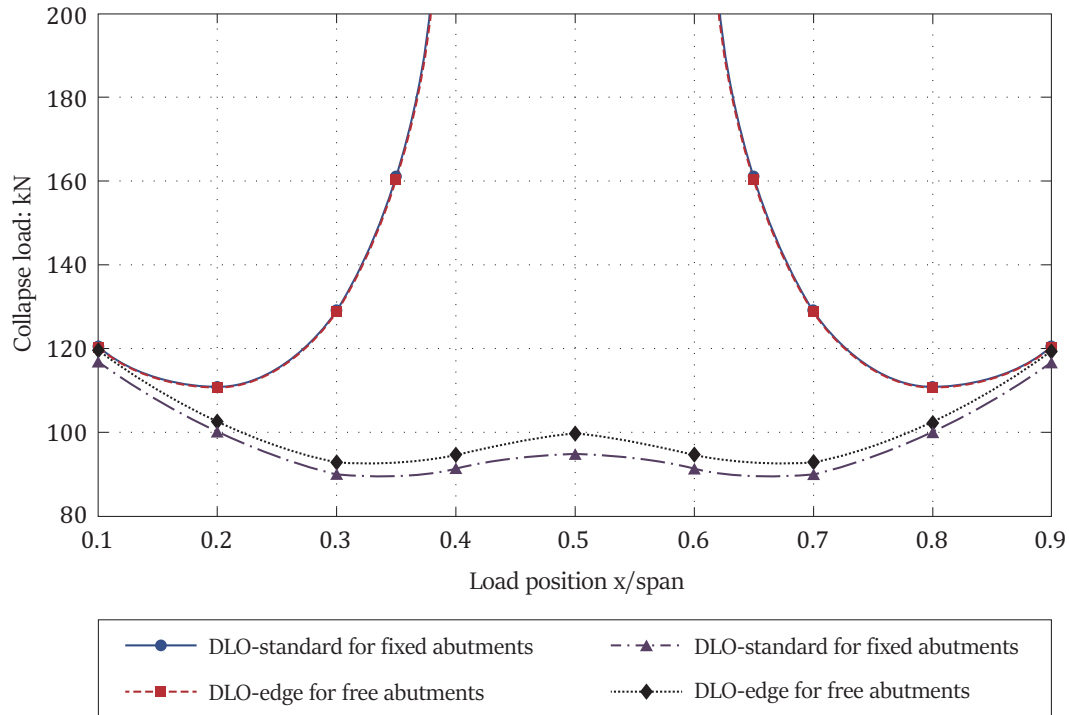


FIGURE 3.14: Collapse load vs. load position/span

### 3.6 Concluding Remarks

In summary:

- A fast running discontinuity layout optimization (DLO-edge) limit analysis procedure has been introduced to reduce the computational cost of analysing masonry arch bridges. To save time, an alternative nodal discretization strategy has been proposed, in which nodes are only placed at edges of solid regions. Results from DLO-edge have been compared with results from the standard DLO procedure and high-quality data obtained from laboratory tests on full-scale masonry arch bridges.
- The DLO-edge procedure has also been applied to more complex arch bridge problems where failure mechanisms have been found that are in good agreement with the solutions from a standard DLO analysis containing a suitably larger number nodes. In order to provide acceptable results for problems involving multiple load positions, an increased number of nodes can be used for the positions found to be most critical in an initial analysis. The computational cost of DLO-edge has been compared with that of the current version of the LimitState:GEO and LimitState:RING commercial limit analysis software tools.

## Chapter 4

# Lower Bound Stress Fields Method

### Preface

With the goal of developing rapid and effective means of estimating the load-carrying capacity of masonry arch bridges, potential strategies employing numerical limit analysis methods are explored. One strategy involves lower bound limit analysis. Whilst most available arch analysis tools (e.g. Obvis 2016, LimitState 2019*b*) model the masonry elements explicitly, soil-fill material is normally modelled in an indirect manner, with the anticipated effects of the soil-fill (self-weight, load dispersion and passive restraint) only approximately represented. Although it is possible to model the soil-fill explicitly in a numerical limit analysis model, e.g. via use of finite element limit analysis (Cavicchi and Gambarotta 2007, Gilbert et al. 2007) or discontinuity layout optimization (Smith and Gilbert 2007, Gilbert et al. 2010), additional computational costs are incurred. Therefore, closed form lower bound stress fields combined with numerically modelled arch elements are proposed to obviate the need for potentially computationally costly analyses, permitting rapid estimation of the load-carrying capacity of soil-filled masonry arch bridges.

## 4.1 Introduction

Lower bound limit analysis is useful to predict the largest loads that a plastic system can sustain without failure. The loads are determined from stress fields which satisfy the equilibrium, stress boundary conditions and nowhere violate yield. The challenge is to generate the stress fields for soil-filled masonry arch bridges, modelling both soil and masonry elements.

Rigid-block limit analysis has been previously applied to masonry arch barrels (Gilbert and Melbourne 1994) and when a LP solver is used to obtain a solution then this will simultaneously be a lower and upper bound for the given discrete blocks. Thus the arch structures can be straightforward modelled approach using rigid-block analysis. For the soil-fill components, combinations of lower bound stress fields are proposed that superimpose the distributions due to live loads and simple stress fields which combine to make the effect of surface loads on the extrados of a masonry arch.

In the soil model, the Mohr-Coulomb criteria is used. In the masonry model, the compressive strength is considered. If a stress field of masonry exceeds the crush compression, it means the stress distribution yields.

In this chapter, the lower bound stress fields applicable to masonry and soil will be introduced, then the model is applied to soil-filled masonry arch bridges, with results compared with the upper bound solutions obtained using DLO limit analysis procedure.

## 4.2 Masonry Stress Fields

To generate a lower bound in the arch, a rigid block assemblage is assumed for a masonry structure. For the sake of simplicity, infinite compressive strength is assumed in this chapter. It gives no consideration for any stress fields inside of each masonry block, but it is necessary to know the stress distributions at each contact between adjacent blocks. A solution in a critical failure mechanism of a masonry arch bridge using rigid-block analysis gives shear force  $S$ , normal force  $N$  and moment  $M$  at each contact. These forces can be used to obtain valid lower-bound stress distributions along each contact.

Stress distribution at cross-section is assumed as linear. The normal force  $N$  and moment  $M$  at each contact can be used to calculate the normal stress  $\sigma$  over the cross-section of the arch at the contact. Similarly, the shear force  $S$  can be used to calculate the shear stress  $\tau$  over the cross-section of the arch. Thus there are two cases to show the stress distribution, involving Case A of non-crack as shown in Figure 4.1(a) and Case B of crack as shown in Figure 4.1(b). In order to guarantee

nowhere yielding in the masonry model, all normal and shear stresses should be lower than the compressive and shear strength at each contact. The procedures for equating the largest value of these stresses are as follows

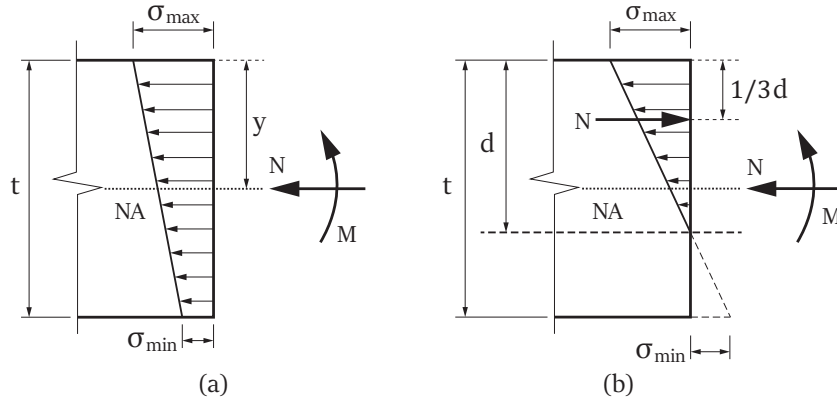


FIGURE 4.1: Contact stress distribution: (a) non-crack; (b) crack

- (i) For each contact  $i$ , initially compute the minimum normal stress  $\sigma_{min}$  to determine the stress distribution. If  $\sigma_{min}$  is larger than zero, it means 'no-tension' at the contact; in contrast, if  $\sigma_{min}$  is lower than zero, a crack will occur at the contact. In accordance with the assumption of linear distribution, the minimum normal stress can be written as

$$\sigma_{min} = \frac{N}{wt} - \frac{My}{I} \quad (4.1)$$

where  $t$  is the height of the cross-section;  $w$  is the width of the cross-section;  $I$  is the second moment of area of the cross-section;  $y$  is the distance between the neutral axis and the top edge of the cross-section.  $\sigma_{max}$  is always larger than  $\sigma_{min}$ .

- (ii) Calculate the largest value of normal and shear stress at each contact.

For Case A,  $\sigma_{min}$  is larger than zero, thus no-crack occurs at the contact. The maximum normal stress at the contact can be expressed as

$$\sigma_{max} = \frac{N}{wt} + \frac{My}{I} \quad (4.2)$$

For Case B,  $\sigma_{min}$  is lower than zero, thus the crack occurs at the contact and the stress distributions will be rearranged. Taking the moment at the top edge of the cross-section, the moment equilibrium can be written as

$$N \cdot \frac{d}{3} = N \cdot \frac{t}{2} - M \quad (4.3)$$

Deriving this equation, the no-crack length can be written as

$$d = \frac{3}{2}t - 3\frac{M}{N} \quad (4.4)$$

Taking the force equilibrium, the maximum normal stress can be derived as

$$\sigma_{max} = \frac{2N}{wd} \quad (4.5)$$

In accordance with 'no-sliding' constraint for plastic analysis, yield inequality gives as follows

$$S \leq N\mu + c'd \quad (4.6)$$

where  $\mu$  is the joint frictional coefficient and  $c'$  is the cohesion. Considering yield factor  $\zeta$ , the yield constraint can be expressed as

$$\zeta \leq \frac{S}{N\mu + c'd} \quad (4.7)$$

The lower-bound stress fields of masonry can be illustrated by considering an example of arch barrel. The geometry of the arch barrel is shown in Figure 4.2(a). An axle load is acted at the quarter span of the arch barrel. The unit weight of the masonry is assumed as  $23.7 \text{ kN/m}^3$  and the joint frictional coefficient  $\mu$  is 0.66. Numerical failure mechanism obtained from rigid-block analysis is presented in Figure 4.2(b). The estimation of the arch load-carrying capacity is 18.9 kN. The computed no-crack length  $d$ , maximum normal stress  $\sigma_{max}$  and shear stress  $\tau_{max}$  at each contact are shown in Table 4.1. According to Mohr-Coulomb yield criteria,  $S \leq N\mu$  for no cohesion at contact, it is clearly to know from this table that nowhere violate yield.

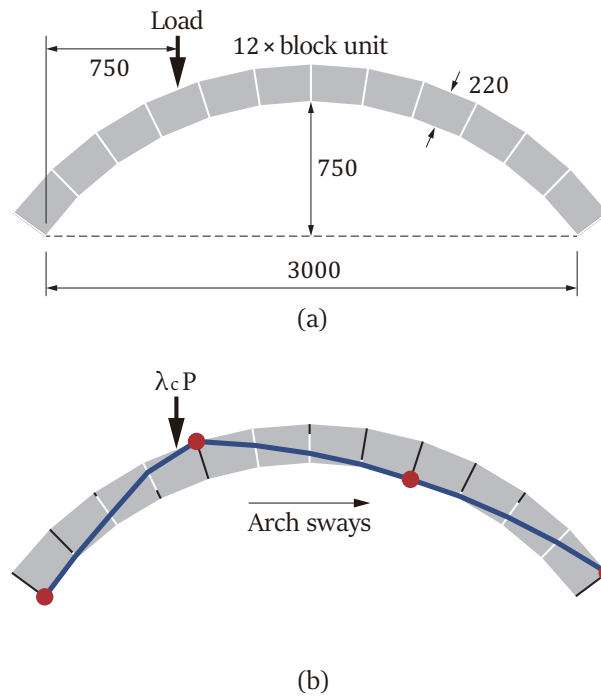


FIGURE 4.2: Example of an arch barrel: (a) geometry of an arch barrel (all dimensions in mm); (b) failure mechanism ( $P$  is a unit load)

TABLE 4.1: Results of an arch barrel

Contact	S (kN)	N (kN)	M (kN m)	$d$ (m)	$\sigma_{\max}$ (kN/m <sup>2</sup> )	$ S/N $
0	0.17	29.76	3.27	0.00	$\infty$	0.01
1	-3.45	28.49	2.76	0.04	1424.5	0.12
2	-6.70	26.84	1.19	0.20	268.4	0.25
3	-9.55	24.89	-1.31	0.17	292.8	0.38
4	6.03	16.96	-1.87	0.00	$\infty$	0.36
5	4.67	17.48	-0.22	0.22	52.2	0.27
6	3.27	17.99	1.00	0.16	224.9	0.19
7	1.79	18.49	1.77	0.04	924.5	0.10
8	0.20	18.95	2.08	0.00	$\infty$	0.01
9	-1.51	19.36	1.89	0.04	968	0.08
10	-3.38	19.67	1.14	0.16	245.9	0.17
11	-5.40	19.86	-0.20	0.22	65.5	0.27
12	-7.59	19.87	-2.19	0.00	$\infty$	0.38

### 4.3 Soil Stress Fields

#### 4.3.1 Introduction

The challenge is to find a stress field in the soil-fill due to an applied surface load that is a true lower bound solution. When a vehicle traverses a masonry arch bridge, each wheel of the vehicle applies a load to the level traffic surface and will be assumed to be uniform. For the sake of simplicity, a single load only is considered in this chapter.

If a single load is applied at the quarter span of a masonry arch bridge (e.g. shown as Figure 4.3), the collapsed mechanism (upper bound solution) is a typical four hinged mechanism as shown in Figure 4.4. The active zone is specified on the loading side. In contrast, the passive zone is on the side of the arch ring moving into the fill. The surface layer is on the crown of the arch ring. Because the road on a masonry arch bridge has strong strength, the road with depth  $S_C$  was assumed to be cemented material.

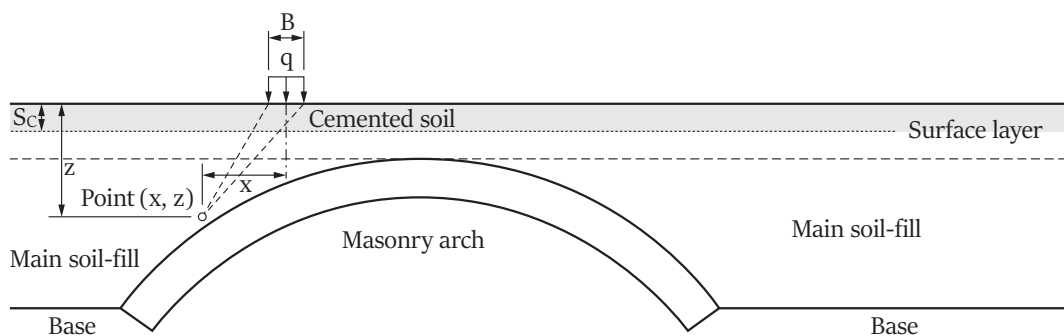


FIGURE 4.3: Lower bound stress fields due to live load

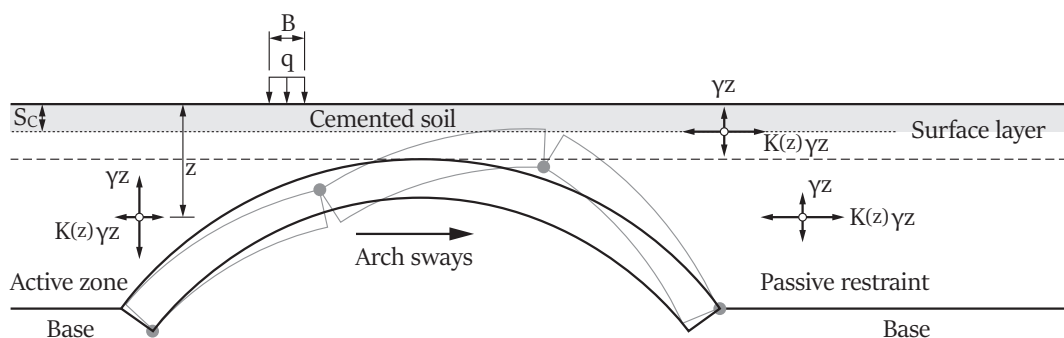


FIGURE 4.4: Lower bound stress fields due to dead load

## 4.3.2 Stress Fields Due to Surface Load

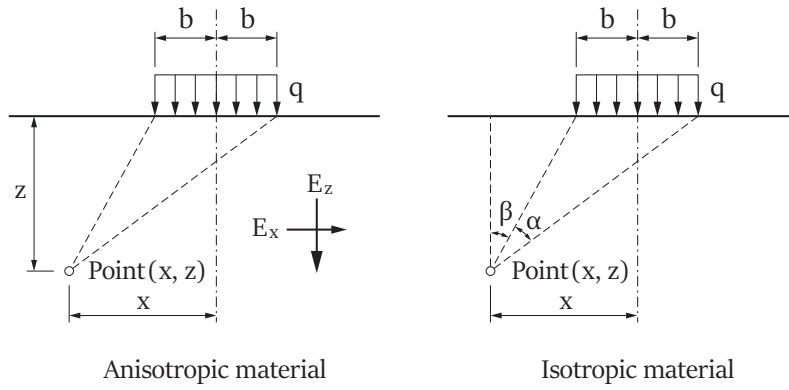


FIGURE 4.5: Cross section through long flexible strip on infinite soil carrying surcharge  $q$

In this work, equilibrium stress fields used an anisotropic 'Boussinesq' distribution (1877) are adopted as the part of a lower bound solution. The degree of the anisotropy is evaluated by means of the Young's modulus ratio  $n = E_x/E_z$ , where  $E_z$  and  $E_x$  are the elastic modulus in the vertical and horizontal direction respectively (e.g. shown as Figure 4.5). The stress formulae (e.g. see Appendix C) under a uniformly distributed load were introduced by Moroto (1973) as follows

$$\begin{cases} \Delta\sigma_z = \frac{q}{\pi} \frac{1}{\eta_2 - \eta_1} (\eta_2 k_1 - \eta_1 k_2) \\ \Delta\sigma_x = \frac{q}{\pi} \frac{\eta_1 \eta_2}{\eta_2 - \eta_1} (-\eta_1 k_1 + \eta_2 k_2) \\ \Delta\tau_{xz} = \frac{q}{2\pi} \frac{\eta_1 \eta_2}{\eta_2 - \eta_1} k_3 \end{cases} \quad (4.8)$$

where  $\eta_1 = \sqrt{n}$  and  $\eta_2 = 1$ .

$$\begin{cases} k_1 = \tan^{-1} \left[ \frac{2b\eta_1 z}{(\eta_1 z)^2 + x^2 - b^2} \right] + i\pi \\ k_2 = \tan^{-1} \left[ \frac{2b\eta_2 z}{(\eta_2 z)^2 + x^2 - b^2} \right] + i\pi \\ k_3 = \ln \left[ \frac{(b+x)^2 + (\eta_1 z)^2}{(b+x)^2 + (\eta_2 z)^2} \frac{(b-x)^2 + (\eta_2 z)^2}{(b-x)^2 + (\eta_1 z)^2} \right] \end{cases} \quad (4.9)$$

where  $i = 0$  unless  $k_1 < 0$  or  $k_2 < 0$ , in which case  $i = 1$ . If  $n$  is equal to one, the equations 4.8 become 'Boussinesq' stress distributions

$$\begin{cases} \Delta\sigma_z = \frac{q}{\pi} [\alpha + \sin\alpha \cos(\alpha + 2\beta)] \\ \Delta\sigma_x = \frac{q}{\pi} [\alpha - \sin\alpha \cos(\alpha + 2\beta)] \\ \Delta\tau_{xz} = \frac{q}{\pi} [\sin\alpha \sin(\alpha + 2\beta)] \end{cases} \quad (4.10)$$

where

$$\beta = \tan^{-1} [(x - b)/z], \quad \alpha = \tan^{-1} [(x + b)/z] - \beta$$

The mean stress  $\Delta p$  and maximum shear stress  $\Delta s$  can be expressed as

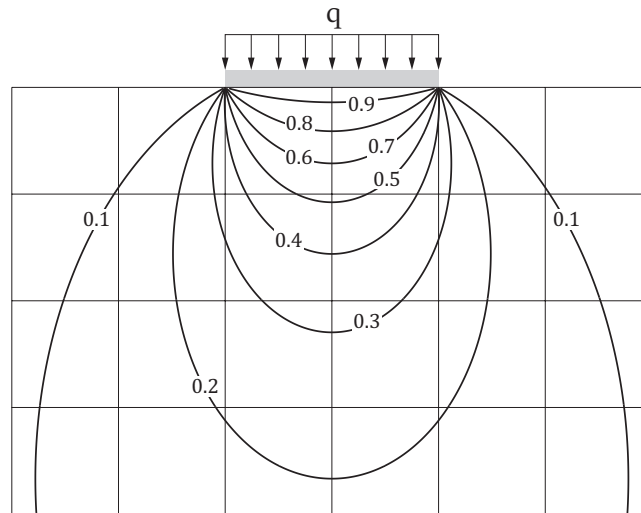
$$\begin{cases} \Delta p = \frac{(\Delta\sigma_1 + \Delta\sigma_3)}{2} \\ \Delta s = \frac{(\Delta\sigma_1 - \Delta\sigma_3)}{2} \end{cases} \quad (4.11)$$

where

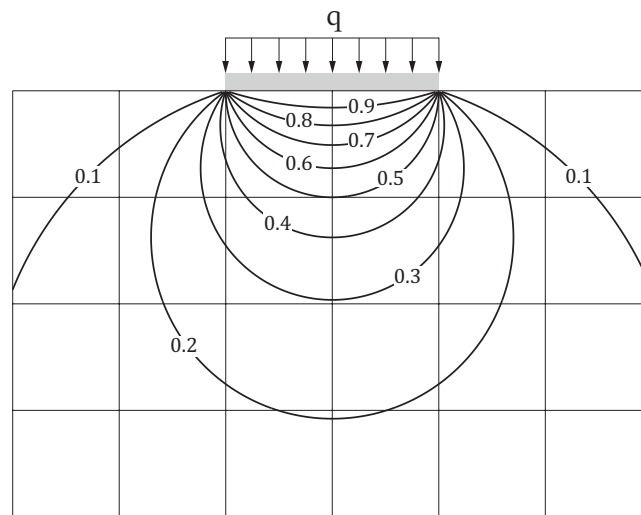
$$\begin{cases} \Delta\sigma_1 = \frac{1}{2}(\Delta\sigma_x + \Delta\sigma_z) + \sqrt{\frac{1}{4}(\Delta\sigma_x - \Delta\sigma_z)^2 + \Delta\tau_{xz}^2} \\ \Delta\sigma_3 = \frac{1}{2}(\Delta\sigma_x + \Delta\sigma_z) - \sqrt{\frac{1}{4}(\Delta\sigma_x - \Delta\sigma_z)^2 + \Delta\tau_{xz}^2} \end{cases} \quad (4.12)$$

In order to visualise increment of stress distribution, contours of increment  $\Delta p$  and  $\Delta s$  are demonstrated in Figure 4.6 and 4.7 respectively. In Figure 4.6, it can be seen that a smaller  $n$  brings a greater concentration of stress and a greater  $n$  brings a greater spreading of stress. In the Figure 4.7, if  $n$  is less than one, the maximum intensity locates at the loading center. In contrast, if  $n$  is higher than one, higher stresses diverge in a form of dipole starting from the both loading edges.

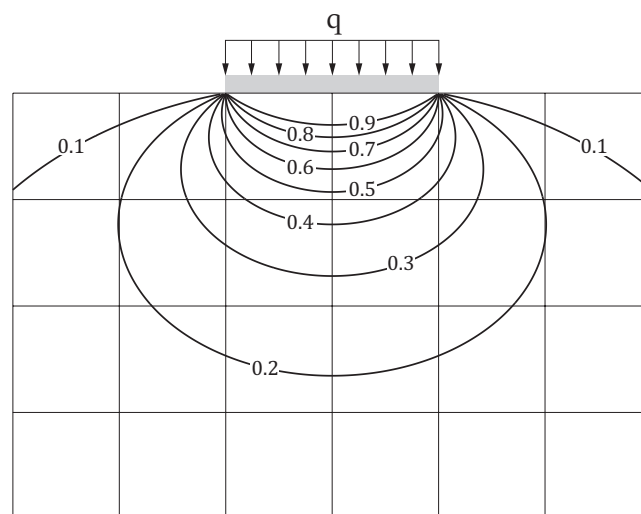
In these equations, it is assumed that self-weight of the soil-fill is zero. Thus the computations furnish the stress fields only due to a surface load. In order to obtain the total stresses including the soil self-weight one has to combine the stress fields due to a surface load with those produced by the weight of the supporting material.



(a)

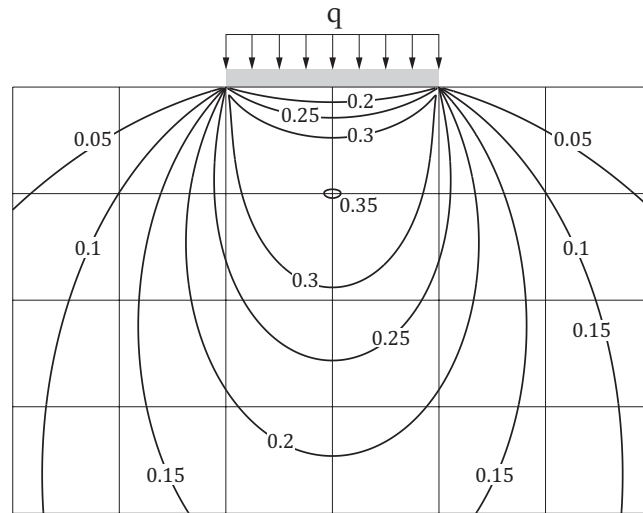


(b)

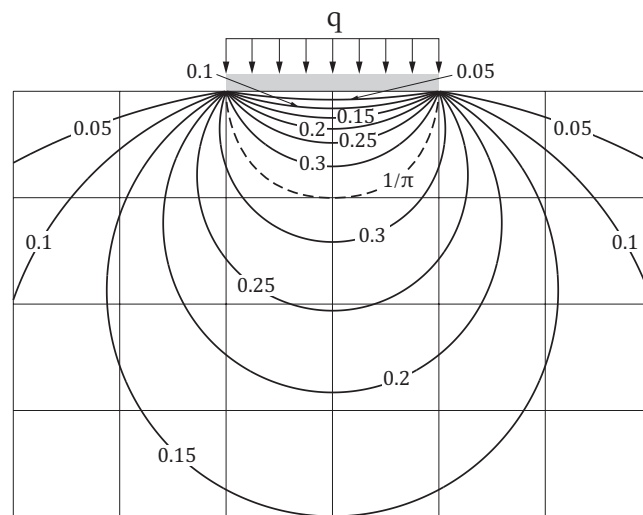


(c)

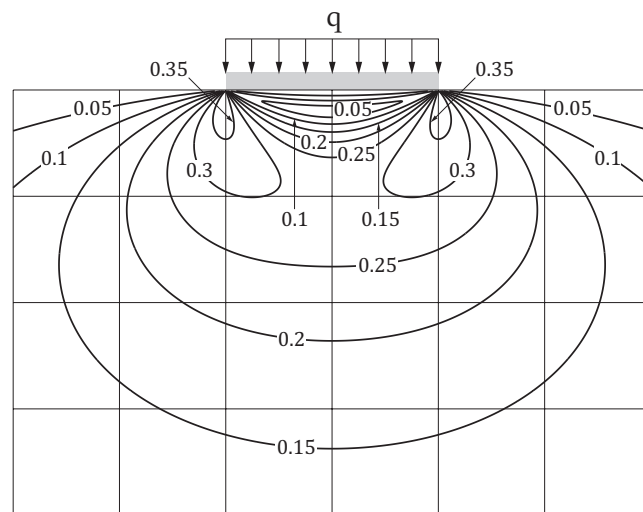
FIGURE 4.6: Contours of  $\Delta p/q$ : (a)  $n = 0.5$ ; (b)  $n = 1.0$ ; (c)  $n = 2.0$



(a)



(b)



(c)

FIGURE 4.7: Contours of  $\Delta s/q$ : (a)  $n = 0.5$ ; (b)  $n = 1.0$ ; (c)  $n = 2.0$

### 4.3.3 Stress Fields Due to Fill Self Weight

For stress fields from dead loads of soil-fill, the initial stress distribution due to the effect of soil self-weight is shown in Figure 4.4 (b). The principal stress orientations of the initial stress distribution are vertical and horizontal. The equations for the stress fields due to the weight of the soil-fill can be expressed as

$$\begin{cases} \sigma_v = \gamma z \\ \sigma_h = K(z) \sigma_v \end{cases} \quad (4.13)$$

where  $K(z)$  is the lateral earth pressure coefficient for the soil and may vary with depth  $z$ , and  $\gamma$  is the soil unit weight.

### 4.3.4 Combined Stress Fields

A combination of stress fields due to a strip load and the soil self-weight is shown in Figure 4.8. The total stresses of the combination were introduced by Dang et al. (2019), then they can be written as

$$\begin{cases} \sigma_z = \Delta\sigma_z + \sigma_v \\ \sigma_x = \Delta\sigma_x + \sigma_h \\ \tau_{xz} = \Delta\tau_{xz} \end{cases} \quad (4.14)$$

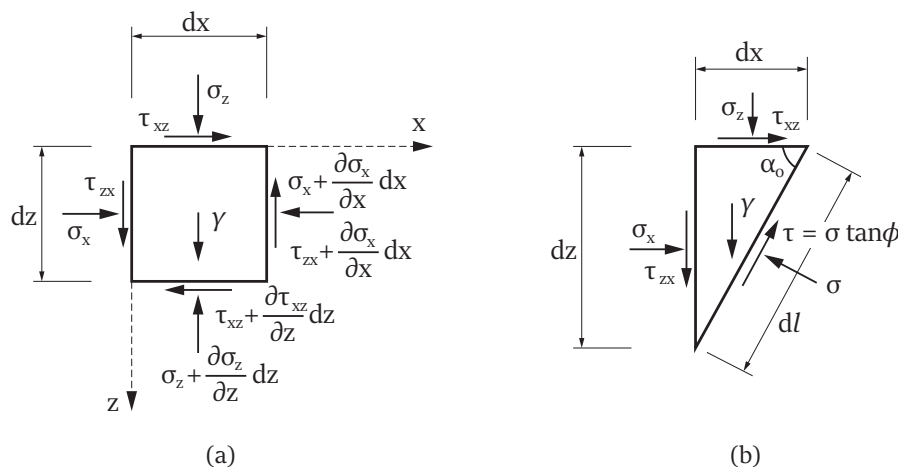


FIGURE 4.8: Diagrams illustrating equilibrium for soil stress fields

### 4.3.5 Yield Constraints

#### General Formulations

In accordance with the rules of lower bound limit analysis, a stress field due to a surcharge and a dead weight of soil, must nowhere violate the yield criteria. The Mohr-Coulomb yield condition can be expressed as

$$\frac{(\sigma_1 + \sigma_3)}{2} \sin \phi = \frac{(\sigma_1 - \sigma_3)}{2} - c \cos \phi \quad (4.15)$$

where

$$\begin{cases} \sigma_1 = \frac{1}{2}(\sigma_x + \sigma_z) + \sqrt{\frac{1}{4}(\sigma_x - \sigma_z)^2 + \tau_{xz}^2} \\ \sigma_3 = \frac{1}{2}(\sigma_x + \sigma_z) - \sqrt{\frac{1}{4}(\sigma_x - \sigma_z)^2 + \tau_{xz}^2} \end{cases} \quad (4.16)$$

For the masonry arch bridge problem, the yield conditions must be checked at any location within the soil body. Thus for any given depth, it is necessarily to determine the values of  $K(z)$ . The range of  $K(z)$  is limited by the Rankine (1857) active and passive lateral earth pressure coefficients as follows

$$K_{\infty, \min} = K_a \leq K(z) \leq K_p = K_{\infty, \max} \quad (4.17)$$

where

$$\begin{cases} K_a = \tan^2 \left( \frac{\pi}{4} - \frac{\phi}{2} \right) \\ K_p = \tan^2 \left( \frac{\pi}{4} + \frac{\phi}{2} \right) \end{cases} \quad (4.18)$$

where  $\phi$  is the internal frictional angle of soil-fill.

For cohesion soil,  $c$  is equal to zero, then the mobilised friction  $\sin \phi_m$  can be derived from equation 4.15 and obtained as

$$\sin \phi_m = \frac{(\sigma_1 - \sigma_3)/2}{(\sigma_1 + \sigma_3)/2} = \frac{\sqrt{\frac{1}{4}(\sigma_x - \sigma_z)^2 + \tau_{xz}^2}}{\frac{1}{2}(\sigma_x + \sigma_z)} \quad (4.19)$$

When  $K(z)$  is equal to  $K_a$  at any given position, a combined stress field does not lead to yield violation as illustrated using Mohr's circles as shown in Figure 4.9(a).

For cohesive soil,  $\phi$  is equal to zero, then the equation 4.15 becomes

$$c = \frac{(\sigma_1 - \sigma_3)}{2} = \sqrt{\frac{1}{4}(\sigma_x - \sigma_z)^2 + \tau_{xz}^2} \quad (4.20)$$

In this case  $K(z)$  is equal to one, a combined stress field does not lead to yield violation as illustrated using Mohr's circles as shown in Figure 4.9(b).

For frictional-cohesive soil-fill, the material yield criteria can be simplified as the equivalent cohesionless material yield condition of Mohr-Coulomb as shown in Figure 4.9(c). The equivalent frictional angle  $\phi_e$  can be defined as (Ni et al. 2018)

$$\phi_e = \tan^{-1} \left( \tan \phi + \frac{c}{\gamma z} \right) \quad (4.21)$$

Substitute equation 4.21 into equation 4.19 and replace  $\phi$  by  $\phi_e$ , then the equation 4.19 can be expressed as

$$\sin \phi_e = \sin \left\{ \tan^{-1} \left[ \tan \left( \sin^{-1} \left( \frac{\sqrt{\frac{1}{4}(\sigma_x - \sigma_z)^2 + \tau_{xz}^2}}{\frac{1}{2}(\sigma_x + \sigma_z)}} \right) \right) + \frac{c}{\gamma z} \right] \right\} \quad (4.22)$$

In the frictional-cohesive soil-fill, when  $K(z)$  is equal to  $K_a$  obtained using the value of  $\phi_e$ , a combined stress field does not lead to yield violation as illustrated in Figure 4.9(c).

### Simple Example of Footing

The use of stress fields can be illustrated by considering a strip footing. The strip footing with length  $B$  of 0.5 m, positioned on the surface of soil with unit weight  $\gamma$  of 20 kN/m<sup>3</sup>. A strip load of 100 kN/m positioned on the cohesionless soil surface (Figure 4.10(a)) and the frictional-cohesive soil surface (Figure 4.10(b)), respectively. To visualize the flow of required frictional strength in supporting soil material, it is necessary to plot contours of the greatest mobilized frictional angle.

Figure 4.11 shows the contours of mobilised frictional angle of cohesionless and frictional-cohesive soil respectively. Stress fields combine the 'Boussinesq' stress fields (e.g. anisotropic ratio  $n$  is equal to one) and earth pressures due to the self weight of soil. In this case the value of  $K(z)$  is assumed as one at any depth. In Figure 4.11(a), it can be seen that the weakest zone is at the surface of the soil on both sides of the loaded strip footing. In Figure 4.11(b), the surface includes cohesion, so

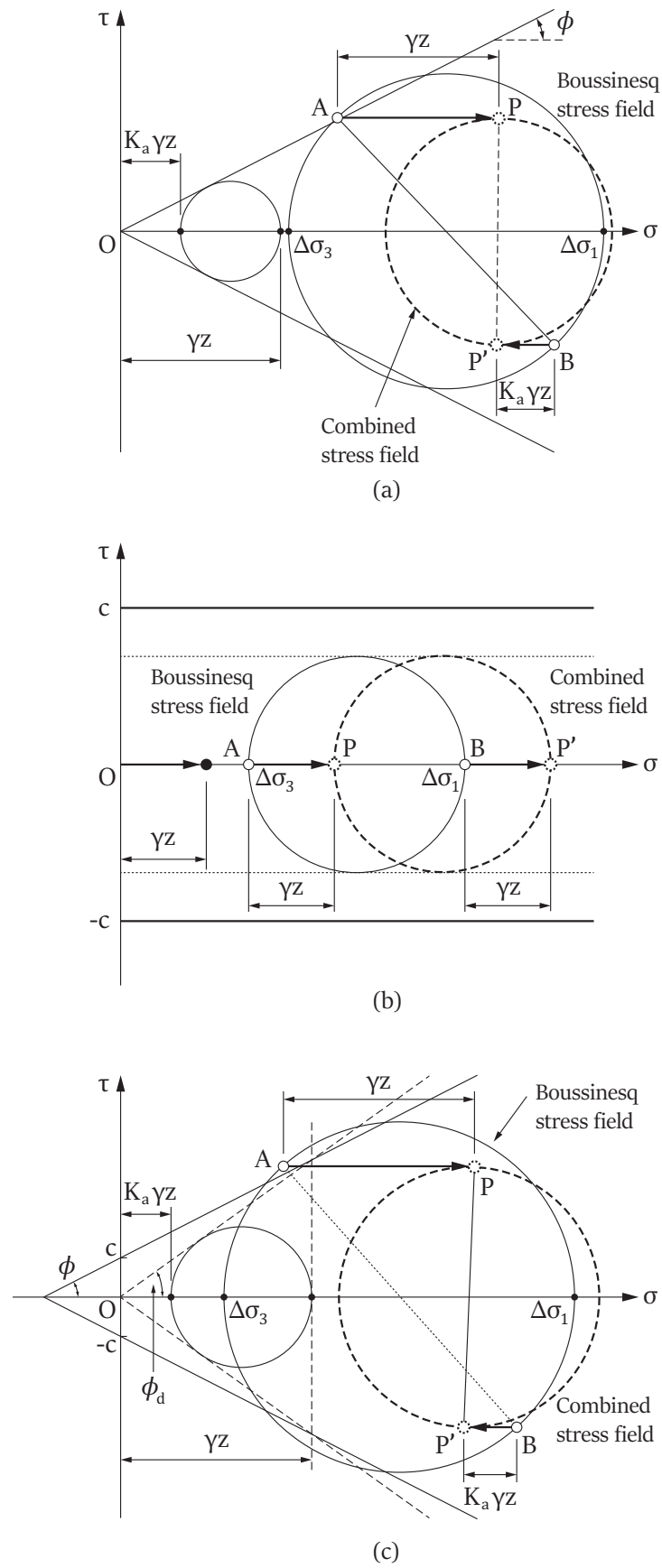


FIGURE 4.9: Mohr stress diagrams of (a) cohesionless and (b) cohesion and (c) frictional-cohesive soil

that the surface zone does not violate yield condition when the cohesion provides enough shear strength.

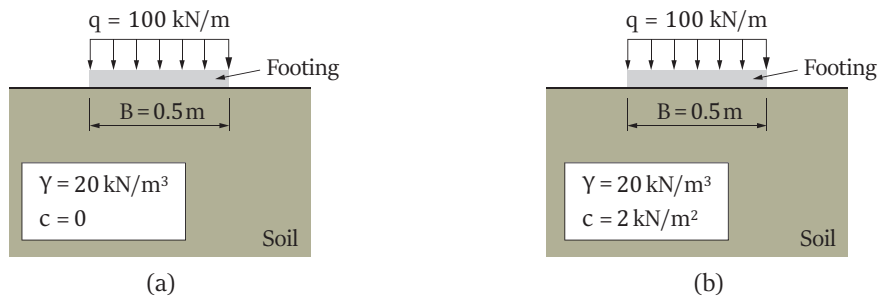


FIGURE 4.10: Example of footing on the surface of (a) cohesionless and (b) cohesive soil

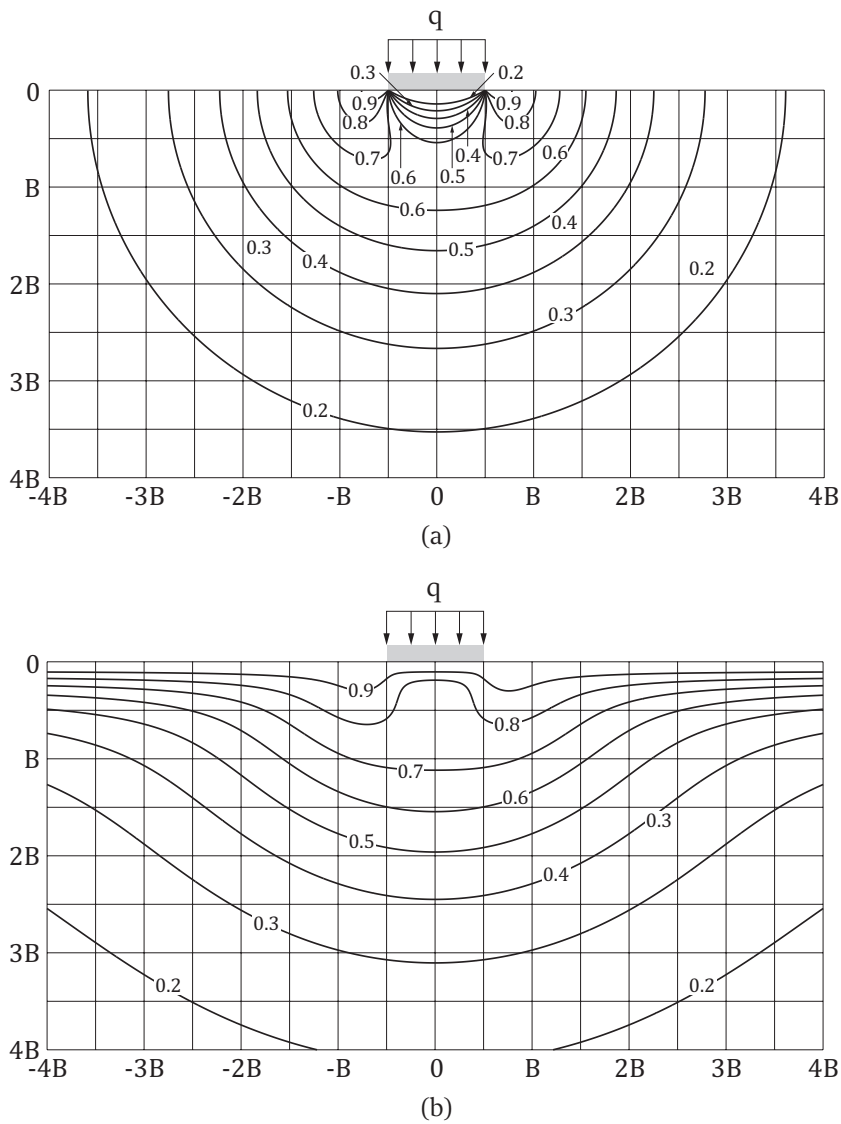


FIGURE 4.11: Contours of mobilised friction  $\sin \phi_m$  with  $n = 1.0$  and  $q/\gamma B = 10, K = 1$ : (a)  $c/\gamma B = 0$ ; (b)  $c/\gamma B = 0.2$

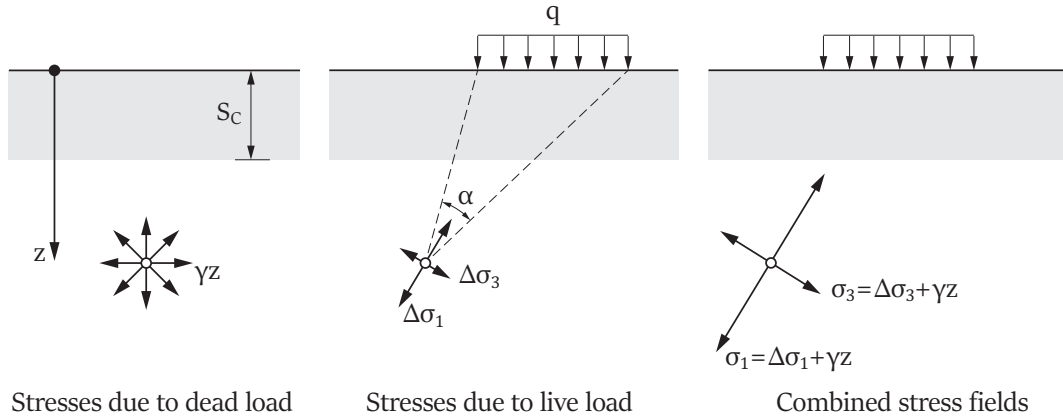


FIGURE 4.12: Superposition of initial and induced stresses in ideal soil (original gravity stresses assumed spherical) (after Bolton 1979)

In order to generate sufficient friction to make such shear stresses viable, it is necessary to provide a cohesion  $c$  to avoid yield for the layer and this provides the sufficient strength and depth of the 'cemented' layer  $S_c$ . Figure 4.12 shows an ideal soil in which the initial stress distribution has been assumed to be spherical and to increase linearly with depth. Superposition between initial and induced stresses can obtain the total principal stresses as follows

$$\begin{cases} \sigma_1 = \frac{q}{\pi} (\alpha - \sin \alpha) + \gamma z \\ \sigma_3 = \frac{q}{\pi} (\alpha - \sin \alpha) + \gamma z \end{cases} \quad (4.23)$$

Then the greatest mobilised friction can be derived from the total principal stresses mobilised at any point, and that is

$$\sin \phi_e = \frac{(\sigma_1 - \sigma_3)/2}{(\sigma_1 + \sigma_3)/2} = \frac{\frac{q}{\pi} \sin \alpha}{\gamma z + \frac{q}{\pi} \alpha} \quad (4.24)$$

It is necessary to find the largest mobilised friction in order to check that the yield condition has not been yielded. Thus the mobilised friction can be achieved by using calculus such as  $d(\sin \phi_m)/d\alpha = 0$ . In that  $\alpha$  can take any value between zero and  $\pi$ , and by differentiation using  $z = S_c$

$$\frac{d(\sin \phi_e)}{d\alpha} = \frac{\left(\gamma S_c + \frac{q}{\pi} \alpha\right) \left(\frac{q}{\pi} \cos \alpha\right) - \left(\frac{q}{\pi} \sin \alpha\right) \frac{q}{\pi}}{\left(\frac{q}{\pi} \cos \alpha\right)^2} \quad (4.25)$$

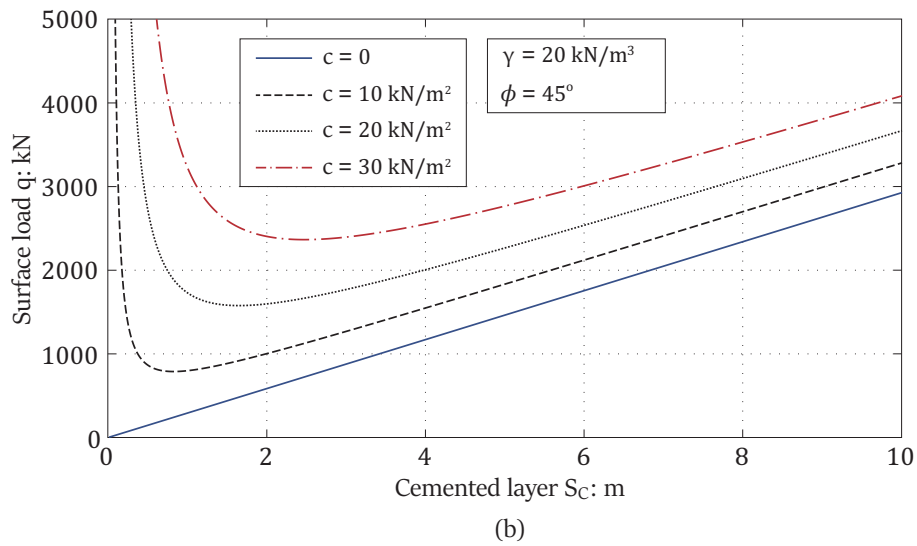
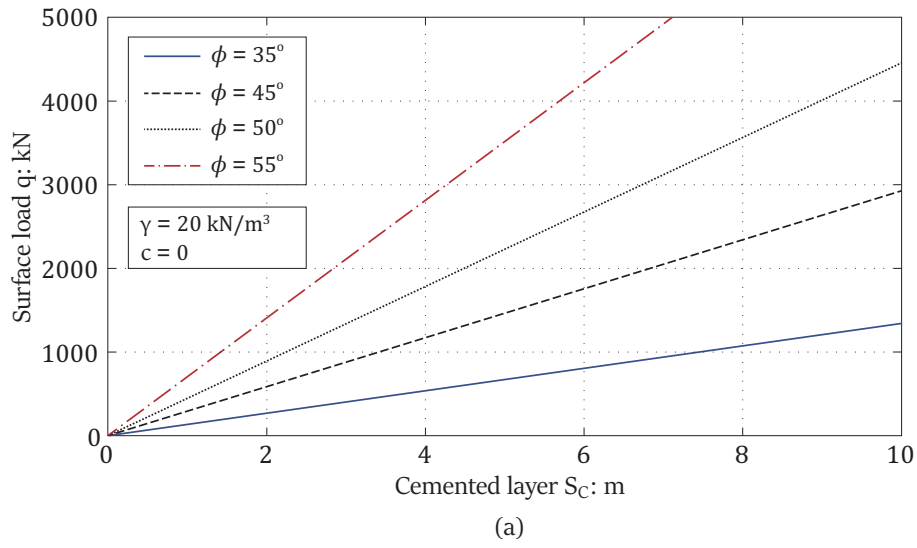


FIGURE 4.13: Surface load at cemented layer  $S_C$ : (a) influence of friction angle  $\phi$  and (b) cohesion  $c$

When this equation is equal to zero, then

$$\alpha = \tan \alpha - \frac{\pi \gamma S_c}{q} \quad (4.26)$$

Substitute this equation into the denominator of equation 4.24, and using  $z = S_c$ , then the equation becomes

$$\sin \phi_e = \frac{\frac{q}{\pi} \sin \alpha}{\gamma S_c + \frac{q}{\pi} \tan \alpha - \gamma S_c} = \cos \alpha \quad (4.27)$$

Thus the critical angle of  $\alpha$  can be obtained as

$$\alpha = \frac{\pi}{2} - \phi_e \quad (4.28)$$

Equation 4.26 can then be written as

$$\frac{\pi}{2} - \phi_e = \cot \phi_e - \frac{\pi \gamma S_c}{q} \quad (4.29)$$

Substituting equation 4.21 into equation 4.29, then equation can be rewritten as

$$q = \frac{\pi \gamma S_c}{\tan^{-1} \left( \tan \phi + \frac{c}{\gamma S_c} \right) + \cot \left[ \tan^{-1} \left( \tan \phi + \frac{c}{\gamma S_c} \right) \right] - \frac{\pi}{2}} \quad (4.30)$$

Figure 4.13(a) shows the greater friction angle  $\phi$  brings the increasing of the allowable surface load. This figure also indicates that the friction of cohesionless soil at the surface cannot provide shear strength to avoid yield. However, if add cohesion strength in the soil, the surface load can be supported by sufficient shear strength to avoid yield. Figure 4.13(b) also shows the greater cohesion  $c$  brings the increasing of the allowable surface load.

In order to automatically determine the sufficient lateral earth pressure coefficient  $K(z)$  at depths to avoid yield, it is necessary to derive a series of equations to check yield for combined stress fields.

### Yield Check for Combined Stress Fields

In order to automatically constraint stress field, substituting equation 4.14 into 4.18, expression of combined stress fields can be re-written as

$$\begin{cases} \sigma_z = \Delta \sigma_z + \gamma z \\ \sigma_x = \Delta \sigma_x + K(z) \gamma z \\ \tau_{xz} = \Delta \tau_{xz} \end{cases} \quad (4.31)$$

To simplify an expression of  $K(z)$ , two parameters are defined as

$$\begin{cases} D_1 = \Delta \sigma_x + \Delta \sigma_z \\ D_2 = \Delta \sigma_x - \Delta \sigma_z \end{cases} \quad (4.32)$$

Substitute equation 4.14 and 4.32 into 4.15, then the required lateral earth pressure coefficient (Appendix D) can be derived as

$$K(z) = \frac{-\chi \pm \sqrt{\chi^2 - 4\psi\kappa}}{2\psi} \quad (4.33)$$

where

$$\begin{cases} \psi = \gamma^2 z^2 (\sin^2 \phi - 1) \\ \chi = 2\gamma^2 z^2 (\sin^2 \phi + 1) + 2\gamma z (D_1 \sin^2 \phi - D_2) \\ \kappa = \gamma^2 z^2 (\sin^2 \phi - 1) + 2\gamma z (D_1 \sin^2 \phi + D_2) + D_1 \sin^2 \phi - D_2^2 - 4\Delta\tau_{xz}^2 \end{cases} \quad (4.34)$$

The equation gives two solutions, the higher of which gives an active lateral pressure coefficient, the lower of which gives a passive lateral pressure coefficient. Figure 4.14 shows the required active lateral earth pressure coefficients computed by applied load and soil frictional strength.

### Cemented Layer

When equation 4.25 has no solution, it means that no suitable value of  $K$  can avoid yield. Thus, it is necessary to provide a cohesion  $c$  to avoid yield for the layer and this provides the criterion for the strength and depth of the cemented layer  $S_C$ . The base of the cemented layer can be found as

$$\chi^2 - 4\psi\kappa = 0 \quad (4.35)$$

Substitute equation 4.34 and 4.35 into 4.33, then the critical  $K(S_C)$  can be derived as follows

$$K(S_C) = \tan^2 \phi \left( 1 + \frac{D_1}{\gamma S_C} \right) + \sec^2 \phi \left( 1 - \frac{D_2}{\gamma S_C} \right) \quad (4.36)$$

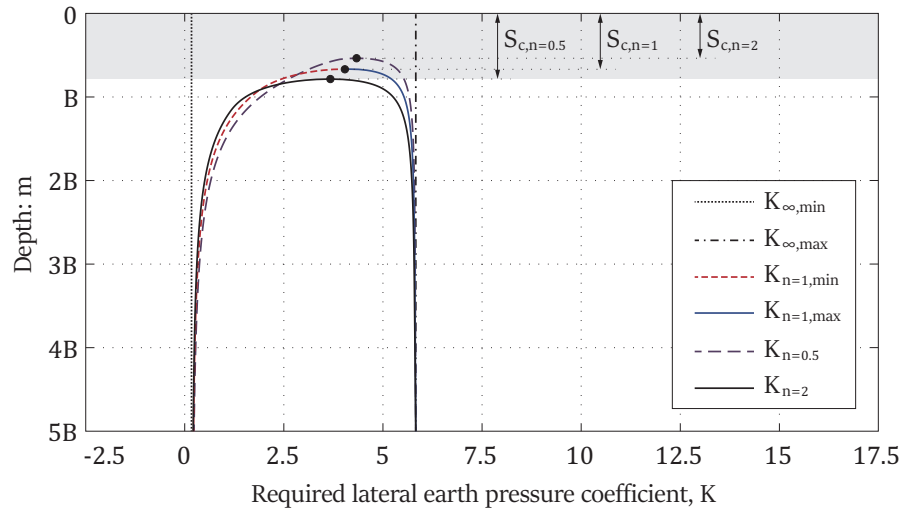
Substituting equation 4.36 into 4.31 and then into equation 4.21 gives the required cohesion  $c_C$  as

$$c_C = (\tan \phi'_e - \tan \phi) \cdot \gamma S_C \quad (4.37)$$

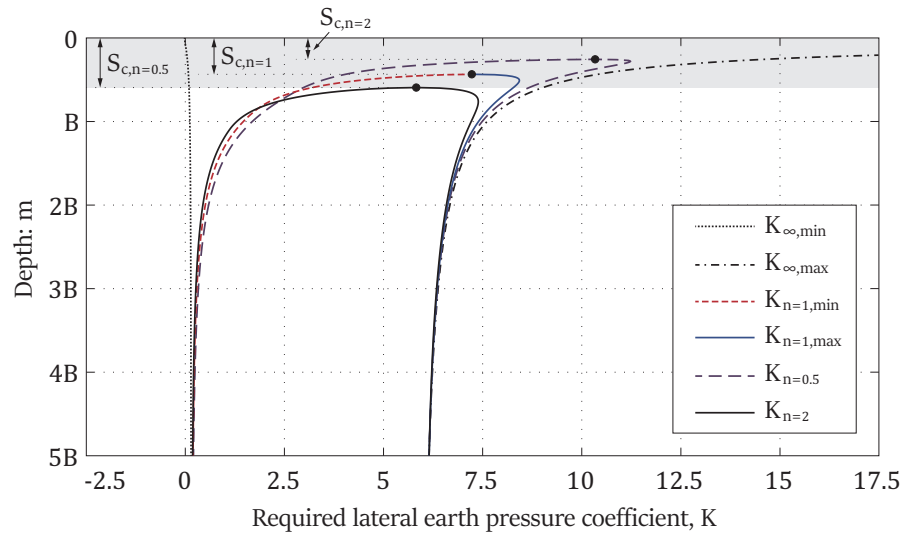
where

$$\tan \phi'_e = \tan \left\{ \sin^{-1} \left[ \frac{\sqrt{\frac{1}{4} [D_2 + \gamma S_C (K(S_C) - 1)]^2 + \Delta\tau_{xz}^2}}{\frac{1}{2} [D_1 + \gamma S_C (K(S_C) + 1)]}} \right] \right\} \quad (4.38)$$

Figure 4.14 shows the required depth of the cemented layer  $S_C$ .



(a)



(b)

FIGURE 4.14: Required lateral earth pressure coefficients with  $q/\gamma B = 10$  at depths: (a)  $c/\gamma B = 0$ ; (b)  $c/\gamma B = 0.2$

### 4.3.6 Determination of Lower Bound Stress Fields

Pragmatically it is necessary to divide the soil body into horizontal layers of finite thickness and determine a sufficient value of  $K_{min}$  or  $K_{max}$  for each layer in the active or passive zones that maintains a lower bound. As illustrated in Figure 4.15(c), 4.16(c) and 4.17(c), it can be seen that for  $K_{min}$  the critical (highest) value will either be where the arch intersects the layer (or on the load centreline if there is no intersection) or it will be at  $x = \pm\infty$ . For  $K_{max}$  the critical (lowest) value is at an intermediate minimum point. Due to the complexity of the Moroto equations it is necessary to identify this point using a standard rapid 1D min/max search algorithm or at the arch/layer intersection. Figure 4.18 and 4.19 show the contours of mobilised friction with different  $n$ .

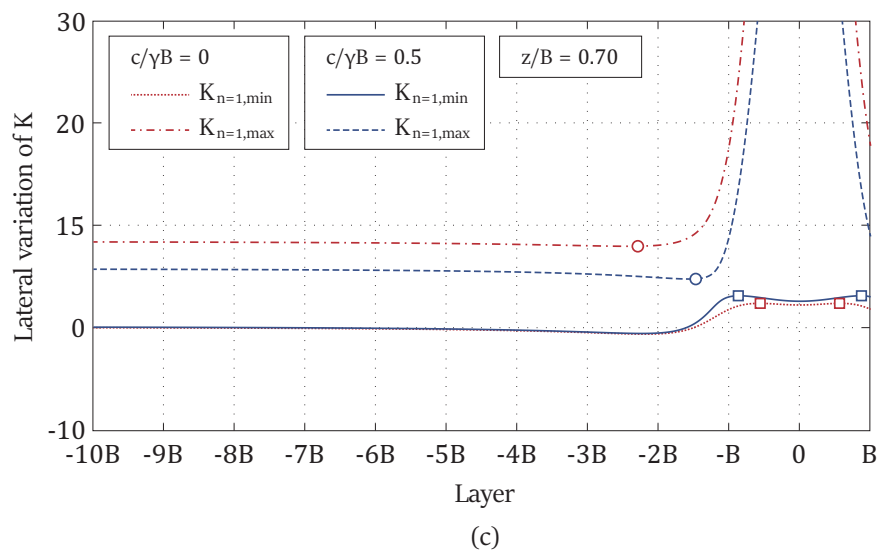
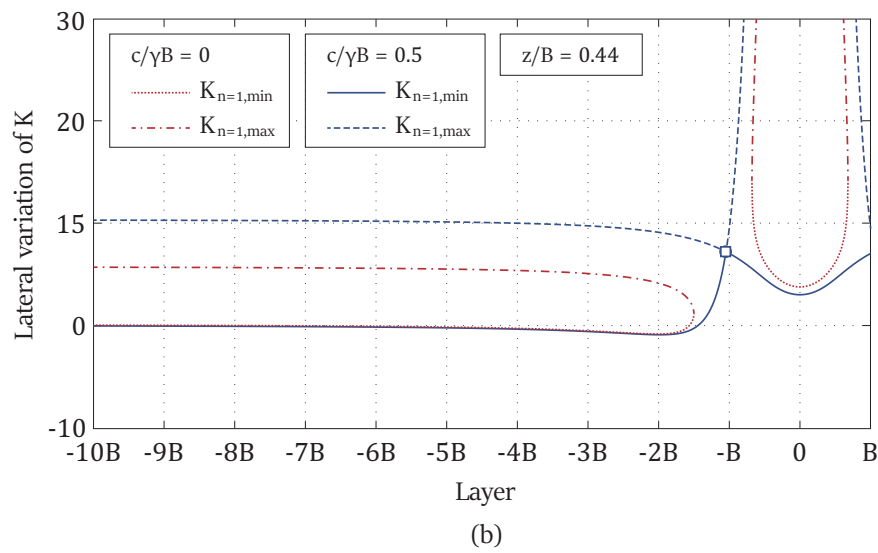
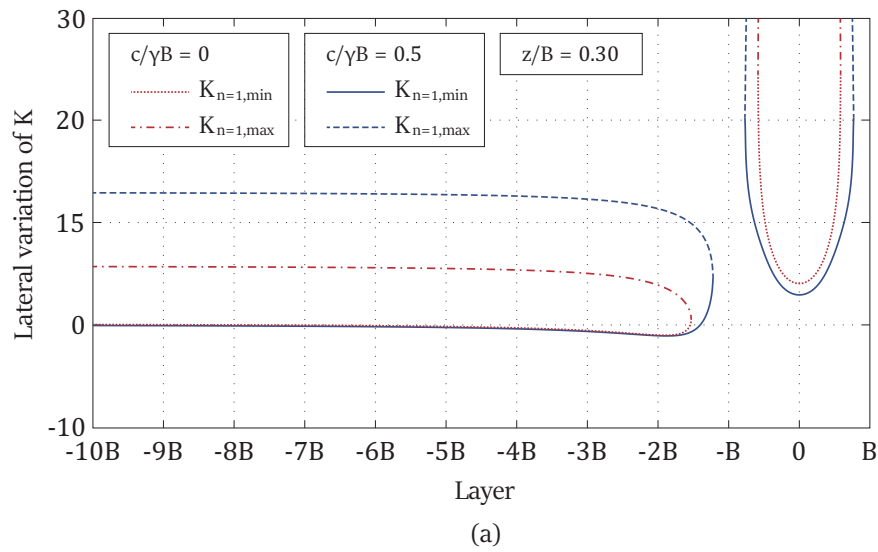


FIGURE 4.15: Lateral variation of  $K_{min}$  and  $K_{max}$  for  $n = 1.0$  and  $q/\gamma B = 10$  at depths: (a)  $z/B = 0.30$ ; (b)  $z/B = 0.44$ ; (c)  $z/B = 0.70$

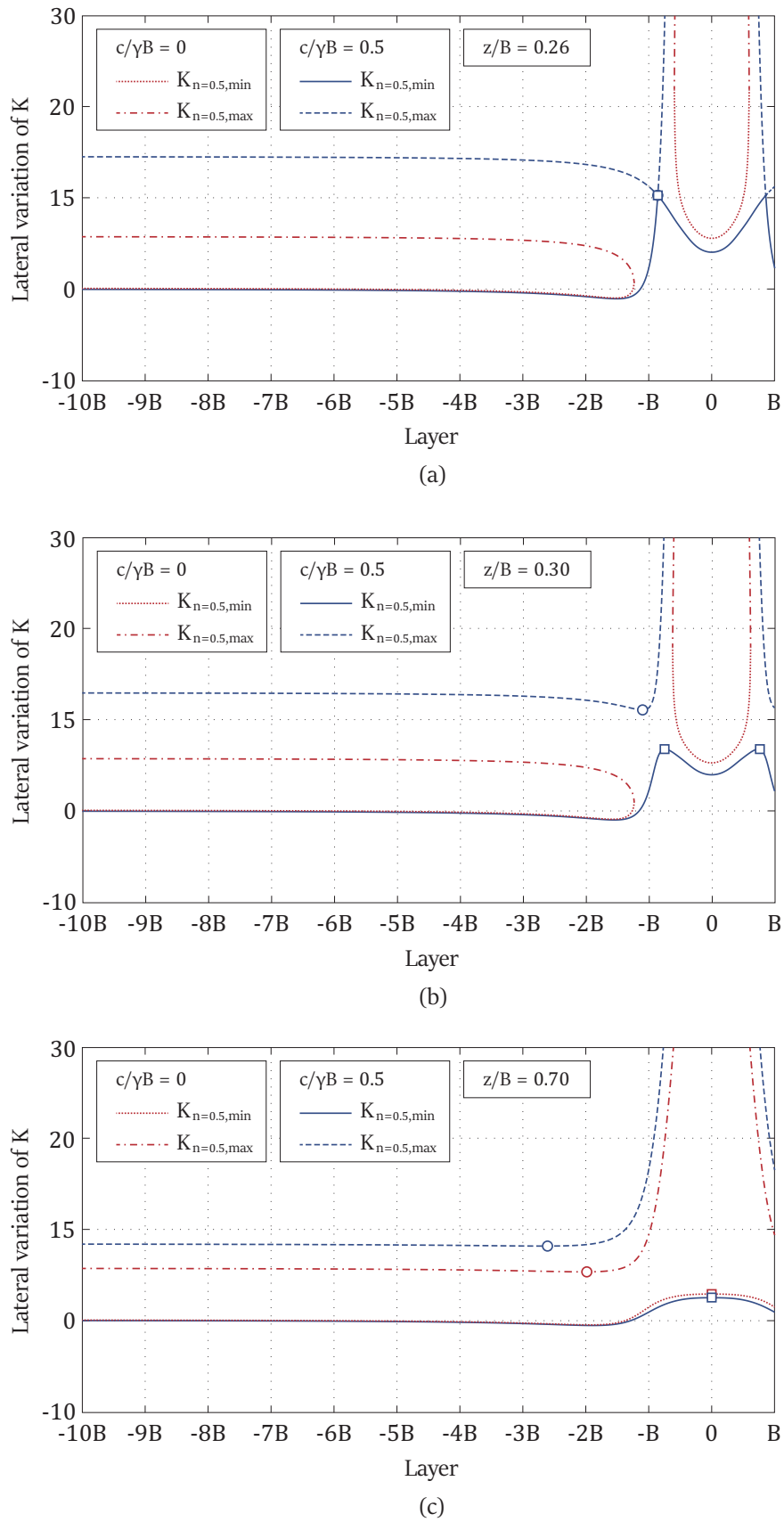


FIGURE 4.16: Lateral variation of  $K_{min}$  and  $K_{max}$  for  $n = 0.5$  and  $q/\gamma B = 10$  at depths: (a)  $z/B = 0.26$ ; (b)  $z/B = 0.30$ ; (c)  $z/B = 0.70$

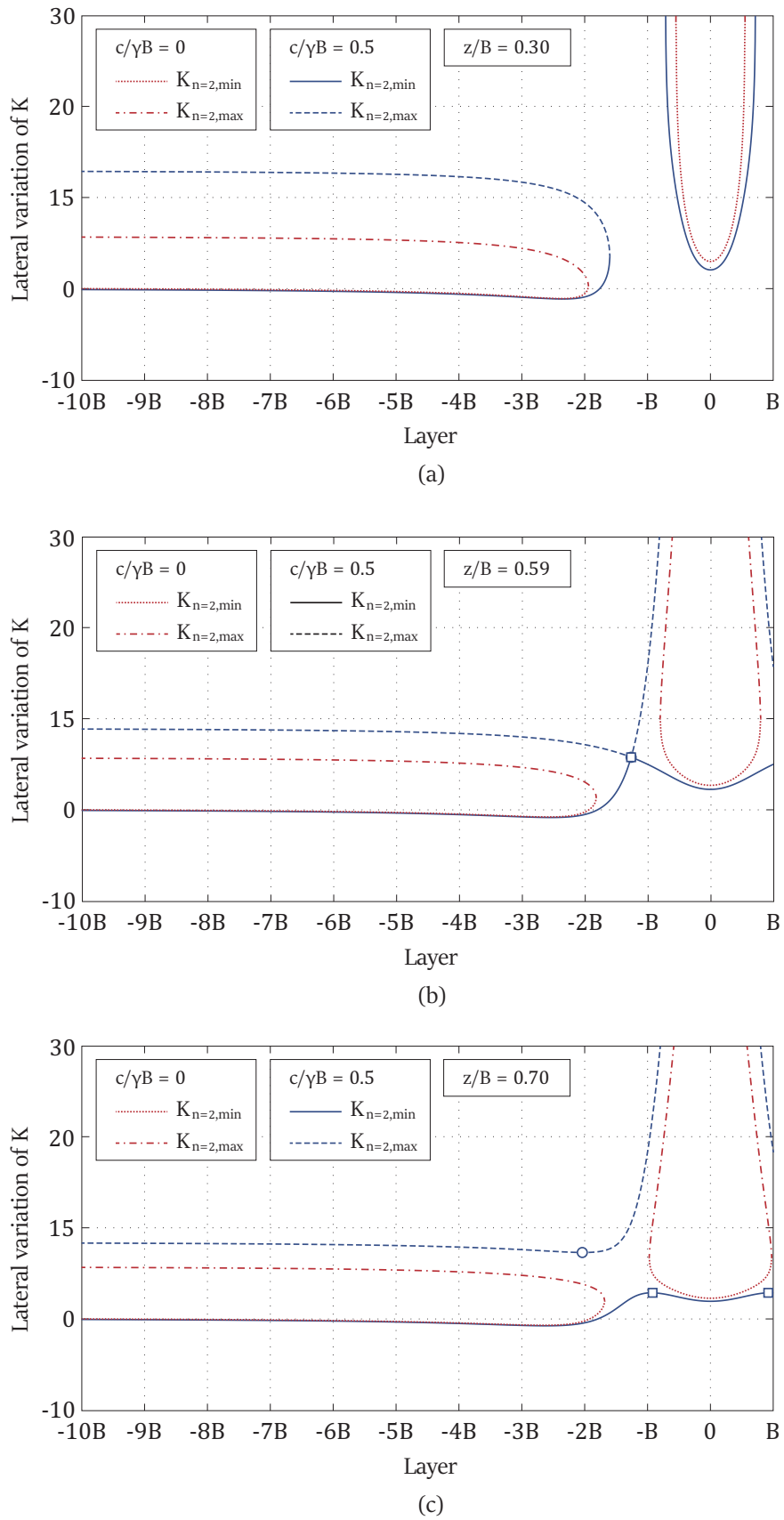


FIGURE 4.17: Lateral variation of  $K_{min}$  and  $K_{max}$  for  $n = 2.0$  and  $q/\gamma B = 10$  at depths: (a)  $z/B = 0.30$ ; (b)  $z/B = 0.59$ ; (c)  $z/B = 0.70$

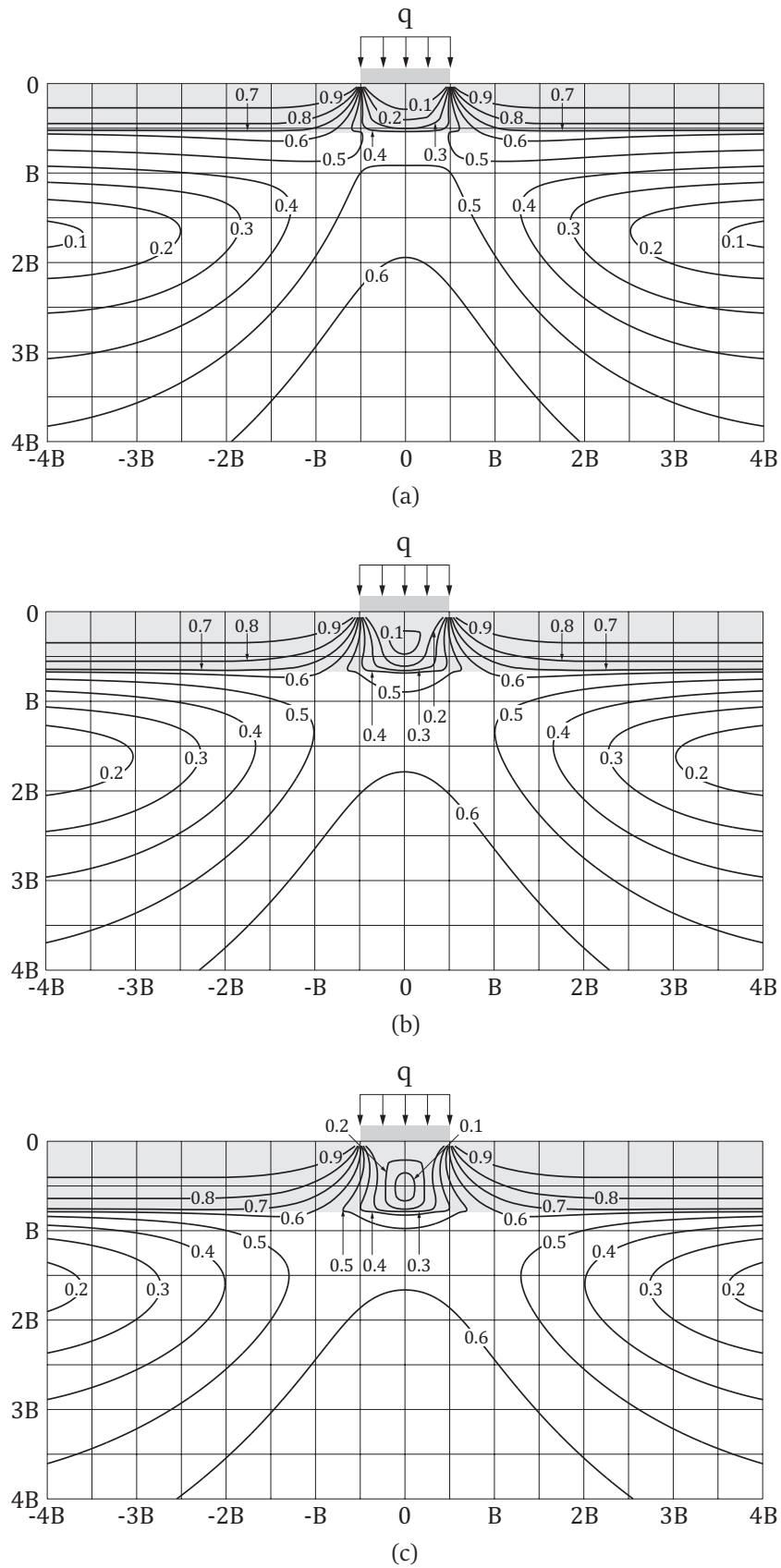


FIGURE 4.18: Contours of mobilised friction  $\sin \phi_m$  with  $q/\gamma B = 10$  and  $c/\gamma B = 0$ : (a)  $n = 0.5$ ; (b)  $n = 1.0$ ; (c)  $n = 2.0$

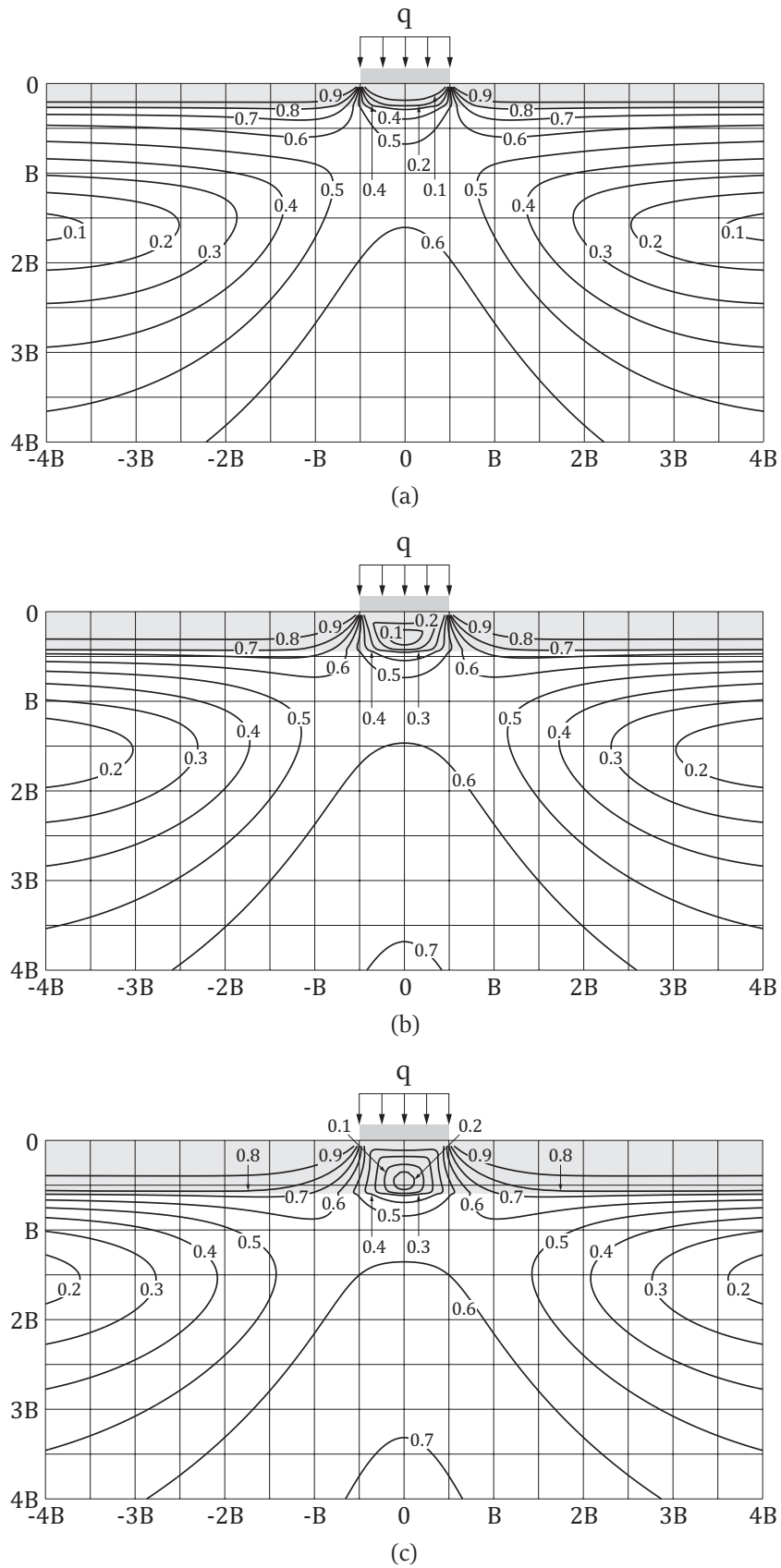


FIGURE 4.19: Contours of mobilised friction  $\sin \phi_e$  with  $q/\gamma B = 10$  and  $c/\gamma B = 0.2$ : (a)  $n = 0.5$ ; (b)  $n = 1.0$ ; (c)  $n = 2.0$

### 4.3.7 Iterative Procedure

Combined stress field and its yield constraint were introduced in previous sections. Utilizing combined stress field to rigid-block analysis and maximizing the load factor  $\lambda$  can obtain the collapse load factor  $\lambda_c$  which is a true lower bound solution. In order to clearly explain the use of the proposed stress field, we need to make a flow chart interpret the application of stress field to numerical limit analysis procedure.

In the iterative procedure, initially an anisotropic ratio  $n$  is selected in input data. The choice of  $n$  value has a significant effect on the computed arch collapse load magnitude, because the soil stress spreading capacity is evaluated by the single parameter  $n$  (Figure 4.20). However, it is difficult to know the real Young's modulus at limit state. Main flow chart of the programme is shown in Figure 4.21. The presented flow chart specifies a function that will give the optimal lower bound load  $q$  for any given value of  $n$  using the current method  $q = f(n)$ . If desired a better solution can be found more rigorously using numerical optimization and a search for the maximum value of  $f(n)$ . This can be done for example using the MATLAB function `fminbnd` (e.g.  $n_{opt} = \text{fminbnd}(f, n_{low}, n_{high})$ , where  $n_{low}$  and  $n_{high}$  might be selected as e.g. 0.1 and 10.0).

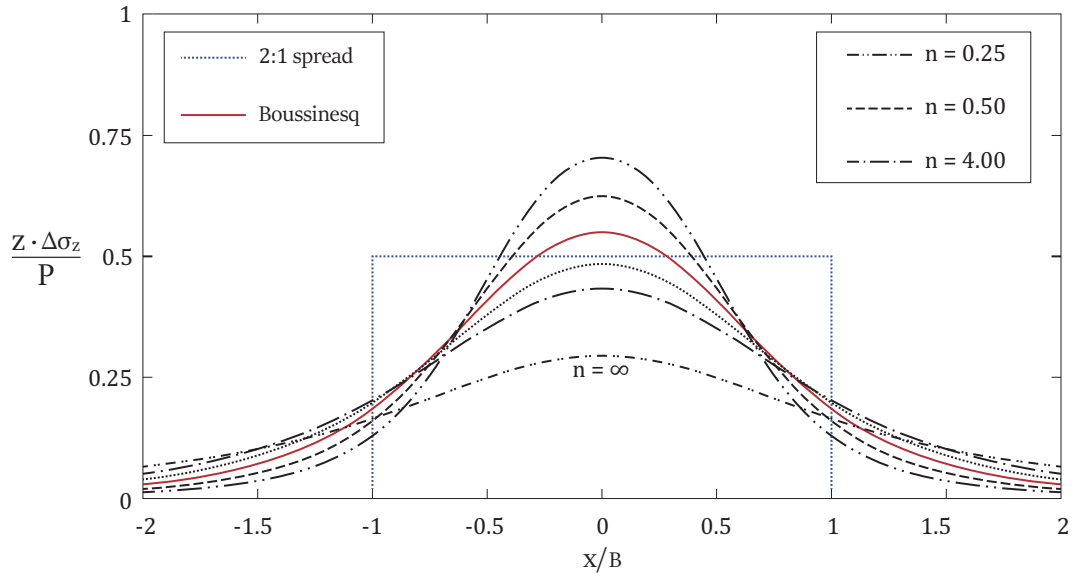


FIGURE 4.20: Vertical stress distribution at depth B

After determination of  $n$ , apply active lateral earth pressure coefficient  $K_0$  ( $K_0$  assumed as one) and passive coefficient  $K_p$  into rigid-block analysis and utilizing linear programming (LP) optimization to find a load  $q_0$ . Input  $q_0$  into equation 4.25 then  $K_{i=1}(z)$  can be obtained. Use  $K_{i=1}(z)$  to calculate a new load  $q_{i=1}$ , then compute the difference between  $q_{i=1}$  and  $q_0$  (e.g.  $|\Delta q_{initial} - \Delta q_{New}| < tol$ , where  $tol$  is the value of tolerance). If the difference of them is larger than an effective value of tolerance, then the computation programme will implement a loop to obtain a better lower bound solution.

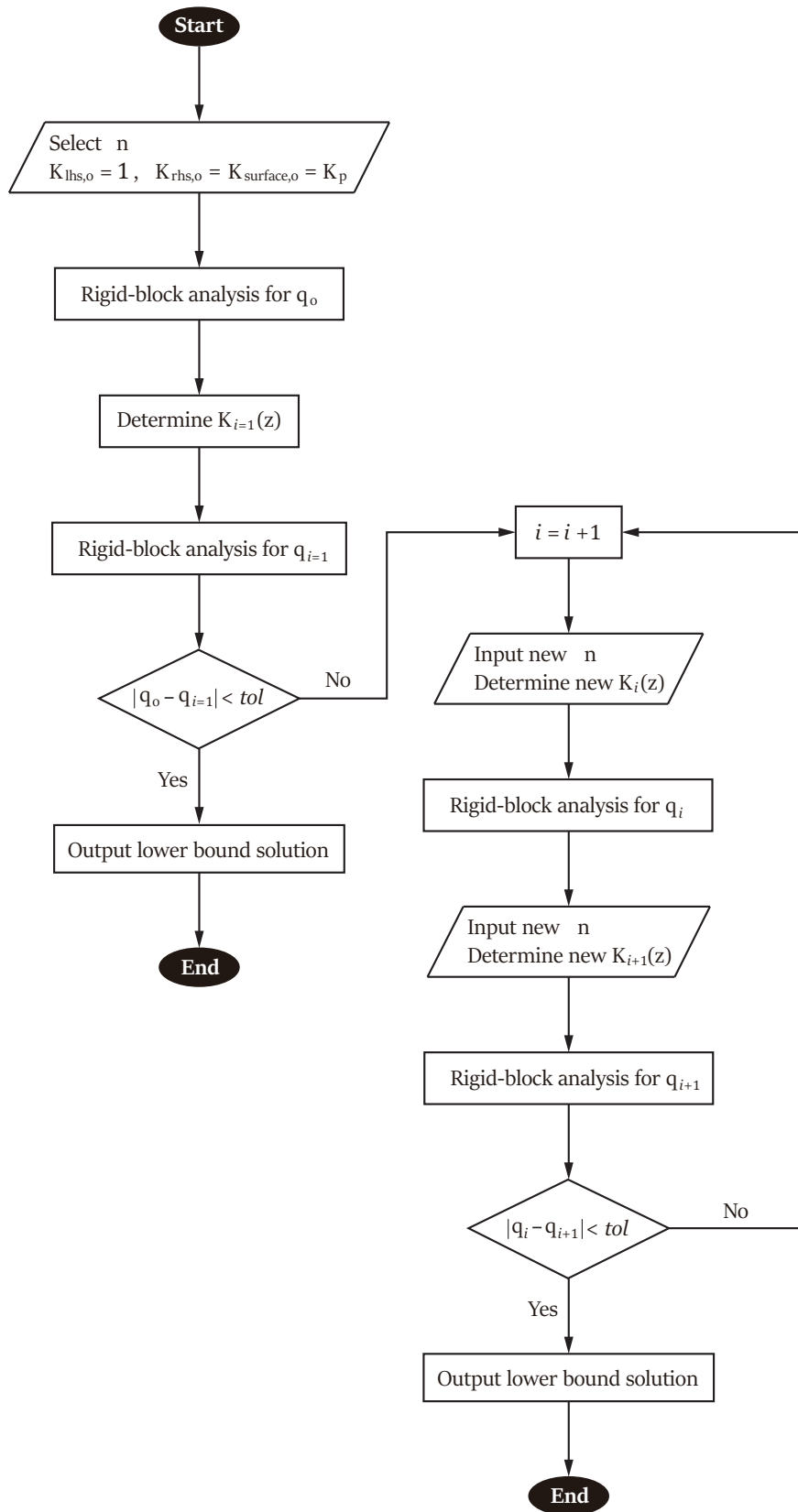


FIGURE 4.21: Iterative flow chart

## 4.4 Application to Case Studies

The use of lower bound stress fields method can be illustrated by considering literature bridges (e.g. Bolton, Salford and Bridgemill arch bridge). The main material properties and geometry are shown in section 2.4 of literature. Bridge upper-bound solutions obtained using the discontinuity layout optimization (DLO) limit analysis technique (Smith and Gilbert 2007) are introduced in section 2.4 and 3.4. The results obtained using the proposed lower-bound calculations can be compared with the upper-bound solutions.

In order to ensure good converge of the potential discontinuities in DLO model, the number of nodes used in DLO-normal was 5000. For the CPU times, it is necessary to compare different methods for a single load case. Figure 4.22 indicates that the lower-bound stress fields method (4.9 s) is faster than the current version of LimitState:GEO (330 s) and fast running DLO (25.8 s) CPU times.

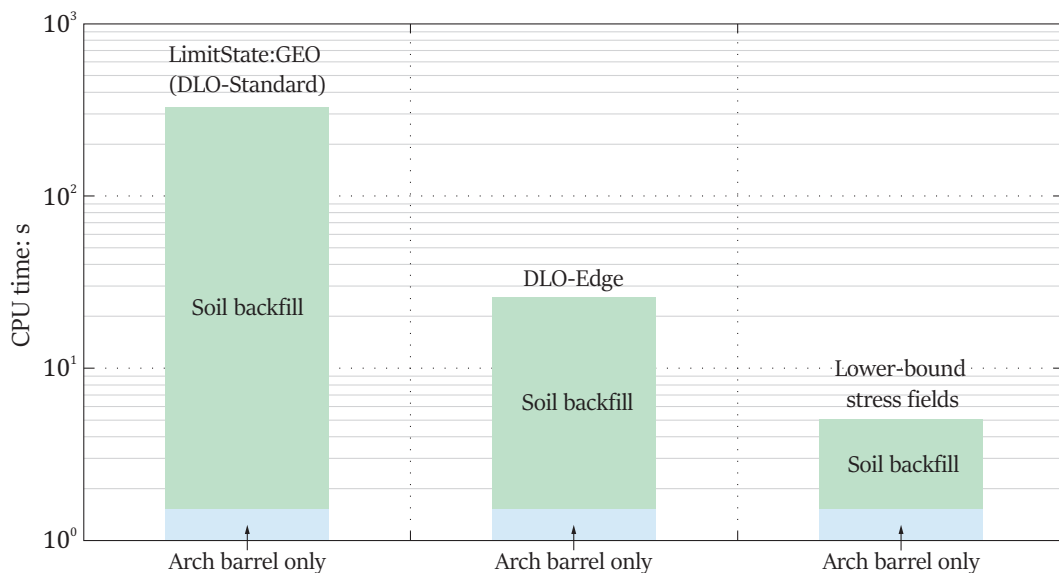


FIGURE 4.22: CPU time comparison of DLO-normal, DLO-fast and lower-bound stress fields

In order to investigate some of key parameters utilised in the analysis of masonry arch bridge, a parametric study was carried out in the application of lower- and upper-bound method to literature bridges. There are three parameters (e.g. cohesion  $c$ , frictional angle  $\phi$  and passive mobilisation factor) was varied in turn while others were kept fixed. The default values of three parameters for each bridge are listed in section 2.4 of literature. The results are shown in Figure 4.23 ~ 4.25. The bridge load-carrying capacity is seen to relatively sensitive to the soil strength, particularly for 'passive side' mobilisation factor.

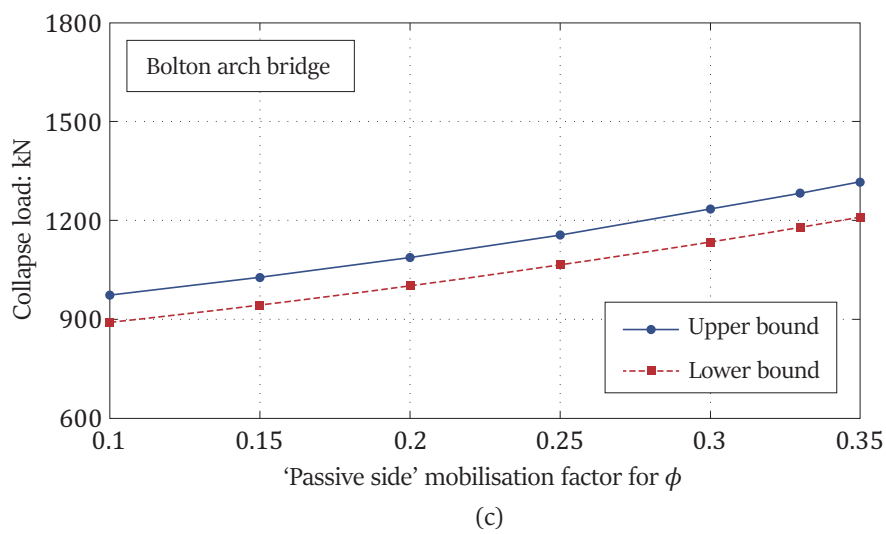
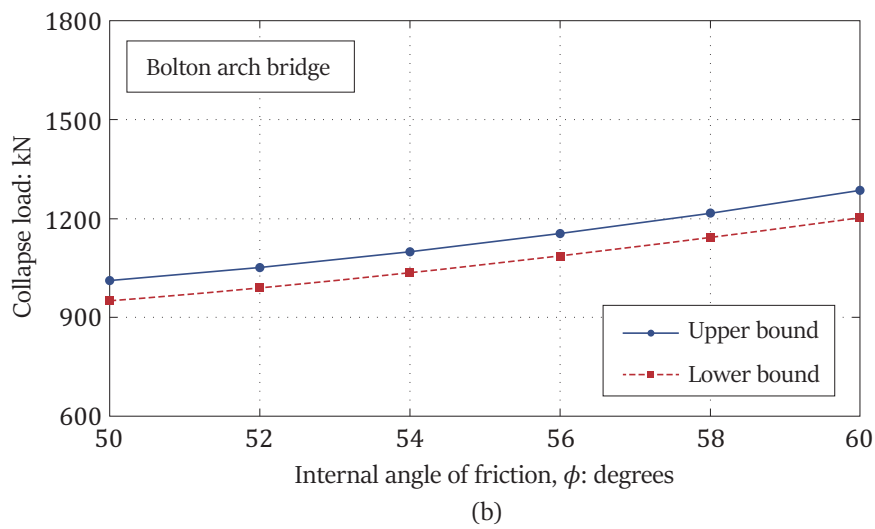
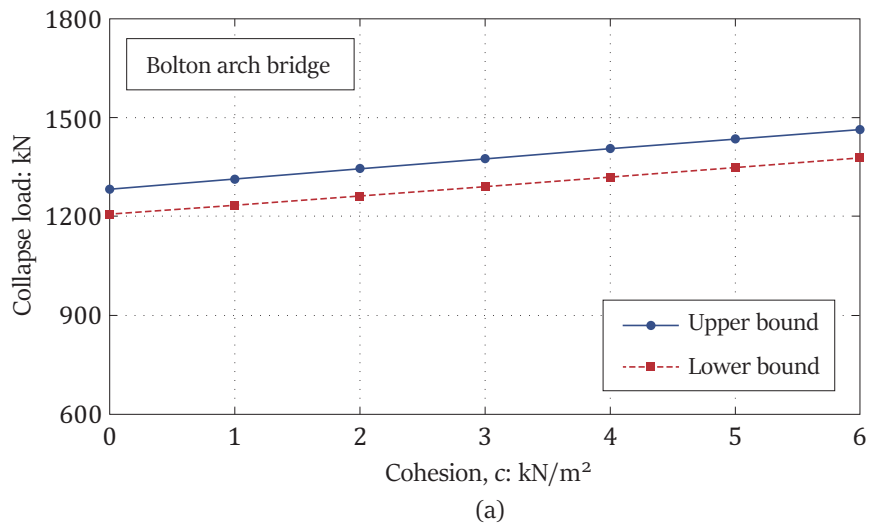
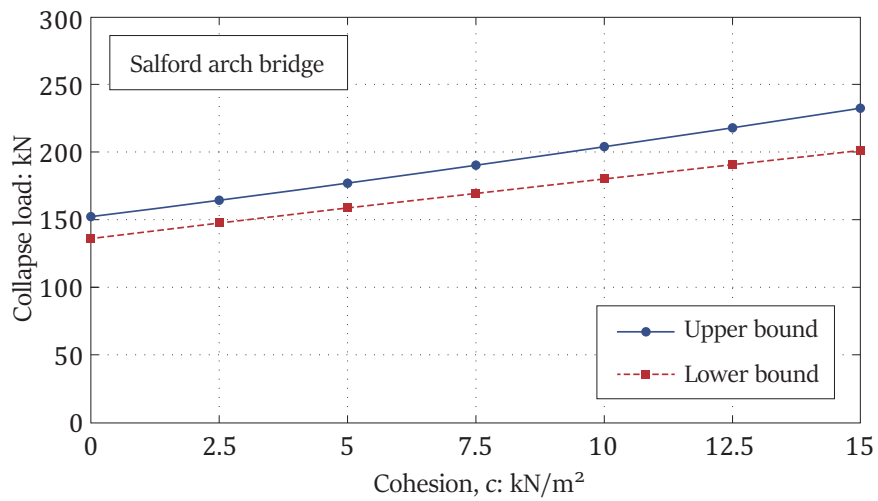
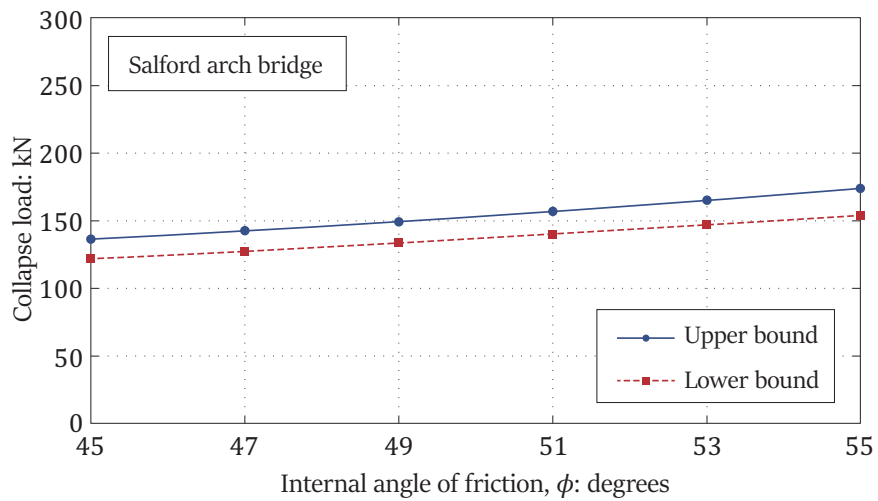


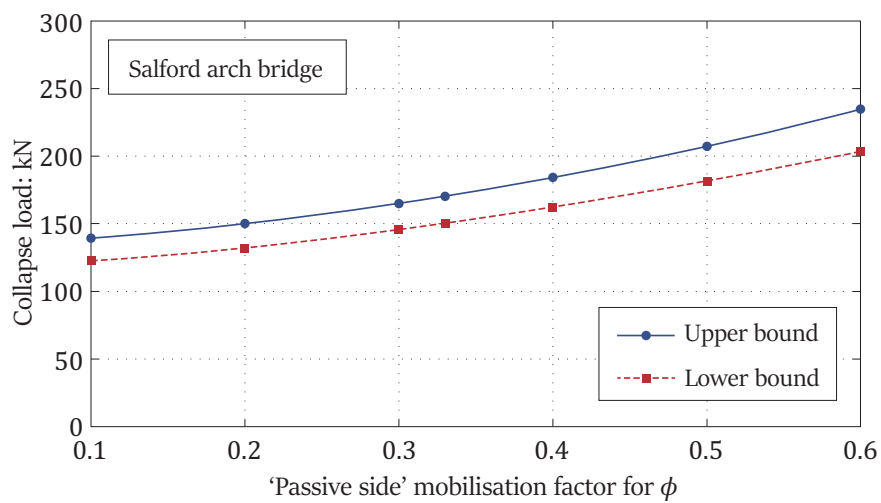
FIGURE 4.23: Parametric study of lower bound solutions for Bolton arch bridge



(a)



(b)



(c)

FIGURE 4.24: Parametric study of lower bound solutions for Salford arch bridge

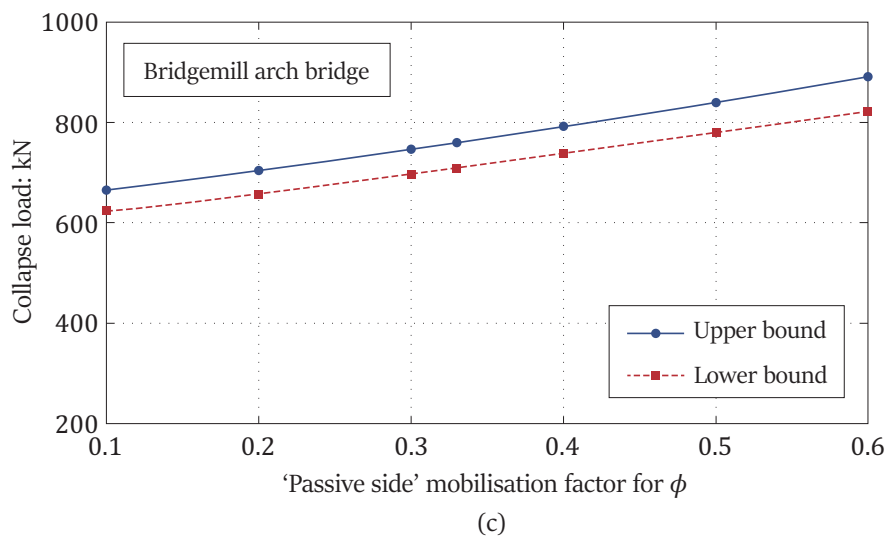
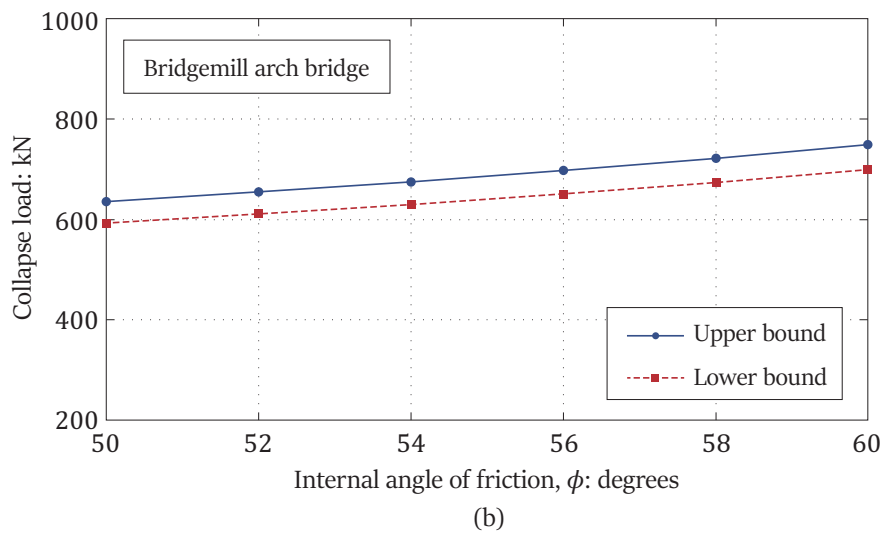
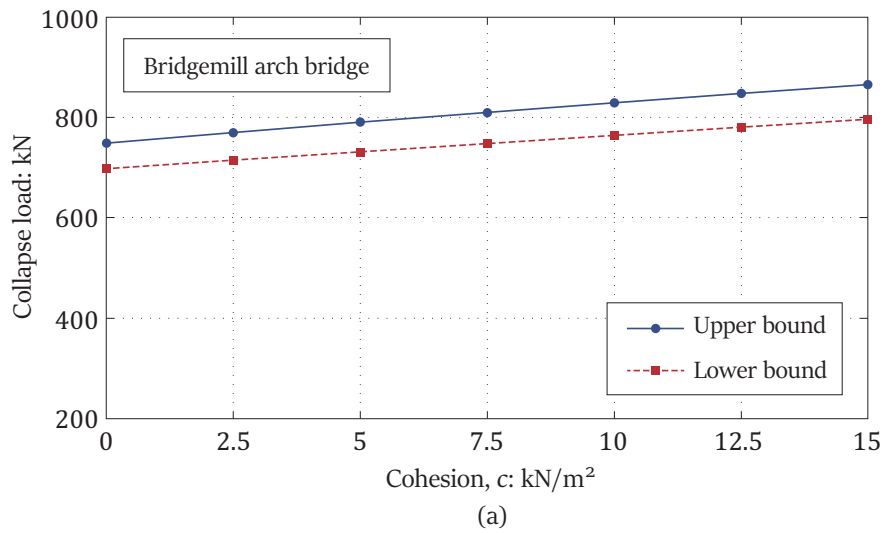


FIGURE 4.25: Parametric study of lower bound solutions for Bridgemill arch bridge

In this parametric study, the gaps between lower- and upper-bound solutions are approximately 4% ~ 23%. This probably is the influence of thinner layer assumption. In section 4.3.5, although an example of footing was designed to show the error from layer less than 8%, the insensible thinner layer could produce a wide gap between lower- and upper-bound solution.

## 4.5 Discussion

The results presented in the masonry and soil model studies appear to indicate that all models satisfy the lower bound theorem, extended to model local failure mechanisms, provides stress fields to lower bound analysis and other analysis procedures for a broad range of problem types.

The masonry arch bridge study illustrates the potential for lower bound limit analysis method, to be applied to challenging soil-structure interaction problems. In this work, lower bound stress fields are simplified as superimposed stresses involving the specified 'Boussinesq' distribution and the stresses due to the loads with those produced by the weight of the supporting material. However, for a good lower bound solution, a complete stress field should be found, to be directly computed by the differential equation of equilibrium and to be supplemented by any effective boundary conditions.

In addition, soil-arch interface is assumed as full rough friction in this chapter, which means the interface frictional strength is same with backfill. In general, friction of the extrados of arch bridges presents  $\delta$  equal to  $0.33\phi$  (soil frictional angle). Thus the soil-arch interface should check yield constraint of  $\tau < \sigma \tan \delta + c'$ , where  $\tau$  and  $\sigma$  is the shear and normal stress at the interface respectively;  $c'$  is the cohesion at the interface. To address it, next step would be develop the computational programme to consider a yield constraint for soil-arch interface.

## 4.6 Concluding Remarks

In summary:

- It has been demonstrated that lower-bound stress fields can be used in conjunction with rigid block limit analysis to provide rapid lower bound estimates of the load carrying capacity of a masonry arch bridge. The lower bound results obtained for a case study bridge model were found to be close to corresponding upper bound solutions obtained using the discontinuity layout optimization (DLO) limit analysis procedure. It was also observed that global and local failure could be modeled using lower bound stress fields (e.g. signaling cases where failure of the traffic surface would in practice occur before failure of the bridge, or alternatively signaling that unrealistically low soil strength properties were used in the model).
- Currently LimitState:RING uses a simplified indirect model of soil-arch interaction, considering dispersal of the applied load, self-weight and passive restraint. The current version of the software assumes that the effects of an applied load can be approximated using stress increments described by vertical Boussinesq stresses, with the horizontal and shear stresses neglected. However, the horizontal and shear stresses (e.g. along the extrados of an arch barrel) can be beneficial or detrimental depending on the scenario. According to lower-bound plastic theory, vertical, horizontal and shear stresses should all be considered. Incorporating the proposed stress fields into LimitState:RING, would therefore allow the software to furnish true lower bound solutions at minimal computational cost.



## Chapter 5

# Rational Limit Equilibrium Method

### Preface

Another strategy of masonry arch bridge analysis in this thesis is the limit equilibrium method. As introduced in Chapter 4, the lower bound stress fields were proposed to be used in conjunction with rigid block limit analysis to provide rapid lower bound estimates of the load-carrying capacity of a masonry arch bridge. However, when very heavy loads are applied on a masonry arch bridge, then lower bound local failure in the soil-fill would in practice occur before failure of the bridge. Thus the soil stress fields are often excessively sensitive, and underestimate the bridge load-carrying capacity. In order to concentrate on the masonry arch bearing capacity, the soil yield constraints are relaxed. The limit equilibrium method is potentially better in this regard as it models stresses in the soil approximately more realistically. Soil earth pressures considering the effects of soil arching and vertical stress distribution due to anisotropic load spreading are used to model the stresses in the soil-fill.

## 5.1 Introduction

The limit equilibrium method has traditionally been used to obtain approximate solutions for the load-carrying capacity of masonry arch bridges. The method of lower bound stress fields has been proposed to obtain true lower bound solutions and the method of discontinuity layout optimization (DLO) has been also introduced to obtain true upper bound solutions. In both of the two methods, soil-fill models in the global system of masonry arch bridges are very sensitive. If low strength of soil is used, failure of the soil-fill often occurs before failure of the arch bridge. In a soil-filled masonry arch bridge, the most important component is the arch ring. Its surrounding soil-fill provides a contribution to the load-carrying capacity of the arch bridge.

LimitState:RING is a commonly used software to estimate the load-carrying capacity of masonry arch bridges. In the current version of LimitState:RING, the soil-fill is assumed to provide self-weight of soil, to disperse applied loading, and to provide restraint to parts of an arch barrel moving into the soil-fill. For dispersion of live loads, the 'Boussinesq' distribution model is used but the distribution is restricted by a dispersed angle to prevent excessive distribution. It is a highly simplified manner. For passive restraint, the 'Rankine' lateral earth pressure theory is used to estimate the amount of horizontal soil stresses. However, this theory is originally developed for retaining walls with a smooth back. In fact the passive earth pressures of masonry arch bridges also need to consider the effect of the roughness of the extrados of the arch.

In this chapter, anisotropic stress formulae and soil earth pressures considering arching effect will be introduced, then the model is applied to soil-filled masonry arch bridges, with results compared with the upper-bound solutions obtained using DLO limit analysis technique procedure.

## 5.2 Anisotropic Stresses Due to Surface Load

The 'Boussinesq' distribution for isotropic material has been often used for an estimation of stresses in loaded soil. However, natural soils often exhibit anisotropic behaviour (Barden 1962, 1963). Moroto (1973, 1990) derived stress solutions in a cross anisotropic soil media under plane strain conditions. These solutions represent different surcharges, such as strip, triangular loads. In this chapter, strip surcharge is used to simulate contact force from a wheel of a vehicle.

For the sake of simplicity, the horizontal and shear stress distributions due to surface loads are neglected in the model of masonry arch bridges. The model generates a suitable 'bell-shaped' distribution of a single load, which the experimental tests

have indicated better approximates reality than the excessive 'Boussinesq' distribution. To address it, vertical anisotropic 'Boussinesq' distribution will be introduced in this chapter.

Figure 5.1 shows a strip surcharge, and a vertical stress  $\Delta\sigma_z$  from equation 4.8 can be re-written as

$$\Delta\sigma_z = \frac{1}{\pi} \frac{\eta_1\eta_2}{\eta_2 - \eta_1} \cdot \left\{ \frac{1}{\eta_1} \left[ \tan^{-1} \frac{b-x}{\eta_1 z} + \tan^{-1} \frac{b+x}{\eta_1 z} \right] - \frac{1}{\eta_2} \left[ \tan^{-1} \frac{b-x}{\eta_2 z} + \tan^{-1} \frac{b+x}{\eta_2 z} \right] \right\} \quad (5.1)$$

where  $\eta_1 = \sqrt{n}$  and  $\eta_2 = 1$ . The degree of anisotropy  $n$  is equal to  $E_x/E_z$ , where  $E_x$  is the horizontal Young's modulus and  $E_z$  is the vertical Young's modulus.

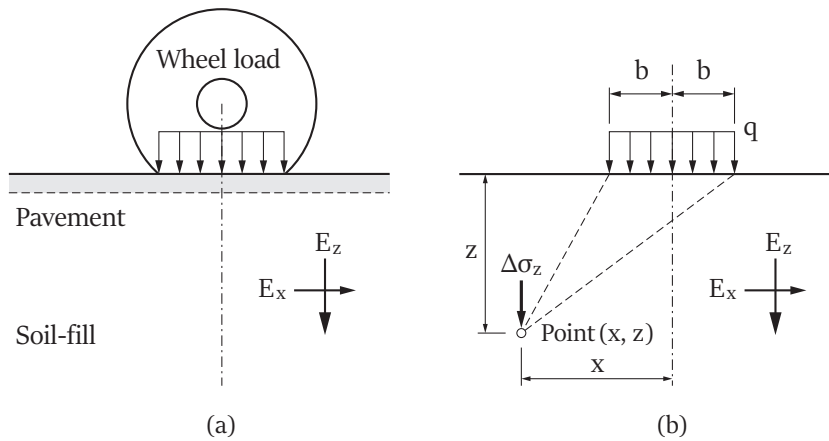
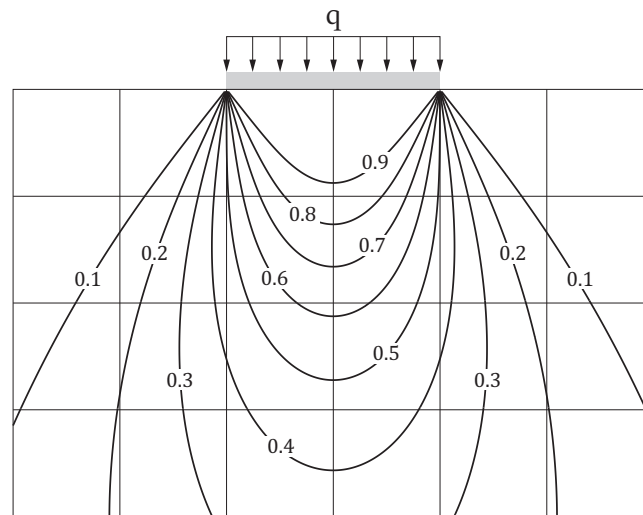
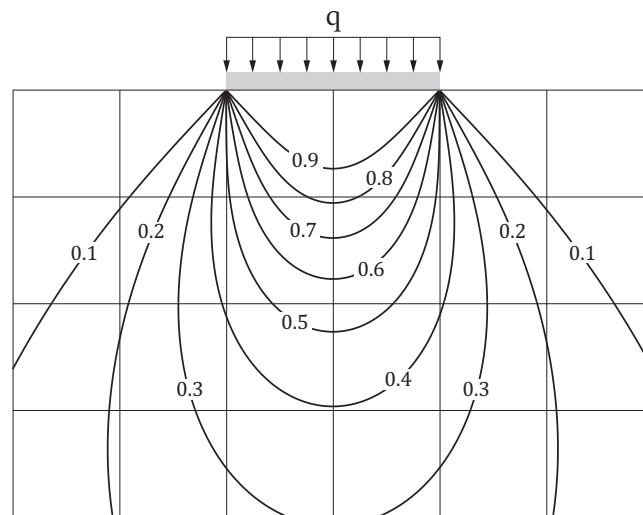


FIGURE 5.1: Cross section through long flexible strip on half-infinite soil carrying surcharges: (a) diagram of a wheel load; (b) diagram of triangular surcharges

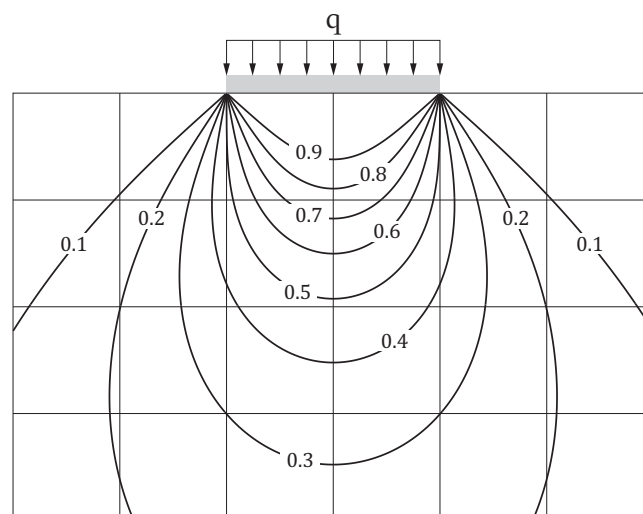
To visualize the increment of stress distribution, the vertical stress increment is demonstrated in Figure 4.20; contours of vertical stress  $\Delta\sigma_z$  under a strip load  $q$  are demonstrated in Figure 5.2(a) ~ (c). In these figures, a smaller  $n$  brings a greater stress concentration and a greater  $n$  brings a greater stress spreading.



(a)



(b)



(c)

FIGURE 5.2: Contours of  $\Delta\sigma_z/q$ : (a)  $n = 0.5$ ; (b)  $n = 1.0$ ; (c)  $n = 2.0$

## 5.3 Soil Earth Pressures of Masonry Arch Bridge

### 5.3.1 Assumptions

A medium-scale test of a typical bridge has been designed by Pytlos to investigate the soil-arch interaction and record soil kinematics of backfilled masonry arch bridges. Figure 5.3 shows the soil displacement of partial image velocity (PIV) at a peak load for the test bridge. The vectors indicated general movement of soil beneath the applied load above the quarter-span, but also show clearly the volume of soil involved in resisting the outward deflection of the arch barrel on the passive side of the arch, remote from the load. In the passive zone, the soil displacement vectors are oriented on average at an angle to the horizontal.

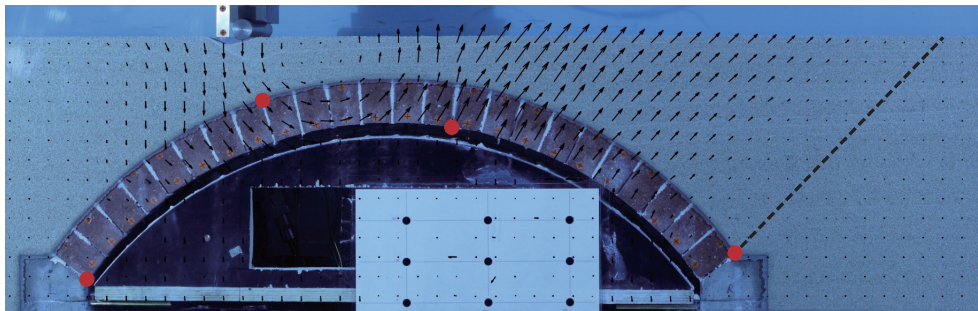


FIGURE 5.3: PIV soil kinematics for a bridge test (after Pytlos 2015)

According to the PIV results, a series of soil-arch interaction models can be assumed. In a problem of a single span masonry arch bridge, a vertical stress distribution from a single load is employed in the limit equilibrium solution which satisfies the equilibrium condition ( Figure 5.4). When the arch ring moves out the soil-fill and into the soil-fill, finite planar elements are considered as shown in Figure 5.5. For the sake of simplicity, the soil-fill between the extrados and crown of the arch ring are divided into two zones: active and passive zones. The surface layer above the crown is assumed to be surcharges due to self-weight of soil.

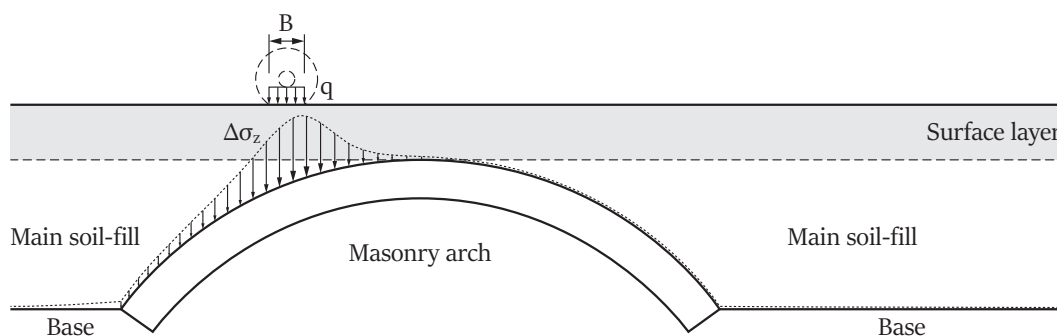


FIGURE 5.4: Vertical stress distribution for live load

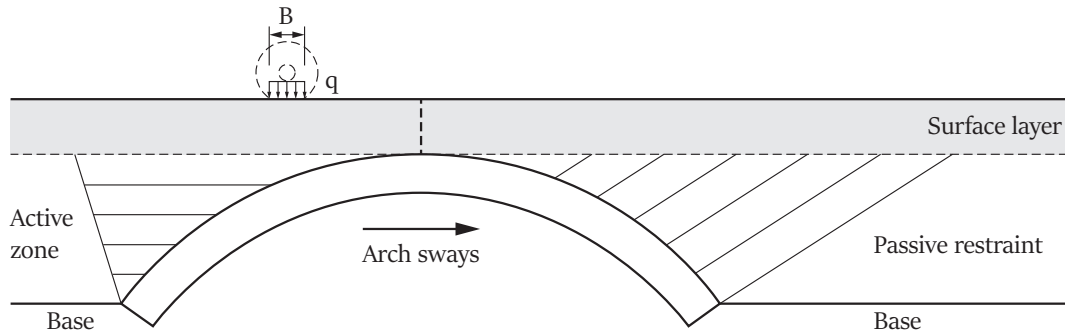


FIGURE 5.5: Finite planar elements for soil-fill

For active zone, a problem of the soil model is similar with a trapdoor test as shown in Figure 5.6(a). Soil arching theory through the trapdoor test has been proposed by Terzaghi (1936, 1943). Arching, as the word suggests, is a stress redistribution process where stress is transferred around a region of the soil mass. In order to investigate the state of stress in the soil considering arching, two parallel and vertical walls are assumed. Figure 5.6(b) shows the weight of a differential planar element in the soil is supported by the wall frictional resistances (Fang & Ishibashi 1986, 1994). These frictional resistances cause changes in the direction of the principal stresses acting on the differential element. The concave arch represented by the dotted lines as shown in Figure 5.6(b).

An experimental study can be used to illustrate the soil arching effect. When a retaining wall moves away from the retained soil, the soil near the wall will drop to fill the gap (Fang et al. 1994, 2002). A concave profile of soil arch between the vertical wall and the shear surface is then mobilized as illustrated in Figure 5.6(b). From the illustration test, it can be seen that failure mechanism of soil wedge behind the wall is different from the assumption of Coulomb theory using a rigid failure wedge. The calculation of the active earth pressures will be illustrated in the next section.

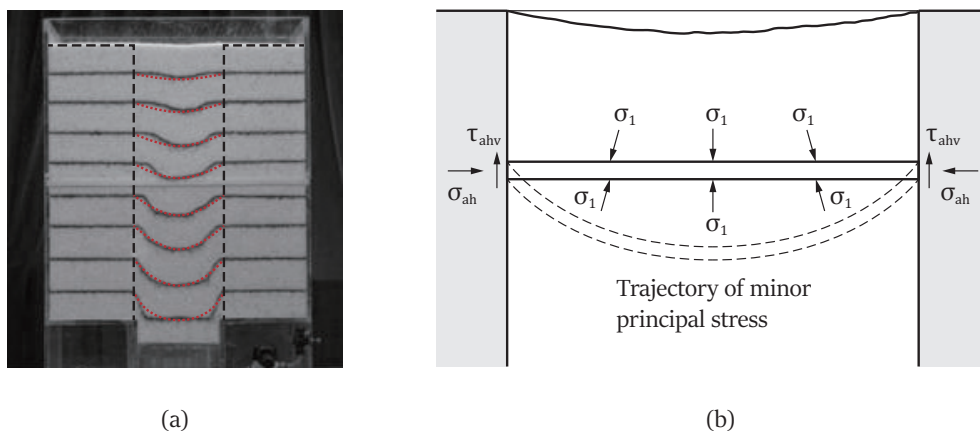


FIGURE 5.6: Soil arching effect: (a) experimental results; (b) trajectory of minor principal stresses (after Paik K. H. and Salgado R. 2003)

### 5.3.2 Active Earth Pressures Against Rigid Wall

In order to estimate active earth pressures, it is important to determine passive earth pressure coefficients. The non-vertical rigid retaining wall is also used to show computations for earth pressures. The retaining wall is considered to retain a cohesionless soil (Figure 5.7(a)). The soil-structure interaction is inclined at an angle  $\varepsilon$  from vertical.  $H$  is the height of the retaining wall and the surcharge loading  $q_s$  on the ground is considered.  $AC$  is the finite flat element of thickness  $dz$  at a depth  $z$  from the ground surface.  $\sigma_{aw}$  and  $\tau_{aw}$  are the normal and shear stresses subjected on the soil-structure interface.

According to soil arching principle, the direction of minor principal stress  $\sigma_3$  in the soil sliding body in limit state is no longer horizontal, but deflection occurs as shown in Figure 5.7(b).  $\delta$  is the friction angle at the soil-structure interface and  $\phi$  is soil friction angle. The inclination  $\beta$  of the rupture surface can be obtained as (Lambe and Whitman 1979)

$$\beta = \tan^{-1} \left\{ \tan \phi \cdot \left[ 1 + \sqrt{1 + \cot \phi \cot (\phi + \delta)} \right] \right\} \quad (5.2)$$

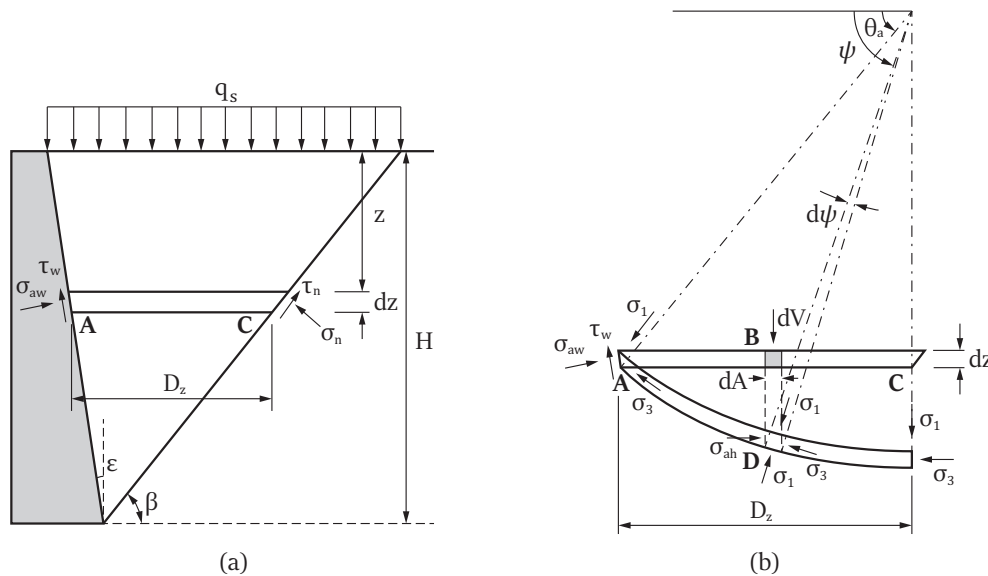


FIGURE 5.7: Concave arch analysis: (a) soil model in active case; (b) stresses on a finite planar element

#### Determination of $\theta_a$

In Figure 5.7(b), the minor principal stress  $\sigma_3$ , on the finite planar element behind the wall acts along the concave arch shown in Figure 5.7(a), whereas the major principal stress  $\sigma_1$  are perpendicular to the concave arch. The shape of the concave arch has been observed or inferred to be elliptic, catenary, or parabolic (Handy 1985). In this

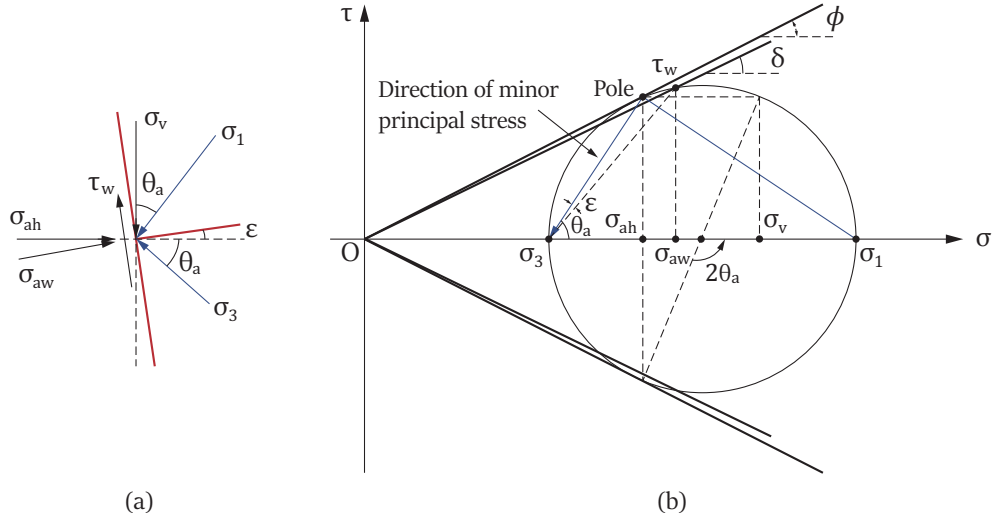


FIGURE 5.8: Mohr-circle for stresses at active retaining wall : (a) stresses at wall; (b) Mohr-circle of stresses at a point

study it is assumed that the trajectory of minor principal stresses takes the form of an arc of a circle (Janssen 1895). The width  $D_z$  of the finite planar element at a depth  $z$  can be expressed as

$$D_z = R \cos \theta_a \quad (5.3)$$

where  $R$  is the radius of the minor principal stress trajectory and  $\theta_a$  is the angle of the minor principal plane with respect to the horizontal line.

Figure 5.8 shows the Mohr-circle representations of stress due to soil arching close to the wall. The normal stress  $\sigma_{aw}$  on the wall is given by

$$\sigma_{aw} = \sigma_1 \cos^2 (\theta_a - \varepsilon) + \sigma_3 \sin^2 (\theta_a - \varepsilon) \quad (5.4)$$

Similarly, the normal stress  $\sigma_{ah}$  at point D of the concave arch, which was originally located at point B, is given by

$$\sigma_{ah} = \sigma_1 \cos^2 \psi + \sigma_3 \sin^2 \psi \quad (5.5)$$

The vertical stress acting on the soil element  $\sigma_v$  is given by

$$\sigma_v = \sigma_1 \sin^2 \psi + \sigma_3 \cos^2 \psi \quad (5.6)$$

The rotation angle  $\theta$  of the principal stresses for the wall with wall frictional angle of  $\delta$  can be obtained using the Mohr-circle, as shown in Figure 5.8(b). The shear stress  $\tau_w$  can be defined as

$$\tau_w = \sigma_{aw} \tan \delta = (\sigma_{aw} - \sigma_3) \tan (\theta_a - \varepsilon) \quad (5.7)$$

Substitution of equation 5.4 into equation 5.7 yields the second-order equation

$$\tan(\theta_a - \varepsilon) = \frac{N + \tan^2(\theta_a - \varepsilon)}{N - 1} \tan \delta \quad (5.8)$$

where  $N = \tan^2(45^\circ + \phi/2)$ .  $N$  is the ratio of major to minor principal stresses.

Solving this equation for  $\theta_a$  gives

$$\theta_a = \tan^{-1} \left[ \frac{(N - 1) + \sqrt{(N - 1)^2 - 4N \tan^2 \delta}}{2 \tan \delta} \right] + \varepsilon \quad (5.9)$$

### Determination of $K_{an}$

The differential vertical force  $dV$  on the shaded element at point B in Figure 5.7(b) can be expressed as

$$dV = \sigma_v dA = \sigma_1 \left( \sin^2 \psi + \frac{1}{N} \cos^2 \psi \right) (R \cdot d\psi \cdot \sin \psi) \quad (5.10)$$

where  $dA$  is the width of the shaded element at point B. The average vertical stress  $\bar{\sigma}_v$  across the differential planar element, as shown in Figure 5.7(b), can be obtained by dividing the total vertical force  $V$  acting on the soil element by the length of the element  $D_z = R \cos \theta_a$

$$\bar{\sigma}_v = \frac{V}{D_z} = \frac{1}{D_z} \int_{\theta}^{\frac{\pi}{2}} dV = \frac{R}{D_z} \int_{\theta}^{\frac{\pi}{2}} \sigma_1 \left( \sin^2 \psi + \frac{1}{N} \cos^2 \psi \right) \frac{\sin \psi}{\cos \theta_a} \cdot d\psi \quad (5.11)$$

Integration of this equation yields

$$\bar{\sigma}_v = \sigma_1 \left( 1 - \frac{N - 1}{3N} \cos^2 \theta_a \right) \quad (5.12)$$

Dividing equation 5.4 by 5.12 gives a ratio  $K_{an}$  of the passive normal stress at the wall to the average vertical stress over the finite planar element

$$K_{an} = \frac{\sigma_{aw}}{\bar{\sigma}_v} = \frac{3[N \cos^2(\theta_a - \varepsilon) + \sin^2(\theta_a - \varepsilon)]}{3N - (N - 1) \cos^2 \theta_a} \quad (5.13)$$

### Force equilibrium of z-direction

Taking the sliding wedge as an isolated unit, as shown in Figure 5.8, an element of thickness  $dz$  is taken from the wedge at a depth  $z$  below the ground surface.

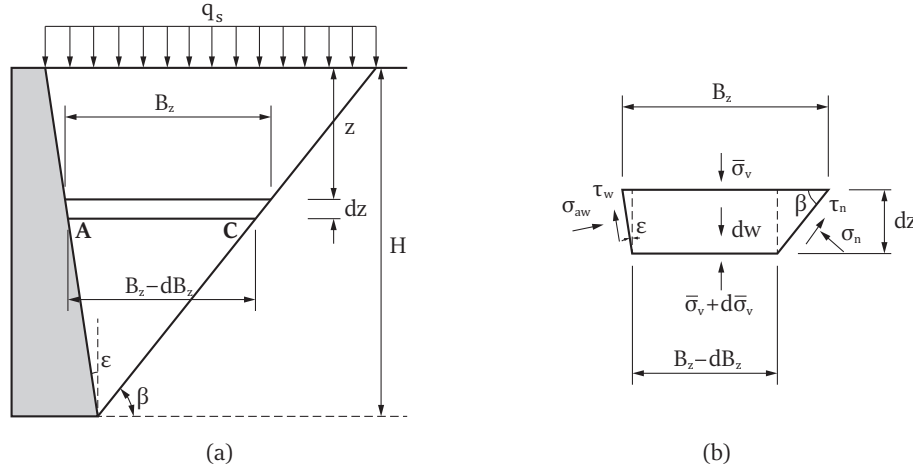


FIGURE 5.9: Force equilibrium analysis in active zone: (a) diagram of an isolated element unit; (b) force analysis

The forces on this element involve the vertical pressure  $\bar{\sigma}_v$  on the top of the element, the vertical reaction  $\bar{\sigma}_v + d\bar{\sigma}_v$  on the bottom of the element, the normal stress  $\sigma_{aw}$  on the retaining wall, the shear stress  $\tau_w$  on the back of the retaining wall, the normal stress  $\sigma_n$  of the soil at rest, the shear stress  $\tau_n$  on the retained soil, the weight  $dw$  of the element expressed as

$$dw = \frac{\gamma}{2} (B_z + B_z - dB_z) dz = \gamma B_z dz \quad (5.14)$$

omitting the second-order differential terms. The width of the soil element  $B_z$  at a depth of  $z$  can be expressed as

$$B_z = \frac{H - z}{\cos \varepsilon} \cdot \frac{\cos(\beta - \varepsilon)}{\sin \beta} = (H - z) \cdot \frac{1 + \tan \varepsilon \tan \beta}{\tan \beta} \quad (5.15)$$

The increase of the element width  $dB_z$  at a depth of  $z + dz$  can be expressed as

$$dB_z = dz (\tan \varepsilon + \cot \beta) \quad (5.16)$$

The force equilibrium in the  $z$ -direction can be defined as

$$\begin{aligned} & \bar{\sigma}_v B_z + dw - (\bar{\sigma}_v + d\bar{\sigma}_v) (B_z - dB_z) - \sigma_{aw} \frac{dz}{\cos \varepsilon} \sin \varepsilon \\ & - \tau_w \frac{dz}{\cos \varepsilon} \cos \varepsilon - \sigma_n \frac{dz}{\sin \beta} \cos \beta - \tau_n \frac{dz}{\sin \beta} \sin \beta = 0 \end{aligned} \quad (5.17)$$

Substituting equations 5.14 ~ 5.16 into equation 5.17, one may get the simplification as

$$\frac{d\bar{\sigma}_v}{dz} = \gamma + \frac{\bar{\sigma}_v}{H-z} - \frac{\sigma_{aw} \tan \varepsilon \tan \beta + \sigma_n + (\tau_w + \tau_n) \tan \varepsilon}{(H-z)(1 - \tan \beta \tan \varepsilon)} \quad (5.18)$$

### Force equilibrium of $x$ -direction

The force equilibrium in the  $x$ -direction can be defined as

$$\sigma_{aw} \frac{dz}{\cos \varepsilon} \cos \varepsilon - \tau_w \frac{dz}{\cos \varepsilon} \sin \varepsilon - \sigma_n \frac{dz}{\sin \beta} \sin \beta + \tau_n \frac{dz}{\sin \beta} \cos \beta = 0 \quad (5.19)$$

and can be written as

$$\sigma_{aw} - \tau_w \tan \varepsilon = \sigma_n - \tau_n \cot \varepsilon \quad (5.20)$$

For the shear stress acting on the soil element at the point A,  $\tau_w$  is given by

$$\tau_w = \sigma_{aw} \tan \delta \quad (5.21)$$

For the shear stress acting on the soil element at the point C,  $\tau_n$  is given by

$$\tau_n = \sigma_n \tan \phi \quad (5.22)$$

Equations 5.21 and 5.22 can be substituted into equation 5.20 to derive an expression for  $\sigma_n$  in terms of  $\sigma_{aw}$ . Then, substituting the expression of  $\sigma_n$ , and equation 5.28 into equation 5.18, it can be simplified to

$$\frac{d\bar{\sigma}_v}{dz} = \gamma + \frac{\bar{\sigma}_v}{H-z} \cdot C_a \quad (5.23)$$

where

$$C_a = \frac{\left\{ \tan \varepsilon + \cot \beta - K_{an} \left[ \tan \varepsilon + \tan \delta + \frac{1 - \tan \delta \tan \varepsilon}{1 - \tan \phi \cot \beta} (\cot \beta + \tan \phi) \right] \right\} \tan \beta}{\cot \beta + \tan \varepsilon}$$

Equation 5.22 is a first-order differential equation for the vertical unit earth pressure. This equation may be solved based on the boundary condition. In the absence of surcharge pressure at the ground surface, the boundary condition will be  $\bar{\sigma}_v = 0$  at  $z = 0$ . But in the presence of surcharge pressure say  $q_s$ , the boundary condition will be  $\bar{\sigma}_v = q_s$  at  $z = 0$ .

If assume that there is a surcharge pressure  $q_s$  at the ground surface, the solution of the equation 5.23 is expressed as

$$\bar{\sigma}_v = \left( q_s + \frac{\gamma H}{C_a + 1} \right) \left( 1 - \frac{z}{H} \right)^{-C_a} - \frac{\gamma H}{C_a + 1} \left( 1 - \frac{z}{H} \right) \quad (5.24)$$

The active normal stress at any depth acting on the wall can be calculated by multiplying equation 5.23 by  $K_{an}$  which is given by equation 5.12

$$\sigma_{aw} = K_{an} \left[ \left( q_s + \frac{\gamma H}{C_a + 1} \right) \left( 1 - \frac{z}{H} \right)^{-C_a} - \frac{\gamma H}{C_a + 1} \left( 1 - \frac{z}{H} \right) \right] \quad (5.25)$$

**Parametric study**

In order to visualize the sensitivity of soil-wall interface friction and inclined angle, a parametric study (see Figure 5.10) was conducted to investigate the influence of interface friction and soil strength. Figure 5.10(a) shows that with a smooth-faced vertical retaining wall the lateral stress distribution is same to the ‘Rankine’ active lateral earth pressure. In the case of a rough-faced vertical retaining wall, higher interface friction brings smaller active earth pressures. The resultants of active earth pressure against the inclined retaining wall are larger than the resultants against the vertical wall. The relationship between vertical and lateral stress is non-linearly.

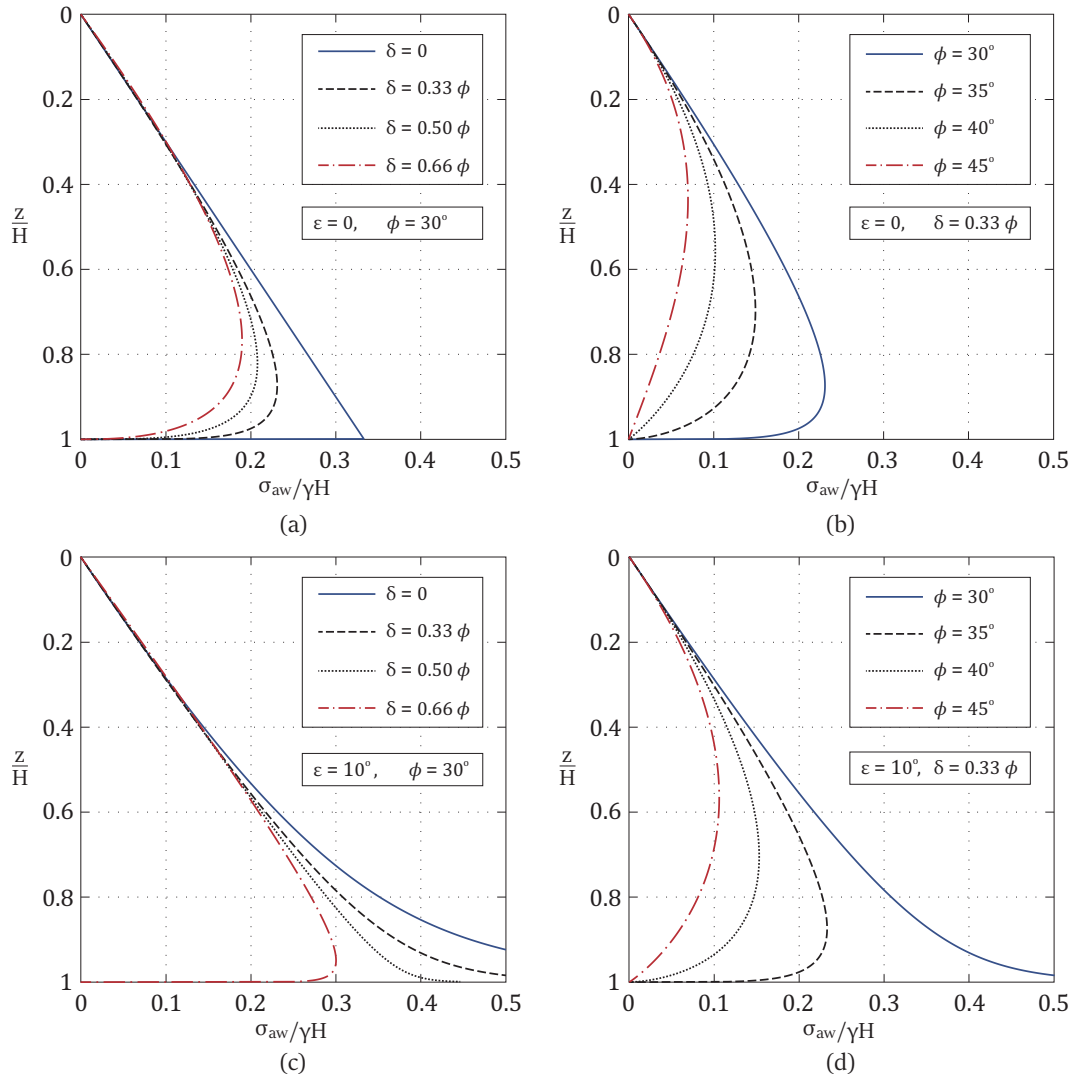


FIGURE 5.10: Parametric study for active retaining wall

### 5.3.3 Passive Earth Pressures Against Rigid Wall

A series of retaining wall tests have been designed by Niedostatkiewicz et al. (2011) to investigate the earth pressures. The experimental results indicated the earth pressures against the rigid wall is due to the thrust exerted by a series of soil wedges between the wall and the rupture surface (Figure 5.11(a)). The lower part of the surface could be concave, convex or plane, but the entire surface tends to be a plane. For the sake of simplicity, in this chapter it defines this surface as a plane. The retaining wall is rigid with an inclination angle  $\varepsilon$ , and the surcharge loading  $q_s$  on the ground level is considered. The rupture surface passes through the heel of the wall and it is a plane with an inclination of  $\alpha$ . In order to calculate the earth pressures, the soil-structure friction  $\delta$  and internal soil friction angle  $\phi$  need to be determined.

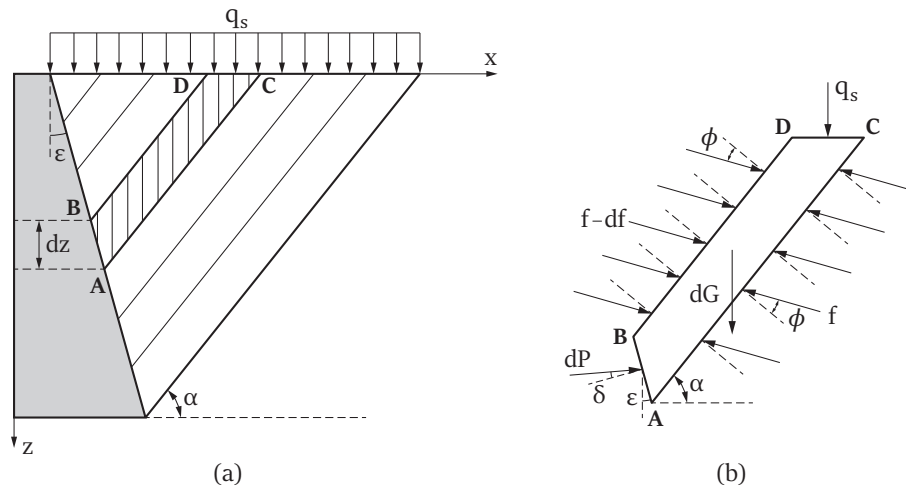


FIGURE 5.11: Soil wedge analysis: (a) soil model in passive case; (b) stresses on a finite planar element

#### Force equilibrium

Taking a soil wedge ABCD as an isolated unit, it is part of the thrust wedge in Figure 5.11(a) at depth  $z$  and the upper surface BD is parallel to the lower surface AC. The soil wedge ABCD is subjected to the stresses as shown in Figure 5.11(b), where the resultant passive earth pressure is  $dP$ , the top surface stress is  $q_s$ , the lower surface stress is  $f$ , the upper surface stress is  $f - df$  and the self-weight of the soil wedge  $dG$ . The geometric parameters of the soil wedge ABCD are expressed as

$$\begin{cases} \overline{AB} = \frac{dz}{\cos \varepsilon} & \text{and} & \overline{DC} = \frac{dz}{\cos \varepsilon} \cdot \cos(\alpha - \varepsilon) \cdot \frac{1}{\sin \alpha} \\ \overline{AC} = \frac{z}{\sin \alpha} & \text{and} & \overline{BD} = \overline{AC} - \frac{dz \sin(\alpha - \varepsilon)}{\cos \varepsilon} - \frac{dz \cos(\alpha - \varepsilon)}{\cos \varepsilon \tan \theta} \end{cases} \quad (5.26)$$

omitting the second-order differential terms. The self-weight of the soil wedge  $dG$  can be obtained as

$$dG = \frac{1}{2} \gamma (\overline{AC} + \overline{BD}) \frac{dz \cos(\alpha - \varepsilon)}{\cos \varepsilon} = \frac{dz \cos(\alpha - \varepsilon)}{\sin \alpha \cos \varepsilon} \cdot \gamma z \quad (5.27)$$

The passive earth pressure  $dP$  is given by

$$dP = \sigma_p \cdot dz \quad (5.28)$$

where  $\sigma_p$  is the passive earth pressure.

The force equilibrium in the  $x$ -direction can be defined as

$$dP \cos(\varepsilon - \delta) + (f - df) \overline{BD} \sin(\alpha + \phi) = f \overline{AC} \sin(\alpha + \phi) \quad (5.29)$$

and can be written as

$$(f - df) \overline{BD} = f \overline{AC} - dP \cdot \frac{\cos(\varepsilon - \delta)}{\sin(\alpha + \phi)} \quad (5.30)$$

The force equilibrium in the  $z$ -direction can be defined as

$$dP \sin(\varepsilon - \delta) + f \overline{AC} \cos(\alpha + \phi) = dG + (f - df) \overline{BD} \cos(\alpha + \phi) + q_s \overline{DC} \quad (5.31)$$

Substituting equations 5.27 and 5.30 into equation 5.31, one may get the simplification as

$$\sigma_p = \frac{\cos(\alpha - \varepsilon) / (\sin \alpha \cos \varepsilon)}{\sin(\varepsilon - \delta) + \cos(\varepsilon - \delta) \cot(\alpha + \phi)} (\gamma z + q_s) = g(\alpha) (\gamma z + q_s) \quad (5.32)$$

omitting the second-order differential terms. Thus the expression of the initial passive earth pressure coefficient is given by

$$g(\alpha) = \frac{\cos(\alpha - \varepsilon) / (\sin \alpha \cos \varepsilon)}{\sin(\varepsilon - \delta) + \cos(\varepsilon - \delta) \cot(\alpha + \phi)} \quad (5.33)$$

### Determine inclination angle of rupture surface

In order to determine the inclination angle  $\alpha$ , it can be achieved by using calculus such as  $dg(\alpha)/d\alpha = 0$  and  $d^2g(\alpha)/d\alpha^2 > 0$  to determine the mathematical minimum for  $g(\alpha)$  as  $\alpha$  is allowed to vary.

According to trigonometry theorems, the expressions of  $\cos(\alpha - \varepsilon)$  and  $\sin \alpha$  can be derived as

$$\begin{cases} \cos(\alpha - \varepsilon) = \cos[(\alpha + \phi) - (\phi + \varepsilon)] \\ \quad = \cos(\alpha + \phi) \cos(\phi + \varepsilon) + \sin(\alpha + \phi) \sin(\phi + \varepsilon) \\ \sin \alpha = \sin[(\alpha + \phi) - \phi] = \sin(\alpha + \phi) \cos \phi - \cos(\alpha + \phi) \sin \phi \end{cases} \quad (5.34)$$

Substitute equation 5.34 into equation 5.33, then one may get the simplification as

$$g(\alpha) = \frac{\tan(\alpha + \phi)}{[\tan(\alpha + \phi) \sin(\varepsilon - \delta) + \cos(\varepsilon - \delta)] \cos \varepsilon} \cdot \frac{\cos(\phi + \varepsilon) + \tan(\alpha + \phi) \sin(\phi + \varepsilon)}{\tan(\alpha + \phi) \cos \phi - \sin \phi} \quad (5.35)$$

The variable  $\alpha$  of equation 5.35 can be replaced by  $\tan(\phi + \varepsilon)$ , then the calculus can be expressed as

$$\frac{dg(\tan(\phi + \varepsilon))}{d(\tan(\phi + \varepsilon))} = 0 \quad (5.36)$$

This first-order differential equation can be derived as

$$C_p \tan^2(\phi + \varepsilon) + D_p \tan(\phi + \varepsilon) + E_p = 0 \quad (5.37)$$

where

$$\begin{cases} C_p = \cos \varepsilon \tan(\varepsilon - \delta) - \sin(\phi + \varepsilon) \cos \phi \\ D_p = \cos \varepsilon - \cos(2\phi + \varepsilon) \\ E_p = \sin \phi \cos(\phi + \varepsilon) \end{cases} \quad (5.38)$$

The solutions of equation 5.37 can be obtained as

$$\tan(\phi + \varepsilon) = \omega_p = \frac{-D_p \pm \sqrt{D_p^2 - 2C_p E_p}}{2C_p} \quad (5.39)$$

The lower of the two solutions gives a valid inclination angle  $\alpha$ , and the value of  $\alpha$  is given by

$$\alpha = \tan^{-1} \omega_p - \phi \tag{5.40}$$

Substituting equation 5.39 into equation 5.35, one may get the simplification as following

$$K_{p\phi} = g(\alpha) = \frac{\omega_p}{[\omega_p \sin(\varepsilon - \delta) + \cos(\varepsilon - \delta)] \cos \varepsilon} \frac{\cos(\phi + \varepsilon) + \omega_p \sin(\phi + \varepsilon)}{\omega_p \cos \phi - \sin \phi} \tag{5.41}$$

Substitute equation 5.41 into equation 5.32, then the passive normal earth pressure can be obtained as

$$\sigma_{pw} = K_{p\phi} (\gamma z + q_s) \cos \delta \tag{5.42}$$

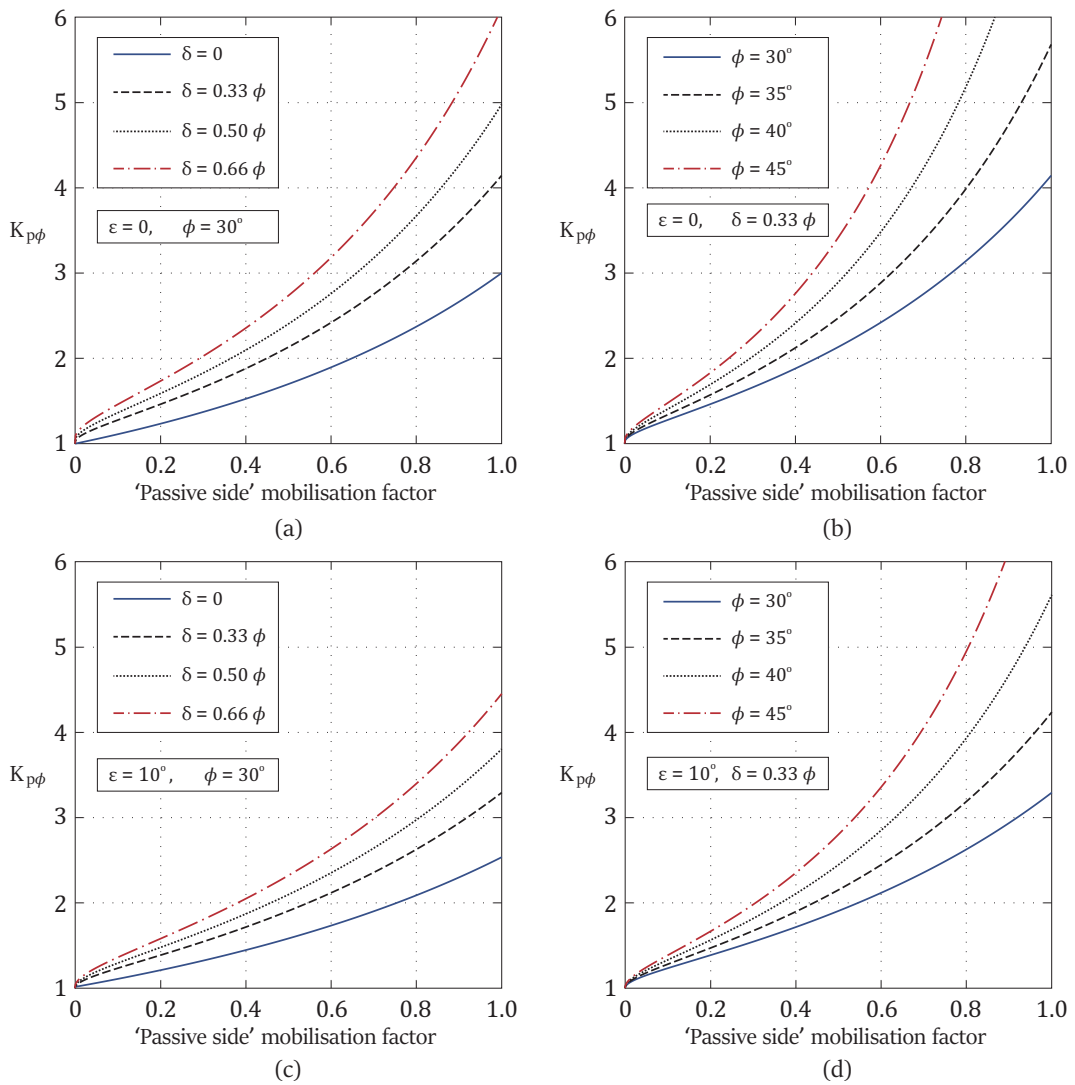


FIGURE 5.12: Parametric study for passive retaining wall

### Parametric study

To visualize the sensitivity of soil-structure interface friction and inclined angle, it is necessary to conduct a parametric study (Figure 5.12). In Figure 5.12(a), it can be seen that in case of smooth vertical retaining wall, passive earth pressure coefficients  $K_{p\phi}$  are the same to the 'Rankine' passive lateral earth pressure coefficients. When 'passive side' mobilisation factor is equal to zero, it means the soil mass becomes the ideal material, and the value of  $K_{p\phi}$  equals one. In the case of a rough-faced vertical retaining wall, higher interface friction brings larger passive earth pressures. The resultants of passive earth pressure against the inclined retaining wall are smaller than the resultants against the vertical wall.

### 5.3.4 Simple Example of Rigid Embedded Cantilever Retaining Wall

A rigid embedded cantilever retaining wall (Figure 5.13) that retains soil of height  $H$  and is embedded a depth  $d$  into the soil is considered to illustrate the application of the theoretical soil models. Such an analysis requires that moments induced by assumed active and passive earth pressure distributions either side of the wall, above an assumed point of rotation, are in static equilibrium; that is

$$\frac{\lambda \gamma K_a (d + h)^3}{6} = \frac{\gamma K_p d^3}{6} \quad (5.43)$$

where  $K_a$  and  $K_p$  are the active and passive earth pressure coefficients respectively,  $\gamma$  is the soil unit weight,  $d$  is the depth to the point of rotation, and  $\lambda$  is a load factor on the retained soil weight. In this problem,  $K_p$  is equal to  $K_{p\phi}$  expressed in equation 5.41. The value of  $K_a$  can be equivalent to the resultant active force  $P_{ah}$  divided by  $\gamma H^2/2$ . The active force  $P_{ah}$  on the wall can be obtained by integrating equation 5.25 with respect to  $z$

$$P_a = \int_0^H \sigma_{aw} dz = \frac{K_{an}}{1 - C_a} \left( q_s H + \frac{\gamma H^2}{2} \right) \quad (5.44)$$

In this problem,  $q_s$  is equal to zero then  $K_a$  can be expressed as

$$K_a = \frac{K_{an}}{1 - C_a} \quad (5.45)$$

Comparisons with the DLO results are made by evaluating the value of  $\phi$  required in the DLO analysis to replicate the theoretical value of  $\lambda$ . Table 5.1 and 5.2 show the results of comparison between the theoretical soil models and the numerical DLO models. It can be seen that the error of the smooth wall case is less than 2% and the rough wall case is approximately 8%.

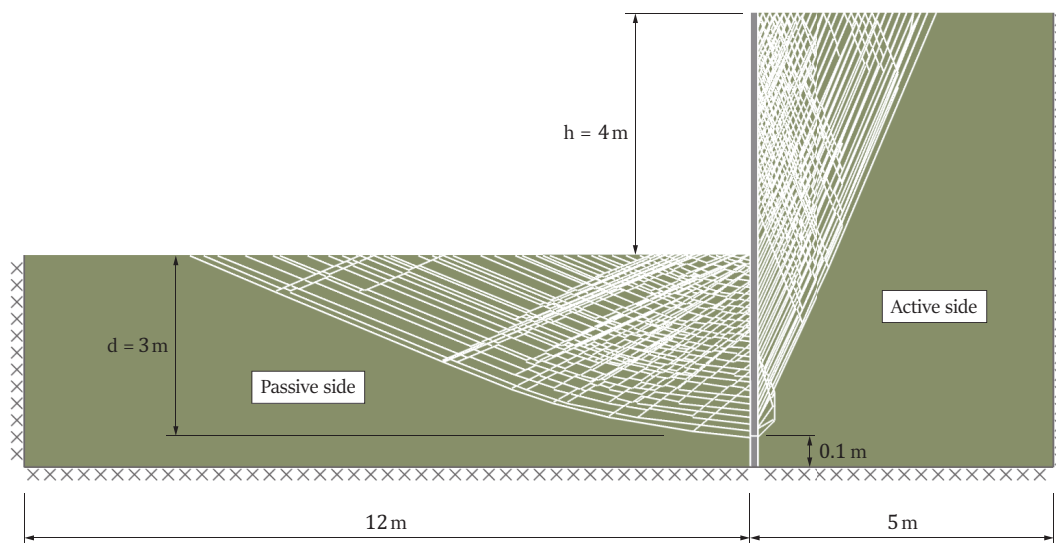


FIGURE 5.13: DLO simulation of embedded cantilever wall ( $d = 3$  m,  $h = 4$  m) using 2000 nodes with  $\phi = 45^\circ$  and  $\delta = 0.33$  (wall thickness increased to 0.1 m for visual clarity)

TABLE 5.1: Comparison of theory and DLO results for the embedded cantilever retaining wall with  $\delta = 0$  (2000 nodes used in DLO)

$\phi: ^\circ$	$K_a$	$K_p$	$\lambda_{\text{theory}}$	$\phi_{2000}: ^\circ$	$\phi_{2000}/\phi$
30	0.33	3.00	0.71	29.5	0.98
35	0.27	3.69	1.07	34.5	0.99
40	0.22	4.60	1.66	39.6	0.99
45	0.17	5.83	2.67	44.4	0.99

TABLE 5.2: Comparison of theory and DLO results for the embedded cantilever retaining wall with  $\delta = 0.33 \phi$  (2000 nodes used in DLO)

$\phi: ^\circ$	$K_a$	$K_p$	$\lambda_{\text{theory}}$	$\phi_{2000}: ^\circ$	$\phi_{2000}/\phi$
30	0.29	4.14	1.16	32.0	1.07
35	0.20	5.68	2.35	37.8	1.08
40	0.14	8.15	4.94	43.2	1.08
45	0.09	12.47	10.91	48.6	1.08

### 5.3.5 Simple Example of Backfilled Masonry Arch Bridge

A masonry arch bridge that fills soil of internal friction angle  $\phi$  is considered to illustrate the application of the theoretical soil models. The main geometric parameters are shown in Figure 5.14(a). It was designed that a point load is subjected at quarter-span of the bridge, the 'passive side' mobilisation factor is the third of  $\phi$ . Considering the passive restraints of the bridge, the passive zone model (remote to the load) requires that the soil friction  $\phi$  is mobilised as one-third of  $\phi$ .

For active earth pressures, the calculation is simplified that each voussoir is an isolated 'retaining wall' against these soil stresses  $\sigma_{aw}$  and  $\tau_{aw}$  which are expressed as

$$\begin{cases} \sigma_{aw} = K_{an} \left[ \left( q_s + \frac{\gamma H}{C_a + 1} \right) \left( 1 - \frac{z}{H} \right)^{-C_a} - \frac{\gamma H}{C_a + 1} \left( 1 - \frac{z}{H} \right) \right] \\ \tau_{aw} = \sigma_{aw} \cdot \tan \delta \end{cases} \quad (5.46)$$

Similarly, in passive zone the calculation is also simplified that each voussoir is an isolated 'retaining wall' against passive earth pressures  $\sigma_{pw}$  and  $\tau_{pw}$  which are expressed as

$$\begin{cases} \sigma_{pw} = K_{p\phi} (\gamma z + q_s) \cos \delta \\ \tau_{pw} = \sigma_{pw} \cdot \tan \delta \end{cases} \quad (5.47)$$

These soil pressures are used in conjunction with rigid-block limit analysis to provide rapid estimation of the load-carrying capacity of the masonry arch.

Comparisons with the DLO results for the adequacy factor  $\lambda$  of bridge load-bearing capacity, are useful to validate the application of theoretical soil models in the masonry arch bridge problem. A failure mechanism of DLO simulation is shown in Figure 5.14(b). Table 5.3 shows the results of comparison between the theoretical soil models and the numerical DLO models. From this table, it can be seen that the error of the smooth soil-arch interaction case is less than 2% and the rough case is approximately 4%.

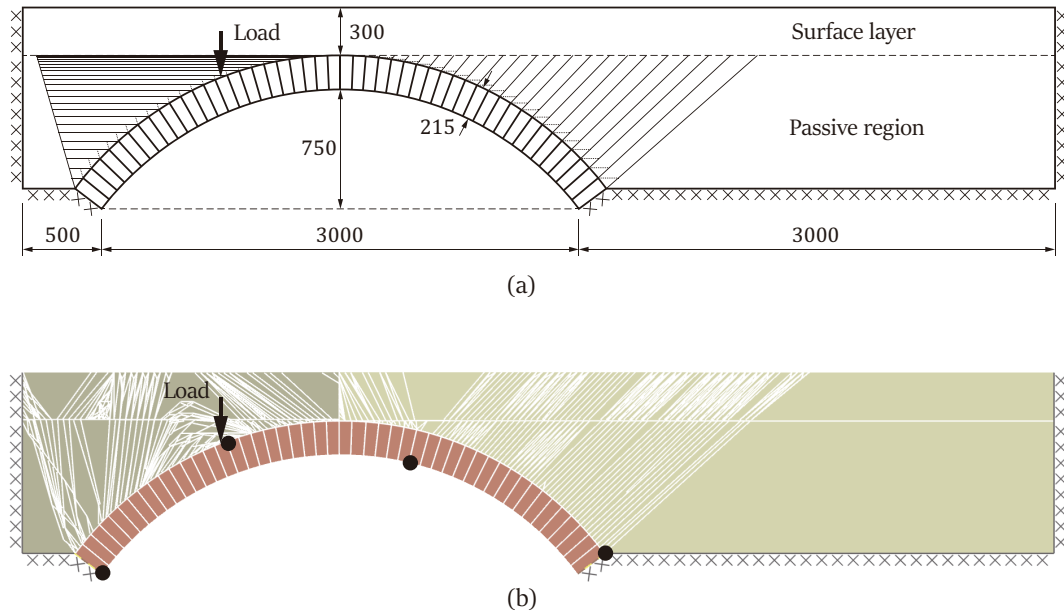


FIGURE 5.14: A simple example of masonry arch bridge: (a) theoretical models (all dimensions in mm); (b) DLO simulation with  $\delta = 0.33$  (2000 nodes used)

TABLE 5.3: Comparison of theory and DLO results for the masonry arch bridge (2000 nodes used in DLO)

$\phi: ^\circ$	$\delta = 0$			$\delta = 0.33$		
	$\lambda_{\text{equ}}$	$\lambda_{\text{DLO}}$	$\lambda_{\text{equ}}/\lambda_{\text{DLO}}$	$\lambda_{\text{equ}}$	$\lambda_{\text{DLO}}$	$\lambda_{\text{equ}}/\lambda_{\text{DLO}}$
30	60.46	61.02	0.99	61.70	63.17	0.98
35	62.12	63.06	0.99	63.39	65.70	0.96
40	63.80	65.23	0.98	65.75	68.41	0.96
45	66.62	67.57	0.99	68.59	71.51	0.96
50	68.98	70.25	0.98	72.46	75.13	0.96
55	72.47	73.44	0.99	77.91	79.53	0.96
60	77.51	77.41	1.00	86.32	85.28	1.02

## 5.4 Application to Case Studies

The use of the proposed limit equilibrium method can be illustrated by considering literature bridges (e.g. Bolton, Salford, Bridgemill arch bridge). The main bridge geometry and the relative material properties are shown in section 2.4. The upper-bound solutions obtained using DLO limit analysis technique can be compared with the proposed limit equilibrium solutions.

In the limit equilibrium soil models, the cohesive material with strength cohesion  $c$  and friction  $\phi$  can be equivalent to friction  $\phi_e$  using equation 5.25. For the anisotropic 'Boussinesq' vertical stress distribution, the most sensitive parameter,  $n$ , was used to evaluate the soil stress spreading capacity. Because of no yield conditions to constraint the anisotropic factor  $n$ , here an exponential function was created to determine the value of  $n$  in the analysis of masonry arch bridges. Through the trail error, the expression of  $n$  is given as

$$n = \zeta \cdot \left( \frac{\phi_e}{\phi_c} \right) \cdot \exp \left[ \left( \frac{\phi_e}{\phi_c} \right) - 1 \right] \quad (5.48)$$

where  $\zeta$  is the soil-arch interface strength multiplier;  $\phi_c$  is the internal friction angle of  $60^\circ$  which is the soil strength commonly used in masonry arch bridges.

In the DLO simulations, a geometrical model common to the masonry arch bridge was created. Appropriate material properties, same as the limit equilibrium, were then applied to each geometrical region. All regions were then discretised using nodes, with a relatively large target number of nodes (5000) being employed.

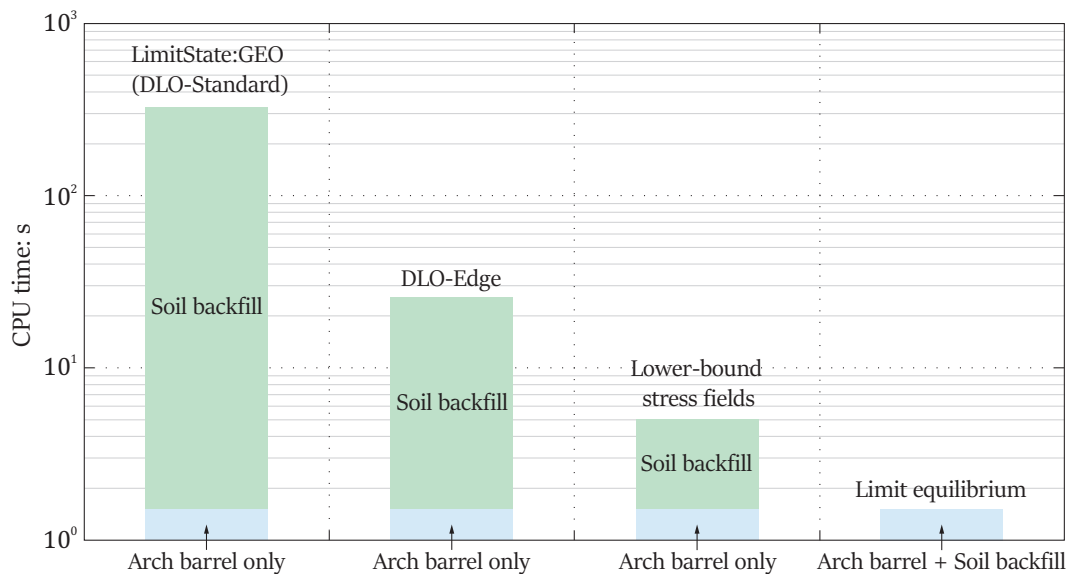


FIGURE 5.15: CPU time comparison of DLO-standard, DLO-edge, lower-bound stress fields and limit equilibrium

For the CPU times, it is necessary to compare different methods for a single load case. Figure 5.15 indicates that the limit equilibrium method (1.2 s) is faster than the current version of LimitState:GEO (330 s) and fast running DLO (25.8 s) and lower-bound stress fields (4.9 s) CPU times.

In order to investigate key three parameters (e.g. internal friction angle  $\phi$ , 'passive side' mobilisation factor and soil-arch interface strength multiplier  $\zeta$ ) utilized in the assessment of masonry arch bridge, a parametric study was carried out in the application of limit equilibrium and upper-bound method to literature bridges. The three parameters were varied in turn while others. The default values of three parameters for each bridge are listed in section 2.4. The results are shown in Figure 5.16 ~ 5.18. From these figures, it can be seen that the assessments of the bridge load-carrying capacity using limit equilibrium ( $n$  was obtained from equation 5.48) have a good agreement with the results of DLO limit analysis.

In this parametric study, the gaps between limit equilibrium and upper-bound solutions in the global failure cases are less than 4%. However, the local failure is not considered in the limit equilibrium so that in the cases of local failure (e.g. low-strength fill) the gaps between the two methods are more than 23%.

## 5.5 Discussion

The results presented in the masonry arch bridge study appear to indicate that the limit equilibrium method provides approximate solutions for the estimation of the bridge load-carrying capacity. In this method, it makes sufficient assumptions regarding the stress distribution along the extrados of an arch. A series of equilibrium equation of soil pressures, in terms of stress resultants, can be written for a given problem. This simplified approach makes it possible to solve the bridge problems by simple statics.

This study indicated that the stress spreading due to live loads has a significant influence in the estimation of the bridge load-carrying capacity. The stress spreading capacity is evaluated by a single parameter, anisotropic ratio  $n$ . Smaller  $n$  brings a greater stress concentration; in contrast, greater  $n$  yields greater stress spreading. In this work, the value of  $n$  was assumed as the multiplier of soil-arch interface and dependent on a simple empirical exponential function. In this respect a natural next step would be to develop a more systematic means of determining suitable anisotropic factor for use in such models.

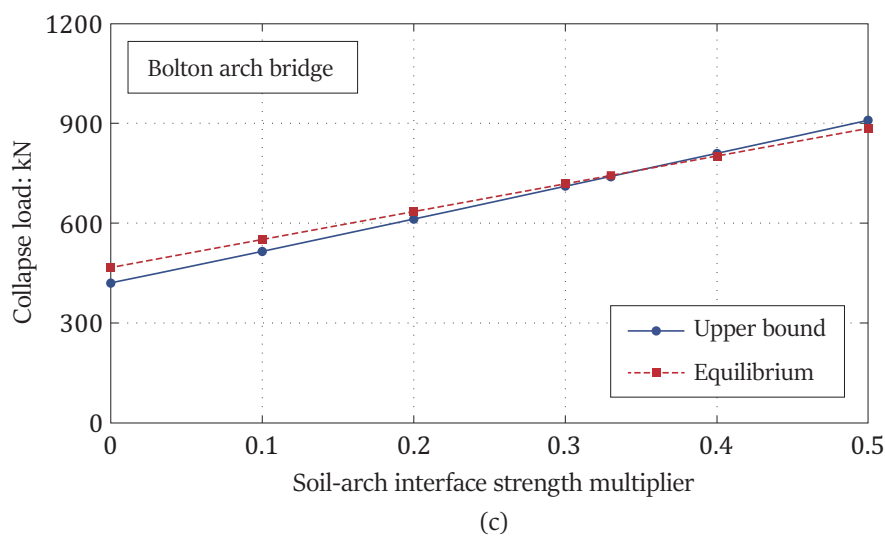
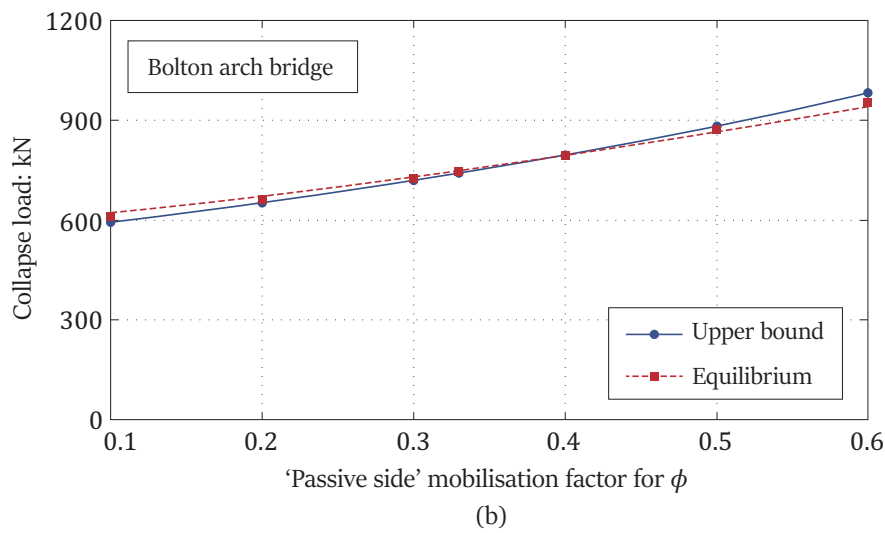
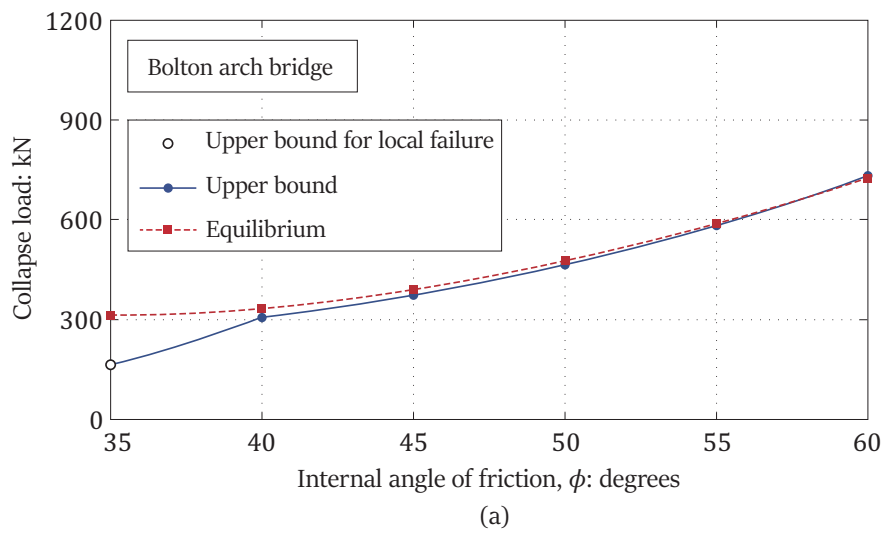
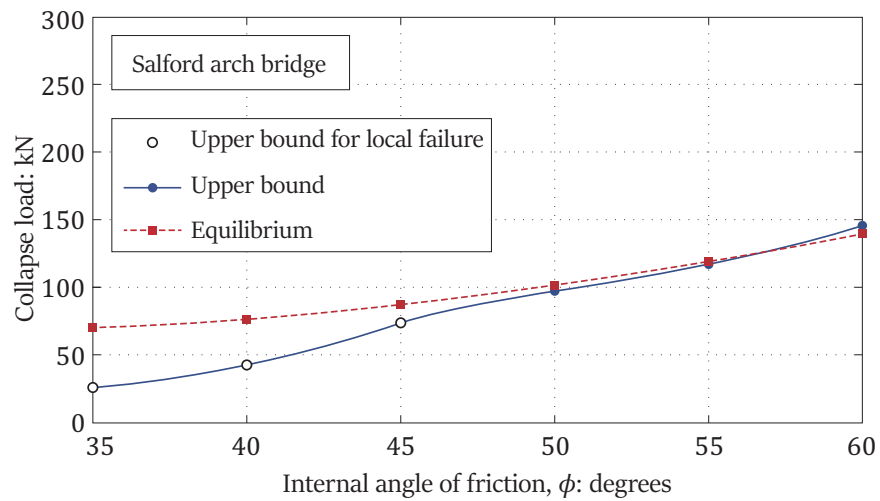
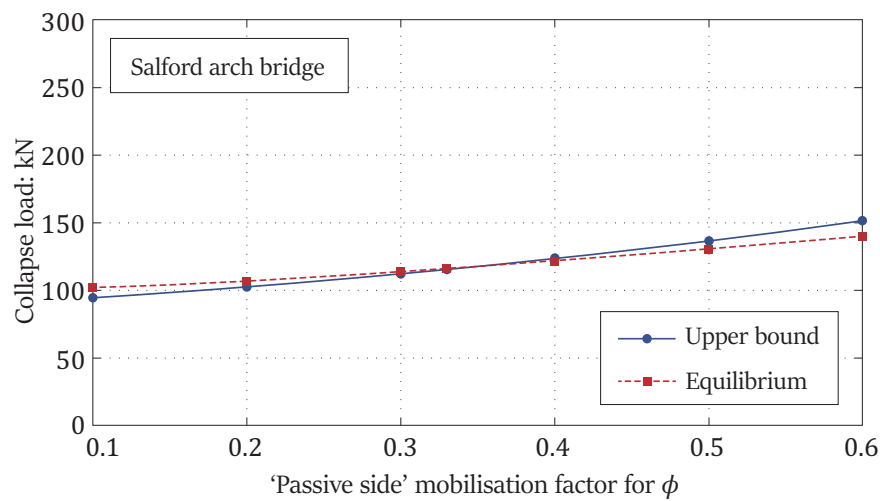


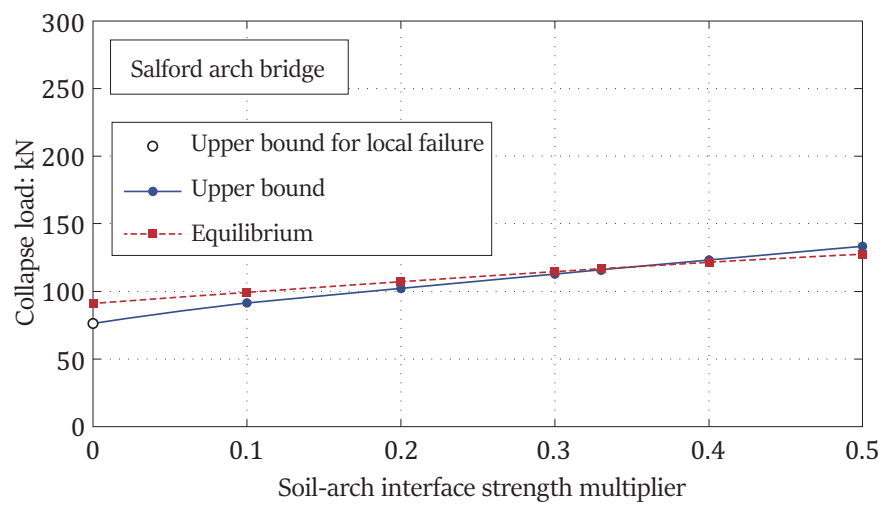
FIGURE 5.16: Parametric study of limit equilibrium solutions for Bolton arch bridge



(a)



(b)



(c)

FIGURE 5.17: Parametric study of limit equilibrium solutions for Salford arch bridge

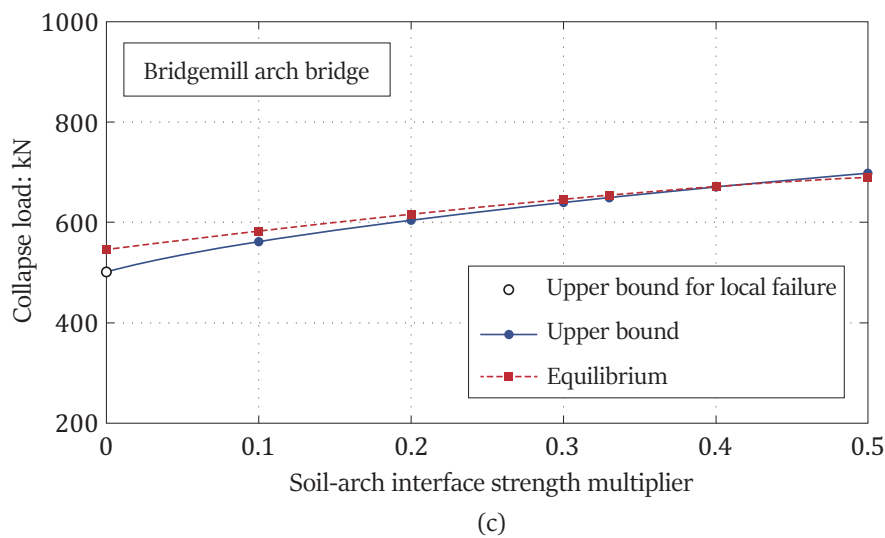
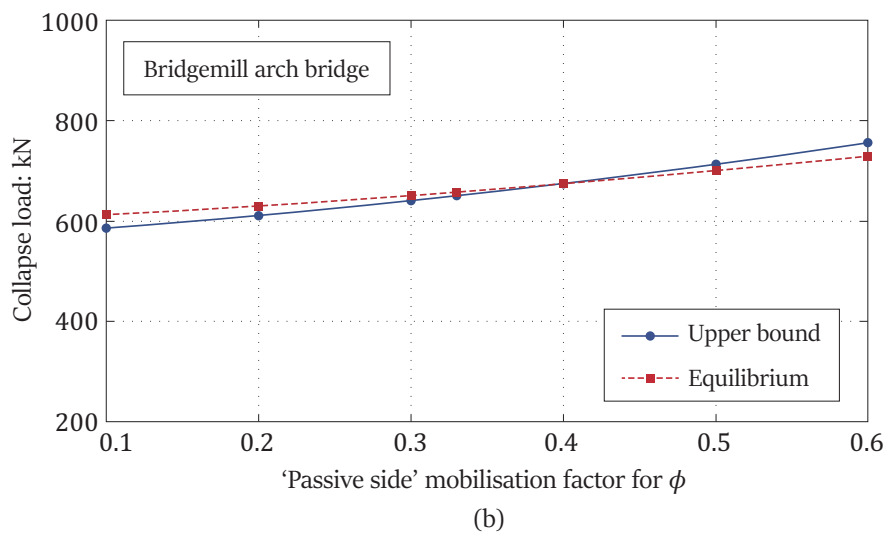
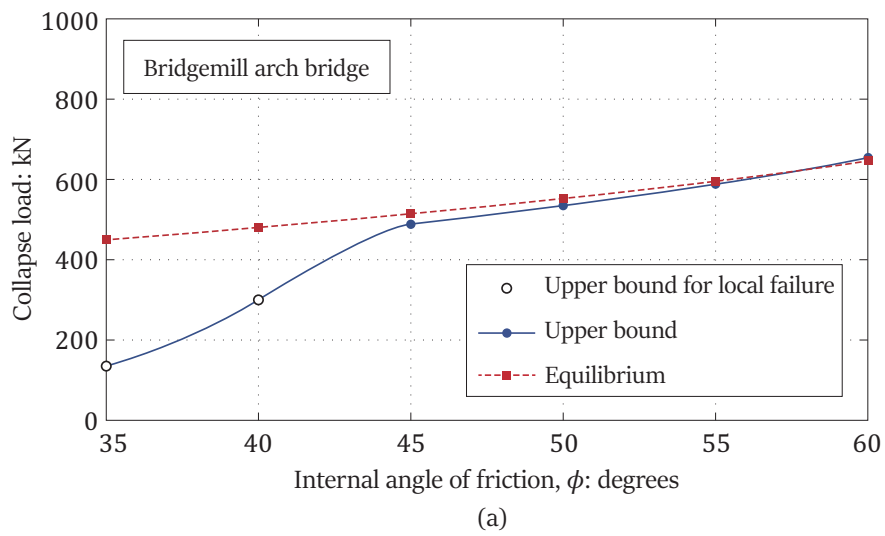


FIGURE 5.18: Parametric study of limit equilibrium solutions for Bridgemill arch bridge

## 5.6 Concluding Remarks

In summary:

- Limit equilibrium analysis provides a conceptually simple and effective means of analyzing the load-carrying capacity of masonry arch bridges. The current version of LimitState:RING allow explicit modelling masonry components to be obtained rapidly, and with a set of input data of soil pressures in the mathematical programming system. The soil arching effect is explicitly considered to derive the earth pressure for both cohesionless and cohesive soil at the stress state. In order to facilitate calculation of earth pressures using the proposed equations, modified active and passive pressure coefficients are provided as functions of the internal frictional angle of soil and the angle of soil-arch interface friction.
- The modelling of soil components also provides stress spreading due to applied loads. The stress spreading capacity can use a single parameter, deformation modulus ratio  $n = E_x/E_z$ , to evaluate. An empirical exponential function is used to determine suitable anisotropic ratio  $n$ , which provides reasonable agreement with results of the discontinuity layout optimisation (DLO) limit analysis procedure when four hinge failures are involved. Both of earth pressures and live load spreading through the fill can be set up into the input data, then utilize the mathematical optimization solvers to obtain results rapidly.

**Part III**

**Discussion**



## Chapter 6

# Discussion

### 6.1 Introduction

The proposed numerical strategies provide powerful methods for assessing the safety of masonry arch bridges. These techniques have now been successfully applied to the analysis of soil-filled masonry arch bridges, using the lower bound, limit equilibrium and upper bound methods. The complex nature of the masonry arch bridges makes modelling them challenging. A number of issues relating to the application of these numerical strategies will be discussed in this chapter.

### 6.2 Issues in Soil Earth Pressures

The challenge is to model soil-arch interaction in masonry arch bridge problems. 'Rankine' earth pressure is assumed in lower-bound stress fields method. Estimation of earth pressure considering arching effect is applied in limit equilibrium method. Both them are simplified in the soil model. In this chapter, DLO model can be used to compare the two simplified soil models.

A masonry arch bridge is designed to show the soil stress distribution on the extrados of the arch barrel. The geometry and main material properties are shown in Figure 6.1 and Table 6.1 respectively. If the load positioned at quarter span of the arch bridges, the critical failure mechanism can be obtained using DLO limit analysis as shown in Figure 6.2. In a case of an arch bridge was acted by a line load over a unit width of bridge. The load carrying capacity of upper bound is equal to 78.45 kN versus 77.87 kN of lower bound solution. The difference between them is very small. It means that the assumption of Rankine earth pressure theory is useful to model the soil-fill. Figure 6.3(a) shows the normal and shear stress distributions on the extrados of an arch barrel. There are four hinges appearing when the arch collapsed. From Figure 6.3(a), it is very clear to see the normal and shear stresses of the lower bound which is good to match the DLO from 'Crown' to 'Hinge 4'. However, the stress distributions of the lower bound can not highly match the DLO in the active side. The reason is that the active arch segment likes the downward open door, rather than the active retaining wall.

TABLE 6.1: Main material parameters of a masonry arch bridge  
(based on Smith *et al.* 2006)

Masonry properties	Values
Crushing strength (N/mm <sup>2</sup> )	25
Coefficient of friction	0.64
Unit weight (kN/m <sup>3</sup> )	23.7
Soil properties	Values
Cohesion, $c$ (kN/m <sup>2</sup> )	0
Internal angle of friction, $\phi$ (degrees)	55
Soil-arch interface strength multiplier	1.0
Unit weight (kN/m <sup>3</sup> )	19.1

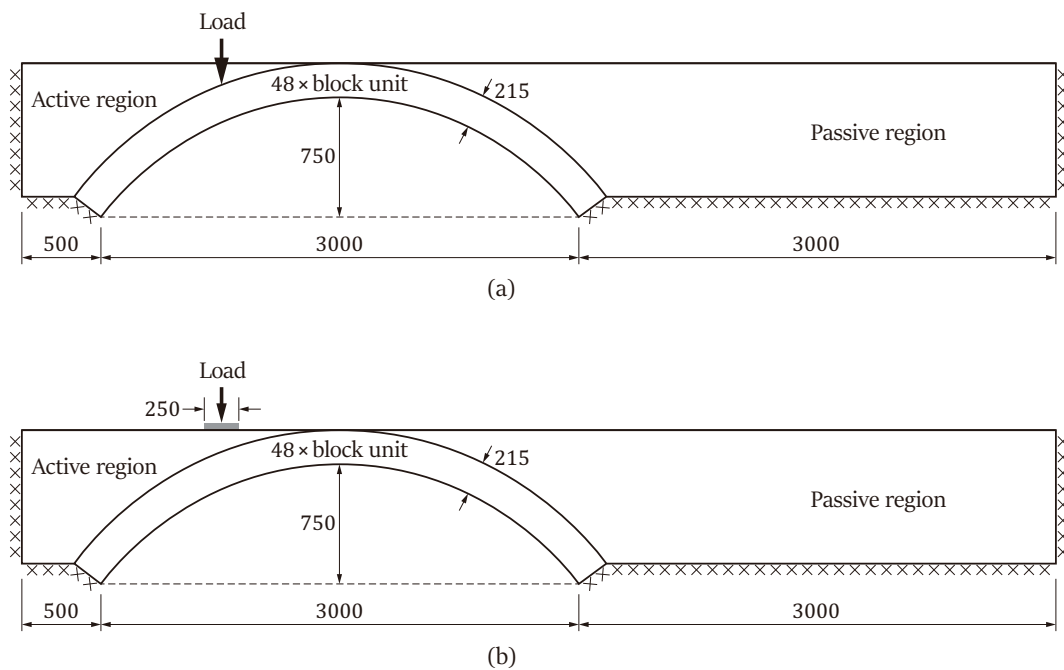


FIGURE 6.1: Geometrical model of a sample of masonry arch bridge with fixed abutments (all dimensions in mm): (a) case of pointed load; (b) case of uniform load

After modelling the simple point load case, it is essential to model the case of an uniform load on the surface of an arch bridge. In the DLO model, the surface height is also assumed on the extrados of the arch crown. Surface backfill weight is acted on the crown surface. An uniform load is applied at the quarter span of the arch and on the crown surface. In the lower bound model, the superimposed soil

pressure is assumed. Soil dead load utilises the Rankine earth pressure theory; Live load through soil-fill utilises the Boussinesq stress theory.

Figure 6.1(b) shows the failure mechanism of a masonry arch under an uniform load. The load carrying capacity of upper bound is equal to 108.6 kN versus 104.08 kN of lower bound solution. The difference between them is very small. It means that the assumption of the superimposed model is useful to this case of the very shallow masonry arch. Figure 7 shows the normal and shear stress distributions on the extrados of an arch barrel. There are four hinges appearing when the arch collapsed. From Figure 6.3(b), it can be seen that the normal stresses of the lower bound which is not very good to match the DLO. From 'Hinge 1' to 'Crown', the stress distributions of DLO have two peaks around the loading centre; the lower bound only has one peak under the loading centre.

Therefore, both 'Rankine' theory and soil model considering arching effect have the issue of simulating soil-arch interaction.

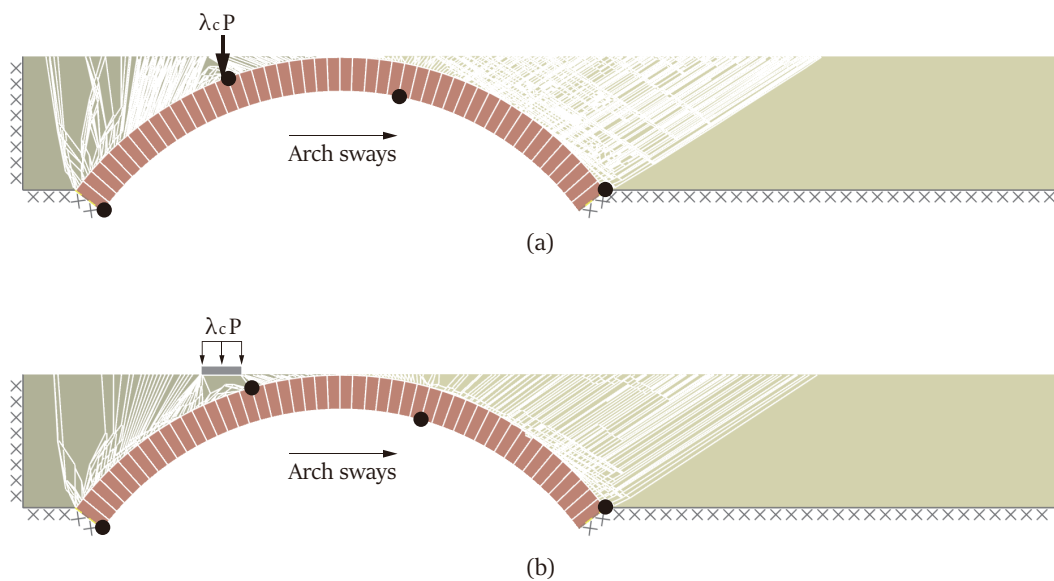
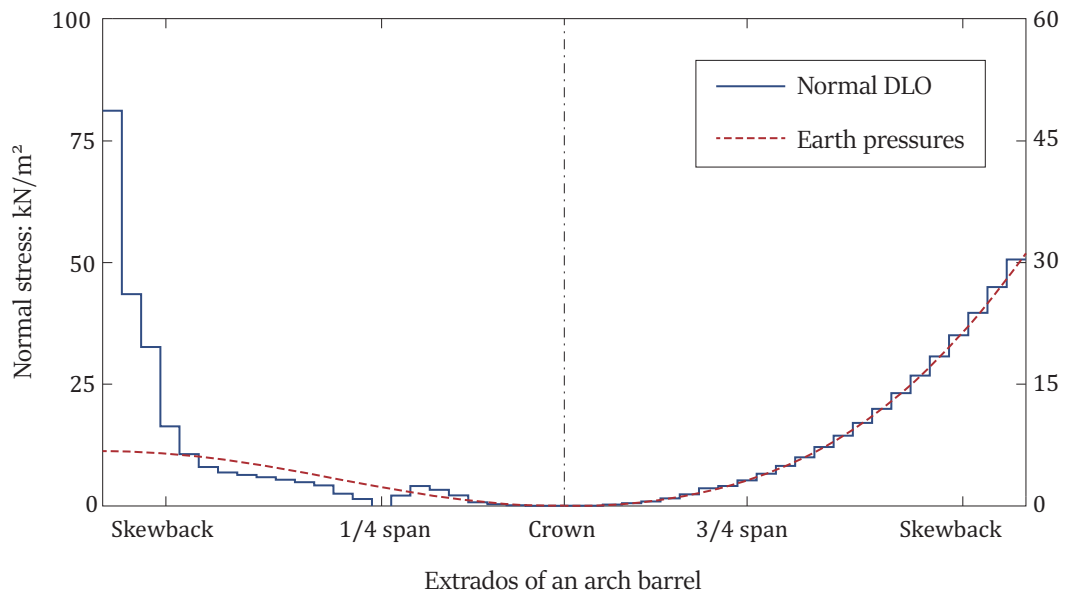


FIGURE 6.2: Failure mechanisms of a sample of masonry arch bridge with fixed abutments (all dimensions in mm): (a) case of pointed load; (b) case of uniform load ( $P$  is a unit load)

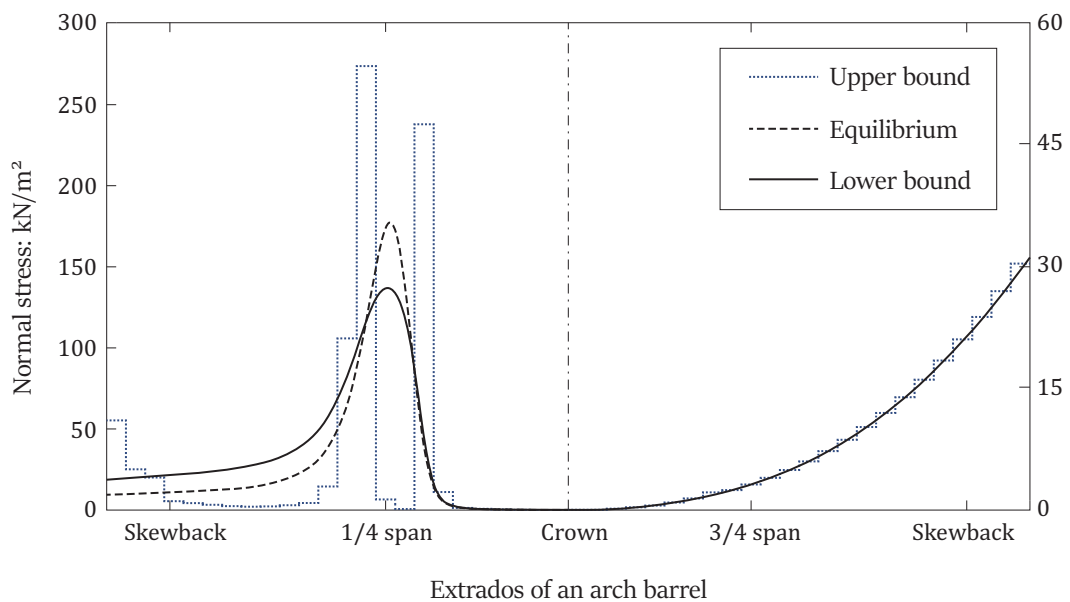
### 6.3 Issues in Complex Masonry Arch Bridge Failure Mechanisms

Four-hinged mechanism is typically failure mode in masonry arch bridges. However, some of other complex failure mechanisms (e.g. 'three-hinged plus sliding') would occur in some situations. In chapter 3 the abutment sliding problem was discussed. DLO-fast method needs adding lines in regions to allow the slip-line may

form. However, using 'Rankine' theory and soil model considering arching effect may not solve the issue in complex masonry arch failure mechanisms because the simple masonry arch bridge with free abutments is difficult to use these methods to model accurately.



(a)



(b)

FIGURE 6.3: Stress distributions on extrados of masonry arch bridge with cohesionless backfill: (a) normal stresses; (b) shear stresses

## **Part IV**

# **Conclusions and Recommendations**



## Chapter 7

# Conclusions and Recommendations

### 7.1 Conclusions

The masonry arch bridge analysis methods developed in the thesis have been designed to provide a rapid computational capability for use in industry. Limit analysis and limit equilibrium methods have been used to furnish methods that are simple, effective and fast. The major research contributions can be summarized as follows:

- To estimate the load-carrying capacity of masonry arches, the upper bound limit analysis technique of discontinuity layout optimization (DLO) has been found to be a simple but efficient means of identifying the critical failure mechanism and associated collapse load. DLO is attractive as it can model both masonry and soil elements directly. The method is now used in industry due to its power and simplicity. However, a problem is that accuracy is dependent upon the number of nodes, and for some problems large numbers of nodes are needed to give good solutions. In this case the associated computational cost is high. This is a particular issue for bridge assessment problems since a large number of load positions need to be considered. To address this a 'DLO-fast' procedure has been proposed; this involves positioning nodes only along the edges of any given body. The procedure has been shown to give results of a given accuracy much more rapidly than when using the standard DLO procedure.
- Although the DLO-fast procedure can reduce the computational cost, the associated computational cost remains much higher than for LimitState:RING, which uses rigid-block analysis to estimate the load-carrying capacity of masonry arch bridges. Thus there is merit in enhancing LimitState:RING, which is already widely used in industry. Currently LimitState:RING uses highly simplified soil-arch interaction assumptions, considering dispersal of the applied load, self-weight and passive restraint of the backfill material surrounding the arch barrel. In addition, the current version of the software assumes

that the load dispersal distribution can be approximated using vertical Boussinesq stresses, with horizontal and shear stresses neglected. In accordance with lower-bound theorem, vertical, horizontal and shear stresses should also be considered. Incorporating the proposed stress fields into LimitState:RING, would enable the software to furnish true ('safe') lower-bound solutions at minimal computational cost.

- The lower-bound stress fields method proposed for use in LimitState:RING requires a number of iterations to find the optimal stress field. According to the lower-bound theorem, an admissible stress field must not be violated at any point in the solid body. In order to find a better lower bound solution, an optimal anisotropic factor needs to be obtained via iteration. Considering the need for two iterative steps, an alternative is to devise a simple but efficient limit equilibrium formulation. This has therefore been done. In the limit equilibrium soil model developed arching effects are considered, which provide a suitably realistic model of soil-arch interaction. A vertical anisotropic stress distribution is used to model dispersal of the applied load. Benefits of the method developed are that, if implemented, it would have a negligible effect on the run time of LimitState:RING.

## 7.2 Recommendations of Future Work

Areas for further work are indicated below:

- It has been shown that the accuracy of the solutions obtained using the DLO-fast procedure are lower when complex masonry arch bridge failure mechanisms are involved (e.g. abutment sliding mechanisms). Although in this thesis steps have been taken to address this (e.g. adding lines in regions where slip-lines may form), these may not always be effective. There is therefore the potential to address the issue of complex failure mechanisms issue more rigorously, with less, or even no, impact on the quality of the solutions.
- In this thesis, efforts have been made to develop the lower bound stress fields method. However, as discussed earlier, the iterations needed to check for yield and to find improved lower-bound solutions has scope for improvement. Although the limit equilibrium method considers arching effects, passive lateral earth pressures on the extrados of an arch bridge give rise to very high stresses around an abutment. This is due to an imperfection in the applicable mathematical equation, which could be improved.
- The efficacy of the rigid-block analysis method when applied to 2D problems has been demonstrated in this thesis. However, to make the software more powerful for use in industry, real-world 3D masonry arch bridges geometries

should be able to be considered, particularly in the case of skew bridges. This will be of interest to many engineers working in industry.



# References

- Amodio, S., Gilbert, M. & Smith, C. C. (2019), 'Modelling masonry arch bridges containing internal spandrel walls', *Proceedings of the 9th International Conference on Arch Bridges, Porto* pp. 315–322.
- Barden, L. (1962), 'Distribution of contact pressure under foundations', *Géotechnique* **12**(3), 181–198.
- Barden, L. (1963), 'Stresses and displacements in a cross-anisotropic soil', *Géotechnique* **13**(3), 198–210.
- Block, P. (2009), Thrust network analysis: exploring three-dimensional equilibrium, PhD thesis, Massachusetts Institute of Technology.
- Block, P., Ciblac, T. & Ochsendorf, J. (2006), 'Real-time limit analysis of vaulted masonry buildings', *Computers & structures* **84**(29-30), 1841–1852.
- Bolton, M. (1992), 'Codes standards and design guides in retaining structures', *Thomas Telford* **387**, 402.
- Bolton, M. D. (1979), *A guide to soil mechanics*, Universities Press.
- Boussinesq, J. (1877), *Essai sur la théorie des eaux courantes*, Impr. nationale.
- Brencich, A. & De Francesco, U. (2004), 'Assessment of multispan masonry arch bridges. i: Simplified approach', *Journal of Bridge Engineering* **9**(6), 582–590.
- Brencich, A., De Francesco, U. & Gambarotta, L. (2001), 'Elastic no tensile resistant-plastic analysis of masonry arch bridges as an extension of castigliano's method', *Proc. 9th Can. Mas. Symp.*
- BrightonWorks (2020), 'Old photos of london road viaduct'.  
**URL:** <http://www.brightonlocoworks.co.uk/london-road-viaduct-old-photos.php>
- Bruce, G. (1851), 'Description of the royal border bridge over the river tweed, on the york, newcastle and berwick railway. (includes plate and appendix)', *Minutes of the Proceedings of the Institution of Civil Engineers* **10**(1851), 219–233.
- Callaway, P., Gilbert, M. & Smith, C. C. (2012), 'Influence of backfill on the capacity of masonry arch bridges', *Proceedings of the ICE-Bridge Engineering* **165**(3), 147–158.
- Castigliano, A. (1966), *The theory of equilibrium of elastic systems and its applications*, Dover Publications.

- Cavicchi, A. & Gambarotta, L. (2005), 'Collapse analysis of masonry bridges taking into account arch–fill interaction', *Engineering Structures* **27**(4), 605–615.
- Cavicchi, A. & Gambarotta, L. (2007), 'Lower bound limit analysis of masonry bridges including arch–fill interaction', *Engineering Structures* **29**(11), 3002–3014.
- Chen, W. (1975), *Limit analysis and soil plasticity*, Elsevier.
- Choo, B., Coutie, M. & Gong, N. (1991), 'Finite-element analysis of masonry arch bridges using tapered elements', *Proceedings of the Institution of Civil Engineers* **91**(4), 755–770.
- Coulomb, C. (1773), 'Essai sur une application des regles de maximis et minimis a quelques problemes de statique relatifs a l'architecture (essay on maximums and minimums of rules to some static problems relating to architecture)'.
- Crisfield, M. A. (1993), *Non-linear finite element analysis of solids and structures*, Vol. 1, Wiley New York.
- Crisfield, M. A. & Packham, A. (1987), 'A mechanism program for computing the strength of masonry arch bridges', *TRRL Research Report* (124).
- Cundall, P. & Strack, O. (1979), 'A discrete numerical model for granular assemblies', *Géotechnique* **29**(1), 47–65.
- Dang, Q., Gilbert, M. & Smith, C. (2019), 'Lower bound stress fields in the limit analysis of soil-filled masonry arch bridges', *Proceedings of the 9th International Conference on Arch Bridges, Porto* pp. 323–330.
- Fang, Y., Chen, T. & Wu, B. (1994), 'Passive earth pressures with various wall movements', *Journal of Geotechnical Engineering* **120**(8), 1307–1323.
- Fang, Y. & Ishibashi, I. (1986), 'Static earth pressures with various wall movements', *Journal of Geotechnical Engineering* **112**(3), 317–333.
- Fang, Y. S., Ho, Y. C. & Chen, T. J. (2002), 'Passive earth pressure with critical state concept', *Journal of Geotechnical and Geoenvironmental Engineering* **128**(8), 651–659.
- Gilbert, M. (2001), 'Ring: a 2d rigid-block analysis program for masonry arch bridges', pp. 459–464.
- Gilbert, M. (2007), 'Limit analysis applied to masonry arch bridges: state-of-the-art and recent developments', *Proceedings of the 5th International Conference on Arch Bridges', Madeira* pp. 13–28.
- Gilbert, M. & Melbourne, C. (1994), 'Rigid-block analysis of masonry structures', *The Structural Engineer* **72**(21), 187–202.

- Gilbert, M., Nguyen, D. P. & Smith, C. C. (2007), 'Computational limit analysis of soil-arch interaction in masonry arch bridges', *Proceedings of the 5th International Conference on Arch Bridges, Madeira* 7, 633–640.
- Gilbert, M., Smith, C. C. & Pritchard, T. J. (2010), 'Masonry arch analysis using discontinuity layout optimisation', *Proceedings of the Institution of Civil Engineers-Engineering and Computational Mechanics* 163(3), 155–166.
- Gilbert, M., Valentino, J., Smith, C. & Pritchard, T. (2019), 'Limit analysis of masonry arch bridges using discontinuity layout optimization', *Proceedings of the 9th International Conference on Arch Bridges, Porto* pp. 307–314.
- Handy, R. (1985), 'The arch in soil arching', *Journal of Geotechnical Engineering* 111(3), 302–318.
- Harvey, W. J. (1988), 'Application of the mechanism analysis to masonry arches.', *Struct. Eng. A* 66(5), 77.
- Hendry, A., Davies, S. & Royles, R. (1985), 'Test on stone masonry arch at bridgemill-girvan'.
- Heyman, J. (1982), *The Masonry Arch*.
- Hulet, K., Smith, C. & Gilbert, M. (2006), 'Load-carrying capacity of flooded masonry arch bridges', *Proceedings of the Institution of Civil Engineers-Bridge Engineering* 159(3), 97–103.
- Janssen, H. A. (1895), 'Versuche uber getreidedruck in silozellen', *Z. Ver. Dtsch. Ing.* 39(35), 1045–1049.
- Kooharian, A. (1952), 'Limit analysis of voussoir (segmental) and concrete arches', *Journal Proceedings* 49(12), 317–328.
- Lambe, T. & Whitman, R. (1979), *Soil Mechanics SI Version*, New York, Wiley.
- LimitState (2019a), 'Limitstate:geo manual, version 3.5 edition'.  
URL: <http://www.limitstate.com/geo>
- LimitState (2019b), 'Limitstate:ring manual, version 3.2 edition'.  
URL: <http://www.limitstate.com/ring>
- Livesley, R. K. (1978), 'Limit analysis of structures formed from rigid blocks', *International Journal for Numerical Methods in Engineering* 12(12), 1853–1871.
- Livesley, R. K. (1992), 'The collapse analysis of masonry arch bridges', 4, 261–274.
- Melbourne, C. & Gilbert, M. (1995), 'The behaviour of multiring brickwork arch bridges', *The Structural Engineer* 73(3), 39–47.

- Melbourne, C., Gilbert, M. & Wagstaff, M. (1997), 'The collapse behaviour of multi-span brickwork arch bridges', *Structural Engineer* **75**(17).
- Melbourne, C., McKibbins, L., Sawar, N. & Sicilia Gaillard, C. (2006), 'Masonry arch bridges: condition appraisal and remedial treatment', *CIRIA, London*.
- Moroto, N. (1973), 'Anisotropy and stress distribution in sand', *Proceedings of the Japan Society of Civil Engineers* **1973**(212), 121–129.
- Moroto, N. & Hasegawa, A. (1990), 'Anisotropic elastic stress formulae applicable to reinforced earth', *Soils and foundations* **30**(1), 172–178.
- Ni, P., Mangalathu, S., Song, L., Mei, G. & Zhao, Y. (2018), 'Displacement-dependent lateral earth pressure models', *Journal of Engineering Mechanics* **144**(6).
- Niedostatkiewicz, M., Lesniewska, D. & Tejchman, J. (2011), 'Experimental analysis of shear zone patterns in cohesionless for earth pressure problems using particle image velocimetry', *Strain* **47**, 218–231.
- Obvis (2016), 'Archiem manual, version 2.5.1 edition'.  
**URL:** <http://www.obvis.com>
- Ochsendorf, J. (2006), 'Masonry arch on spreading supports', *Structural Engineer* **84**(2), 29–34.
- O'Dwyer, D. (1999), 'Funicular analysis of masonry vaults', *Computers & Structures* **73**(1-5), 187–197.
- Page, J. (1993), *Masonry arch bridges*, HM Stationery Office London, UK.
- Paik, K. & Salgado, R. (2003), 'Estimation of active earth pressure against rigid retaining walls considering arching effects', *Géotechnique* **53**(7), 643–653.
- Pippard, A. & Chitty, L. (1951), *A study of the voussoir arch*, HM Stationery Office.
- Pippard, A. J. S. (1948), 'The approximate estimation of safe loads on masonry bridges', *The civil engineer in war: A symposium of papers on war-time engineering problems* pp. 1–365.
- Poleni, G. & Poleni, J. (1748), *Memorie istoriche della gran cupola del tempio Vaticano e de'danni di essa e detristoramenti loro, divisi in libri 5*, Nella Stamperia del seminario.
- Pytlos, M. (2015), *New tools for modelling soil-filled masonry arch bridges*, PhD thesis, University of Sheffield.
- Rankine, W. J. M. (1857), 'On the stability of loose earth', *Philosophical transactions of the Royal Society of London* **147**, 9–27.
- Sarhosis, V., De Santis, S. & De Felice, G. (2016), 'A review of experimental investigations and assessment methods for masonry arch bridges', *Structure and Infrastructure Engineering* **12**(11), 1439–1464.

- Smith, C. C. & Gilbert, M. (2007), 'Application of discontinuity layout optimization to plane plasticity problems', *Proceedings of the Royal Society A: Mathematical, Physical and Engineering Sciences* **463**(2086), 2461–2484.
- Smith, C., Gilbert, M., Melbourne, C. & Wang, J. (2006), 'Full scale modelling of soil-structure interaction in masonry arch bridges', *Proceedings of the 6th International Conference of Physical Modelling in Geotechnics, Hong Kong* pp. 247–252.
- Stevin, S. (1973), *De beghinselen der weeghconst*, Inde druckerye van Christoffel Plantijn, by François van Raphelinghen.
- Terzaghi, K. (1936), 'Stress distribution in dry and in saturated sand above a yielding trap-door', *International Conference on Soil Mechanics Proceedings* **1**, 307–311.
- Terzaghi, K. (1943), 'Theoretical soil mechanics', *New York, McGraw Hill* pp. 11–15.
- Wang, J. & Melbourne, C. (2010), 'Mechanics of mexe method for masonry arch bridge assessment', *Proceedings of the Institution of Civil Engineers-Engineering and Computational Mechanics* **163**(3), 187–202.



# Appendices



## Appendix A

# Formulations in Rigid-Block Limit Analysis

### A.1 Joint Equilibrium Formulation

A joint equilibrium formulation is used in rigid-block limit analysis for estimating the load-carrying capacity of masonry arch bridges. Because an arch barrel is built by a series of very-stiff voussoirs, in the limit state a masonry structure can be assumed as a rigid block assemblage. Therefore, a joint equilibrium formulation for the rigid-block analysis, perfectly plastic body discretized using  $b$  blocks,  $c$  contacts and a single load case can be stated as follows

$$\max \lambda \quad (\text{A.1})$$

subject to equilibrium constraints:

$$\mathbf{B} \cdot \mathbf{q} - \lambda \cdot \mathbf{f}_L = \mathbf{f}_D \quad (\text{A.2})$$

and no-tension yield constraints (e.g. for each contact,  $i = 1, \dots, c$ ):

$$\begin{cases} M_i \leq 0.5 t_i N_i \\ M_i \geq -0.5 t_i N_i \end{cases} \quad (\text{A.3})$$

and sliding yield constraints (e.g. for each contact,  $i = 1, \dots, c$ ):

$$\begin{cases} S_i \leq \mu N_i \\ S_i \geq -\mu N_i \end{cases} \quad (\text{A.4})$$

where  $\lambda$  is the load factor;  $\mathbf{B}$  is a suitable ( $3b \times 3c$ ) equilibrium matrix; and  $\mathbf{q}$  is a vector of shear and normal forces and moment acting on contacts, i.e.  $\mathbf{q}^T = \{S_1, N_1, M_1, S_2, N_2, M_2, \dots, M_c\}$ , where  $S_i$  and  $N_i$  and  $M_i$  represent, respectively,

the shear and the normal force and the moment acting on contact  $i$  ( $i = 1, \dots, c$ ).  $\mathbf{f}_D^T = \{f_{D1}^x, f_{D1}^y, f_{D1}^\omega, \dots, f_{Dc}^\omega\}$  and  $\mathbf{f}_L^T = \{f_{L1}^x, f_{L1}^y, f_{L1}^\omega, \dots, f_{Lb}^\omega\}$ ; and  $f_{Dj}^x, f_{Dj}^y, f_{Dj}^\omega$  and  $f_{Lj}^x, f_{Lj}^y, f_{Lj}^\omega$  present, respectively, the horizontal and vertical and moment dead and live loads applied locally at block  $j$  ( $j = 1, \dots, b$ ). Thus, the linear programming (LP) variables are  $S_i$  and  $N_i$  and  $M_i$  (e.g.  $N_i \geq 0$ ,  $S_i$  and  $M_i$  are unrestricted variables), and the live load factor  $\lambda$ . The objective is therefore to maximize  $\lambda$  while ensuring that the yield condition is not violated along any contacts.

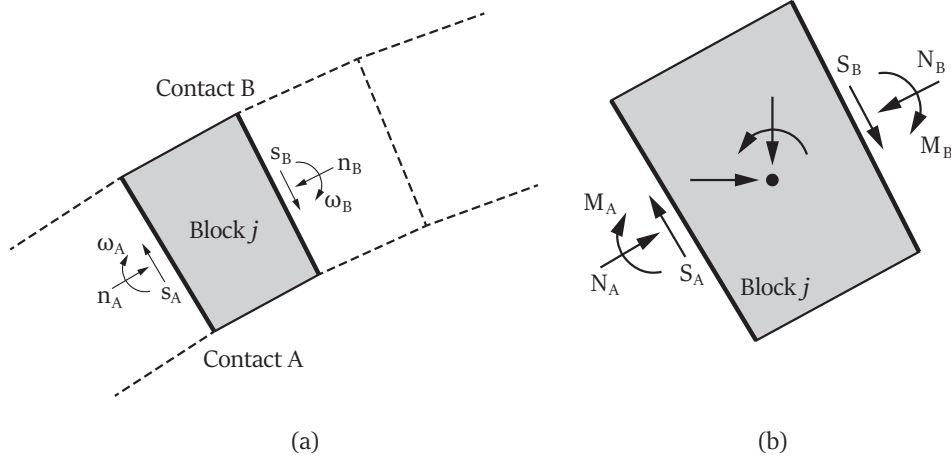


FIGURE A.1: Block and contact forces: (a) the discretization of blocks; (b) force vectors of a block and its contacts

Alternatively, the required equilibrium constraint can be written for a block  $j$  as follows (Figure A.1)

$$\mathbf{B}_j \cdot \mathbf{q}_j - \lambda \cdot \mathbf{f}_{Lj} = \mathbf{f}_{Dj} \quad (\text{A.5})$$

or in expanded form as

$$\begin{bmatrix} \mathbf{s}_A & \mathbf{n}_A & \mathbf{m}_A & \mathbf{0} & \mathbf{0} & \mathbf{0} \\ \mathbf{0} & \mathbf{0} & \mathbf{0} & \mathbf{s}_B & \mathbf{n}_B & \mathbf{m}_B \end{bmatrix} \begin{bmatrix} S_A \\ N_A \\ M_A \\ S_B \\ N_B \\ M_B \end{bmatrix} - \lambda \begin{bmatrix} f_{Lj}^x \\ f_{Lj}^y \\ f_{Lj}^\omega \end{bmatrix} = \begin{bmatrix} f_{Dj}^x \\ f_{Dj}^y \\ f_{Dj}^\omega \end{bmatrix} \quad (\text{A.6})$$

where  $\mathbf{s}_A$ ,  $\mathbf{n}_A$  and  $\mathbf{m}_A$  are vectors of the shear and normal and rotational forces at contact A, respectively;  $\mathbf{s}_B$ ,  $\mathbf{n}_B$  and  $\mathbf{m}_B$  are vectors of the horizontal and vertical forces and moments at contact B, respectively.

## A.2 Including Finite Masonry Material Strength

The yield constraints (equation A.3) given in Appendix A.1 are valid only, if the material is infinitely strong in compression. If it is assumed that the masonry possesses finite masonry strength and that the thrust is transmitted through a rectangular crush block, then equation A.3 can be replaced with

$$\begin{cases} M_i \leq N_i \left( 0.5t_i - \frac{N_i}{2\sigma_{\text{crush}}b} \right) \\ M_i \geq -N_i \left( 0.5t_i - \frac{N_i}{2\sigma_{\text{crush}}b} \right) \end{cases} \quad (\text{A.7})$$

where  $\sigma_{\text{crush}}$  is the crushed compressive strength of the masonry material;  $b$  is the width of the masonry arch ring.

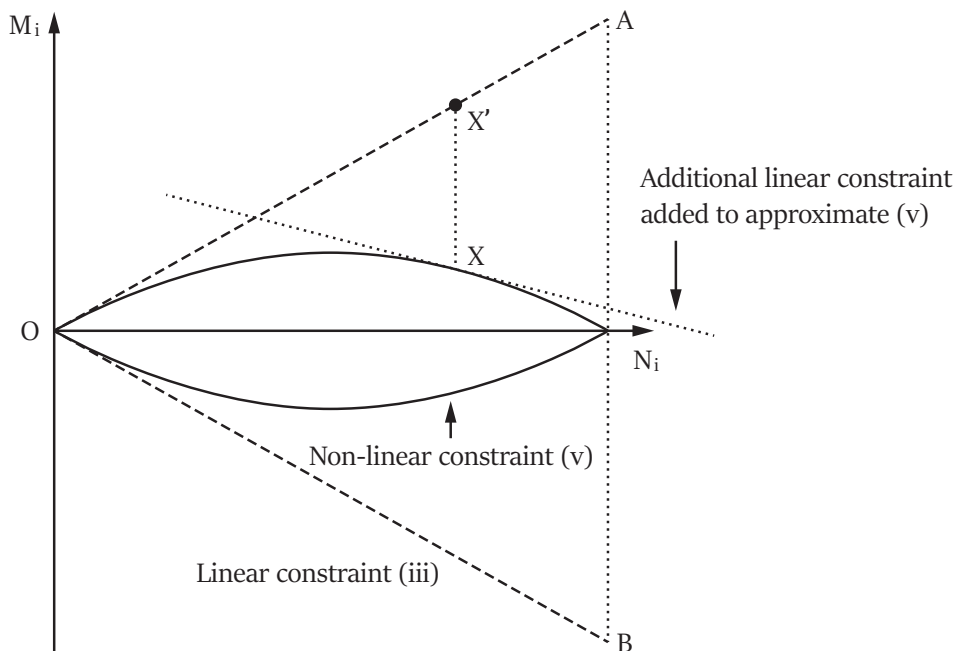


FIGURE A.2: Contact surface moment vs. normal force failure envelopes (LimitState 2019b)

However, the constraints in equation A.7 are non-linear (Figure A.2). Therefore if a linear programming (LP) solver is still to be used to obtain a solution to the global problem, then these constraints need to be approximated as a series of linear constraints. In order to minimise the number of constraints in the problem (and to maximise computational efficiency) an iterative solution algorithm which involves only refining the representation of the failure envelope where required is used:



For case B, the force equilibrium along the AB and normal AB can be expressed as

$$\begin{cases} \sigma_v dx \cos \theta + \sigma_h dz \sin \theta = \sigma_{n,sw} dl \\ \sigma_h dx \sin \theta - \sigma_v dz \cos \theta = \tau_{sw} dl \end{cases} \quad (\text{A.10})$$

Then the normal and shear stresses due to backfill self-weight are derived as

$$\begin{cases} \sigma_{n,sw} = \sigma_v \cos^2 \theta + \sigma_h \sin^2 \theta \\ \tau_{sw} = \sigma_v \sin \theta \cos \theta - \sigma_h \sin \theta \cos \theta \end{cases} \quad (\text{A.11})$$

and

$$\begin{cases} \sigma_{n,sw} = \sigma_v \cos^2 \theta + \sigma_h \sin^2 \theta \\ \tau_{sw} = \sigma_h \sin \theta \cos \theta - \sigma_v \sin \theta \cos \theta \end{cases} \quad (\text{A.12})$$

Consider the soil-arch interface yield constraint of  $\tau_{sw} \leq \sigma_{sw} \tan \delta + c_w$ , then

$$\begin{cases} \sigma_v \sin \theta \cos \theta - \sigma_h \sin \theta \cos \theta \leq (\sigma_v \cos^2 \theta + \sigma_h \sin^2 \theta) \tan \delta + c_w \\ \sigma_h \sin \theta \cos \theta - \sigma_v \sin \theta \cos \theta \leq (\sigma_v \cos^2 \theta + \sigma_h \sin^2 \theta) \tan \delta + c_w \end{cases}$$

and then

$$\begin{cases} \sigma_v (\sin \theta \cos \theta - \cos^2 \theta \tan \delta) - c_w \leq \sigma_h (\sin \theta \cos \theta + \sin^2 \theta \tan \delta) \\ \sigma_h (\sin \theta \cos \theta - \sin^2 \theta \tan \delta) \leq \sigma_v (\sin \theta \cos \theta + \cos^2 \theta \tan \delta) + c_w \end{cases} \quad (\text{A.13})$$

Consider the limiting horizontal fill stresses  $\sigma_{h,min}$  and  $\sigma_{h,max}$ , then the equation (A.13) can be rewritten as

$$\begin{cases} \sigma_{h,min} = \frac{\sigma_v (\sin \theta \cos \theta - \cos^2 \theta \tan \delta) - c_w}{(\sin \theta \cos \theta + \sin^2 \theta \tan \delta)} \\ \sigma_{h,max} = \frac{\sigma_v (\sin \theta \cos \theta + \cos^2 \theta \tan \delta) + c_w}{(\sin \theta \cos \theta - \sin^2 \theta \tan \delta)} \end{cases} \quad (\text{A.14})$$



## Appendix B

# Formulations in Discontinuity Layout Optimization

### B.1 Primal Problem

The contribution of each potential discontinuity  $i$  to the local compatibility constraint equation can be written as follows

$$\mathbf{B}_i \mathbf{d}_i = \mathbf{u}_i \quad (\text{B.1})$$

where  $\mathbf{B}_i$ ,  $\mathbf{d}_i$  and  $\mathbf{u}_i$  are the local compatibility matrix, discontinuity and nodal displacement vectors, respectively. Now consider a cohesive-frictional material governed by the Mohr–Coulomb failure criteria. In this case, the associated flow rule can be written for discontinuity  $i$  as

$$\begin{bmatrix} \alpha_i - \beta_i \tan \phi_i & -\alpha_i - \beta_i \tan \phi_i & 0.5l_i\beta_i & -0.5l_i\beta_i \\ \beta_i + \alpha_i \tan \phi_i & -\beta_i + \alpha_i \tan \phi_i & -0.5l_i\alpha_i & 0.5l_i\alpha_i \\ 0 & 0 & 1 & -1 \\ -\alpha_i + \beta_i \tan \phi_i & \alpha_i + \beta_i \tan \phi_i & 0.5l_i\beta_i & -0.5l_i\beta_i \\ -\beta_i - \alpha_i \tan \phi_i & \beta_i - \alpha_i \tan \phi_i & -0.5l_i\alpha_i & 0.5l_i\alpha_i \\ 0 & 0 & -1 & 1 \end{bmatrix} \begin{bmatrix} s_i^+ \\ s_i^- \\ \omega_i^+ \\ \omega_i^- \end{bmatrix} = \begin{bmatrix} u_{Ai}^x \\ u_{Ai}^y \\ u_{Ai}^\omega \\ u_{Bi}^x \\ u_{Bi}^y \\ u_{Bi}^\omega \end{bmatrix} \quad (\text{B.2})$$

where  $\alpha_i$  and  $\beta_i$  are the  $x$ -axis and  $y$ -axis direction cosines for discontinuity  $i$ , connecting nodes A and B. Figure B.1 shows that the shear and rotational and normal displacement along a discontinuity  $i$ . The actual shear displacement at the discontinuity is  $s_i = s_i^+ - s_i^-$ ; and the actual rotational displacement at the discontinuity is  $\omega_i = \omega_i^+ - \omega_i^-$ . The associated flow rule can be written for the discontinuity as

$$n_i = (s_i^+ + s_i^-) \tan \phi_i + (\omega_i^+ + \omega_i^-) u_i l_i \quad (\text{B.3})$$

where  $\phi_i$  is the frictional angle and  $n_i$  is the normal displacement accompanying the sliding. In the equation B.4, when rotations are focused within an adjacent yielding region,  $u_i$  is expressed as

$$u_i = 0.5 - \frac{1}{1 + e^{\pi \tan \phi_i}} \quad (\text{B.4})$$

Alternatively, if rotations can occur only at the boundary,  $u_i$  is taken as 0.5 (Gilbert *et al.* 2010).

or in expanded form as

$$\mathbf{B}_i \mathbf{d}_i = \begin{bmatrix} \alpha_i & -\beta_i & 0.5l_i\beta_i \\ \beta_i & \alpha_i & -0.5l_i\alpha_i \\ 0 & 0 & 1 \\ -\alpha_i & \beta_i & 0.5l_i\beta_i \\ -\beta_i & -\alpha_i & -0.5l_i\alpha_i \\ 0 & 0 & -1 \end{bmatrix} \begin{bmatrix} s_i \\ n_i \\ \omega_i \end{bmatrix} = \begin{bmatrix} u_{Ai}^x \\ u_{Ai}^y \\ u_{Ai}^\omega \\ u_{Bi}^x \\ u_{Bi}^y \\ u_{Bi}^\omega \end{bmatrix} \quad (\text{B.5})$$

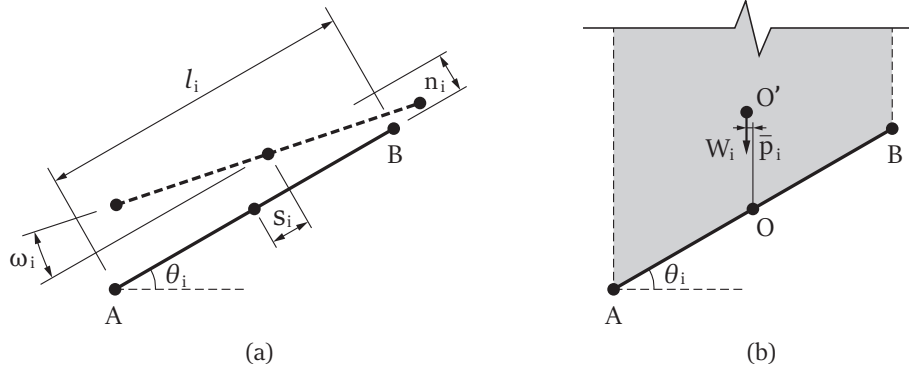


FIGURE B.1: Discontinuity relative displacements: (a) translational and rotational displacements; (b) strip of material lying vertically above a discontinuity

In order to present a more generally applicable limit analysis formulation, with new linear programming (LP) variables and with compatibility and flow constraints decoupled. Now using LP variables  $s_i$ ,  $n_i$  and  $\omega_i$  in  $\mathbf{d}_i$ , to present the shear and normal and rotational displacement at discontinuity  $i$ , respectively, the local compatibility constraint becomes

Then, the flow rule is enforced by introducing the following constraint

$$\mathbf{N}_i \mathbf{p}_i - \mathbf{d}_i = \begin{bmatrix} 1 & -1 & 0 & 0 \\ \tan \phi_i & \tan \phi_i & u_i l_i & u_i l_i \\ 0 & 0 & 1 & -1 \end{bmatrix} \begin{bmatrix} p_i^1 \\ p_i^2 \\ p_i^3 \\ p_i^4 \end{bmatrix} - \begin{bmatrix} s_i \\ n_i \\ \omega_i \end{bmatrix} = \mathbf{0} \quad (\text{B.6})$$

where  $\mathbf{N}_i$  is a local plastic flow matrix;  $\mathbf{p}_i$  is a vector containing plastic multipliers plastic multiplier variables  $p_i^1, p_i^2, p_i^3, p_i^4$ , where  $p_i^1, p_i^2, p_i^3, p_i^4 \geq 0$ .

In the LP problem, the objective is to minimize the work done by the external live loads. In many problems, dead loads (including body forces) and energy dissipation are present to the work balance equation. Thus, the work balance equation can be written as follows

$$\lambda \mathbf{f}_L^T \mathbf{d} = -\mathbf{f}_D^T \mathbf{d} + \mathbf{g}^T \mathbf{p} \quad (\text{B.7})$$

where  $\lambda$  is the load factor;  $\mathbf{f}_D^T = \{f_{D1}^s, f_{D1}^n, f_{D1}^\omega, \dots, f_{Dm}^\omega\}$  and  $\mathbf{f}_L^T = \{f_{L1}^s, f_{L1}^n, f_{L1}^\omega, \dots, f_{Lm}^\omega\}$ ; and  $f_{Di}^s, f_{Di}^n, f_{Di}^\omega$  and  $f_{Li}^s, f_{Li}^n, f_{Li}^\omega$  present, respectively, the shear and normal and moment dead and live loads applied locally at discontinuity  $i$  ( $i = 1, \dots, m$ ).

It is convenient to distinguish between loads applied at external boundaries and those applied within a body itself. The contribution made by discontinuity  $i$  to the  $\mathbf{f}_D^T \mathbf{d}$  term in equation can be written as follows

$$\mathbf{f}_{Di}^T \mathbf{d}_i = \begin{bmatrix} -W_i \beta_i & -W_i \alpha_i & -W_i \bar{p}_i \end{bmatrix} \begin{bmatrix} s_i \\ n_i \\ \omega_i \end{bmatrix} \quad (\text{B.8})$$

where  $W_i$  is the total weight of the strip of material lying vertically above discontinuity  $i$ ;  $\bar{p}_i$  is the horizontal distance from the centroid of the strip of material to the mid-point of the discontinuity  $i$  (Figure B.1).

For the specification of live loads, now taking  $\mathbf{u} = \mathbf{0}$ , all live loads can be specified by imposing the following unit displacement constraint  $\mathbf{f}_L^T \mathbf{d} = 1$ .

Therefore, a primal kinematic problem formulation for the plane strain analysis, perfectly plastic cohesive-frictional body discretized using  $m$  discontinuities,  $n$  nodes and a single load case can be stated as follows

$$\min \lambda \mathbf{f}_L^T \mathbf{d} = -\mathbf{f}_D^T \mathbf{d} + \mathbf{g}^T \mathbf{p} \quad (\text{B.9})$$

subject to:

$$\mathbf{B} \mathbf{d} = \mathbf{0} \quad (\text{B.10})$$

$$\mathbf{N} \mathbf{p} - \mathbf{d} = \mathbf{0} \quad (\text{B.11})$$

$$\mathbf{f}_L^T \mathbf{d} = 1 \quad (\text{B.12})$$

$$\mathbf{p} \geq \mathbf{0} \quad (\text{B.13})$$

where  $\mathbf{f}_D$  and  $\mathbf{f}_L$  are respectively vectors of dead and live loads at discontinuities;  $\mathbf{d}$  contains displacements along the discontinuities,  $\mathbf{d}^T = \{s_1, n_1, \omega_1, \dots, \omega_m\}$ , where  $s_i$  and  $n_i$  and  $\omega_i$  are the relative shear and normal and rotational displacements at discontinuity  $i$ ; when rotations are focused within an adjacent soil mass  $\mathbf{g}^T = \{c_1 l_1, c_1 l_1, c_1 l_1^2 u_1 / \tan \phi_1, c_1 l_1^2 u_1 / \tan \phi_1, \dots, c_m l_m^2 u_m / \tan \phi_m\}$ , when rotations are between two uncemented rigid bodies  $\mathbf{g}^T = \{c_1 l_1, c_1 l_1, c_1 l_1^2 \pi / 4, c_1 l_1^2 \pi / 4, \dots, c_m l_m^2 \pi / 4\}$ , where  $l_i$  and  $c_i$  are respectively the length and the cohesive shear strength of discontinuity  $i$ .  $\mathbf{B}$  is a suitable  $(3n \times 3m)$  compatibility matrix;  $\mathbf{N}$  is a suitable  $(3m \times 4m)$  flow matrix; and  $\mathbf{p}$  is a  $(4m)$  vector of plastic multipliers. The discontinuity displacements in  $\mathbf{d}$  and the plastic multipliers in  $\mathbf{p}$  are the LP variables.

## B.2 Dual Problem

In accordance with duality principals, the equations B.8 ~ B.9 of the DLO primal problem can be used to derive the equations of its dual problem. Thus, for a planar body discretized using  $m$  discontinuities and  $n$  nodes, the equations can be stated as follows

$$\max \lambda \quad (\text{B.14})$$

subject to :

$$\mathbf{B}^T \mathbf{t} + \lambda \mathbf{f}_L - \mathbf{q} = -\mathbf{f}_D \quad (\text{B.15})$$

$$\mathbf{N}^T \mathbf{q} \leq \mathbf{g} \quad (\text{B.16})$$

where  $\mathbf{t}^T = \{t_1^x, t_1^y, t_1^\omega, t_2^x, t_2^y, t_2^\omega, \dots, t_n^\omega\}$  and  $t_j^x$  and  $t_j^y$  and  $t_j^\omega$  can be interpreted as horizontal and vertical and rotated direction equivalent nodal forces acting at node  $j$  ( $j = 1, \dots, n$ ); and  $\mathbf{q}$  is a vector of shear and normal forces and moment acting on discontinuities, i.e.  $\mathbf{q}^T = \{S_1, N_1, M_1, S_2, N_2, M_2, \dots, M_m\}$ , where  $S_i$  and  $N_i$  and  $M_i$  represent, respectively, the shear and the normal force and the moment acting on discontinuity  $i$  ( $i = 1, \dots, m$ ). Thus, the LP variables are  $t_j^x, t_j^y, t_j^\omega, S_i$  and  $N_i$  and  $M_i$  and the live load factor  $\lambda$ . The objective is therefore to maximize  $\lambda$  while ensuring that the yield condition is not violated along any potential discontinuity.

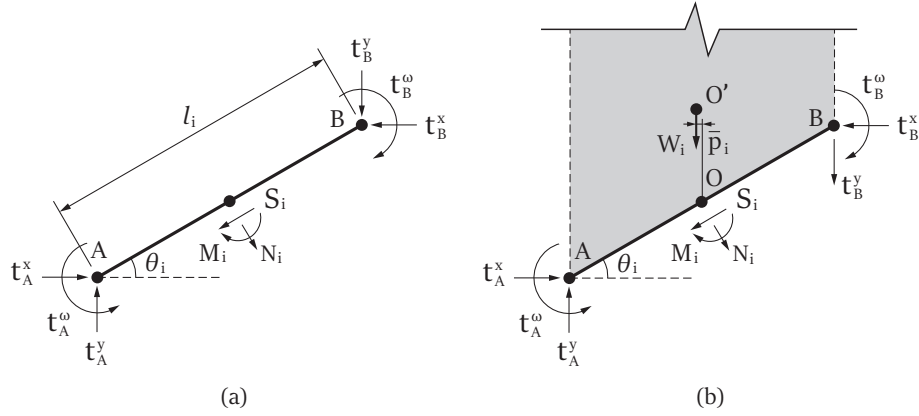


FIGURE B.2: Discontinuity forces in equilibrium with equivalent nodal forces (no external load): (a) excluding external dead loads; (b) including external dead loads

Alternatively, the required equilibrium constraint can be written for a potential discontinuity  $i$  as follows (Figure B.2)

$$\mathbf{B}_i^T \mathbf{t}_i + \lambda \mathbf{f}_{Li} - \mathbf{q}_i = -\mathbf{f}_{Di} \quad (\text{B.17})$$

or in expanded form as

$$\begin{bmatrix} \alpha_i & \beta_i & 0 & -\alpha_i & -\beta_i & 0 \\ -\beta_i & \alpha_i & 0 & \beta_i & -\alpha_i & 0 \\ 0.5l_i\beta_i & -0.5l_i\alpha_i & 1 & 0.5l_i\beta_i & -0.5l_i\alpha_i & -1 \end{bmatrix} \begin{bmatrix} t_A^x \\ t_A^y \\ t_A^\omega \\ t_B^x \\ t_B^y \\ t_B^\omega \end{bmatrix} + \lambda \begin{bmatrix} f_{Li}^s \\ f_{Li}^n \\ f_{Li}^\omega \end{bmatrix} - \begin{bmatrix} S_i \\ N_i \\ M_i \end{bmatrix} = - \begin{bmatrix} f_{Di}^s \\ f_{Di}^n \\ f_{Di}^\omega \end{bmatrix} \quad (\text{B.18})$$

The required yield constraint can also be written for a potential discontinuity  $i$  as follows

$$\mathbf{N}_i^T \mathbf{q}_i \leq \mathbf{g}_i \quad (\text{B.19})$$

or in expanded form for the Mohr–Coulomb yield condition as

$$\begin{bmatrix} 1 & \tan \phi_i & 0 \\ -1 & \tan \phi_i & 0 \\ 0 & u_i l_i & 1 \\ 0 & u_i l_i & -1 \end{bmatrix} \begin{bmatrix} S_i \\ N_i \\ M_i \end{bmatrix} \leq \begin{bmatrix} c_i l_i \\ c_i l_i \\ c_i l_i^2 u_i / \tan \phi_i \\ c_i l_i^2 u_i / \tan \phi_i \end{bmatrix} \quad (\text{B.20})$$



## Appendix C

# Formulations in Anisotropic Stress Distribution

Soil material has both inherent and induced anisotropy. The former is produced by sedimentation and the latter occurs in shear. Degree of the anisotropy is evaluated by means of the deformation modulus ratio  $n = E_x/E_z$ .

In order to evaluate the anisotropic effect  $n$  on the stress in soil body, a simple case of anisotropy is treated herein. Stress solutions in a cross-anisotropic soil shall be derived under plane strain condition. A system of Cartesian coordinates is taken as shown in Figure C.1(a). Consider the case of the principal axis of the material being coincidence with coordinates axis.

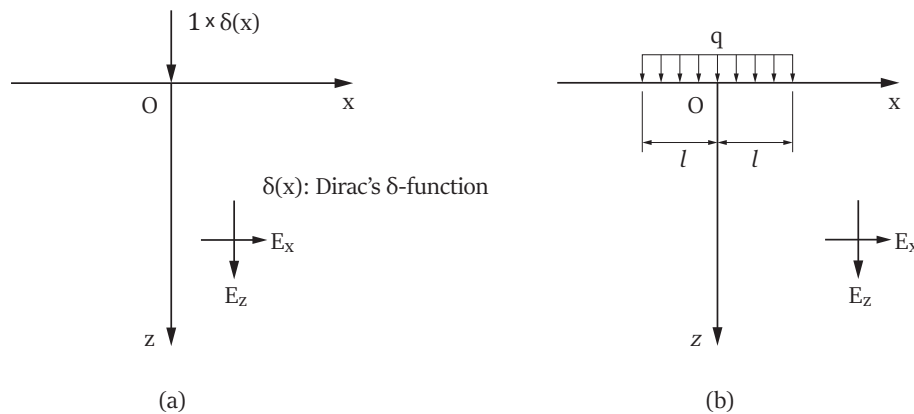


FIGURE C.1: Applied load and coordinates: (a) unit line load; (b) uniformly distributed load

The stress-strain relations are written as follow by neglecting the second order terms with respect to Poisson's ratios

$$\varepsilon_x = \frac{1}{E_x}\sigma_x - \frac{\nu_{zx}}{E_z}\sigma_z, \quad \varepsilon_z = -\frac{\nu_{xz}}{E_x}\sigma_x + \frac{1}{E_z}\sigma_z, \quad \gamma_{xz} = \frac{1}{G_{xz}}\tau_{xz} \quad (\text{C.1})$$

The stresses can be expressed by Airy's stress function  $F$  as

$$\sigma_x = \frac{\partial^2 F}{\partial z^2}, \quad \sigma_z = \frac{\partial^2 F}{\partial x^2}, \quad \tau_{xz} = -\frac{\partial^2 F}{\partial x \partial z} \quad (C.2)$$

The strain compatibility equation is

$$\frac{\partial^2 \varepsilon_z}{\partial x^2} + \frac{\partial^2 \varepsilon_x}{\partial z^2} = \frac{\partial^2 \gamma_{xz}}{\partial x \partial z} \quad (C.3)$$

Substituting equation C.2 into equation C.1 and then into equation C.3 gives

$$\frac{1}{E_z} \frac{\partial^4 F}{\partial x^4} + \left( \frac{1}{G_{xz}} - \frac{\nu_{xz}}{E_x} - \frac{\nu_{zx}}{E_z} \right) \frac{\partial^2 F}{\partial x^2 \partial z^2} + \frac{1}{E_x} \frac{\partial^4 F}{\partial z^4} = 0 \quad (C.4)$$

Assuming  $\frac{\nu_{zx}}{E_z} = \frac{\nu_{xz}}{E_x}$  and using the Barden's assumption which expresses as

$$\frac{1}{G_{xz}} = \frac{1}{E_z} + \frac{1}{E_x} + \frac{2\nu_{zx}}{E_z} \quad (C.5)$$

Substitute equation C.5 into equation C.4, then the compatibility equation reduces to

$$n \frac{\partial^4 F}{\partial x^4} + (n+1) \frac{\partial^4 F}{\partial x^2 \partial z^2} + \frac{\partial^4 F}{\partial z^4} = 0 \quad (C.6)$$

Let the Airy's stress function  $F$  be assumed as follows

$$F = \int_0^\infty f(z, m) \cos mx \, dm \quad (C.7)$$

where  $m$  is a positive parameter. Substituting equation C.7 into equation C.6 gives

$$\frac{d^4 f}{dz^4} - (n+1) \frac{d^2 f}{dz^2} + n f = 0 \quad (C.8)$$

The solution of the differential equation C.8 is obtained as

$$f = B_1 e^{-\eta_1 mz} + B_2 e^{-\eta_2 mz} \quad (C.9)$$

where  $\eta_1$  and  $\eta_2$  are available characteristics roots which are given by  $\eta_1 = \sqrt{n}$ ,  $\eta_2 = 1$ , and  $B_1, B_2$  are constants.

Substituting equation C.9 into equation C.2 gives

$$\sigma_z = \frac{\partial^2 F}{\partial x^2} = - \int_0^\infty (B_1 e^{-\eta_1 mz} + B_2 e^{-\eta_2 mz}) \times m^2 \cos mx \, dm \quad (C.10)$$

$$\sigma_x = \frac{\partial^2 F}{\partial z^2} = \int_0^\infty (B_1 \eta_1^2 e^{-\eta_1 m z} + B_2 e^{-\eta_2 m z}) \times m^2 \cos mx \, dm \quad (\text{C.11})$$

$$\tau_{xz} = -\frac{\partial^2 F}{\partial z^2} = \int_0^\infty (B_1 \eta_1 e^{-\eta_1 m z} + B_2 \eta_2 e^{-\eta_2 m z}) \times m^2 \sin mx \, dm \quad (\text{C.12})$$

In the case that unit load is applied vertically at the origin of the coordinates (Figure C.1(a)), the boundary conditions are as follows

$$\sigma_z|_{z=0} = 1 \times \delta(x) = \frac{1}{\pi} \int_0^\infty \cos mx \, dm \quad (\text{C.13})$$

$$\tau_{xz}|_{z=0} = 0 \quad (\text{C.14})$$

Substituting Equation C.13 into Equation C.10 gives

$$-(B_1 + B_2)m^2 = \frac{1}{\pi} \quad (\text{C.15})$$

Substituting Equation C.14 into Equation C.12 gives

$$\eta_1 B_1 + \eta_2 B_2 = 0 \quad (\text{C.16})$$

Consider the integral of  $e^{ax} \cdot \cos(bx)$  and  $e^{ax} \cdot \sin(bx)$  then derive as

$$\begin{aligned} \int e^{ax} \cdot \cos(bx) dx &= e^{ax} \cdot \frac{1}{b} \sin(bx) - \int \frac{1}{b} \sin(bx) \cdot a \cdot e^{ax} dx \\ &= \frac{e^{ax}}{b} \sin(bx) - \frac{a}{b} \int e^{ax} \cdot \sin(bx) dx \\ &= \frac{e^{ax}}{b^2} \cdot [b \cdot \sin(bx) + a \cdot \cos(bx)] - \frac{a^2}{b^2} \int e^{ax} \cdot \cos(bx) dx \\ &= \frac{e^{ax}}{a^2 + b^2} \cdot [b \cdot \sin(bx) + a \cdot \cos(bx)] + C \end{aligned} \quad (\text{C.17})$$

$$\begin{aligned} \int e^{ax} \cdot \sin(bx) dx &= e^{ax} \cdot \frac{-1}{b} \cos(bx) - \int \frac{-1}{b} \cos(bx) \cdot a \cdot e^{ax} dx \\ &= \frac{-e^{ax}}{b} \cos(bx) + \frac{a}{b} \int e^{ax} \cdot \cos(bx) dx \\ &= \frac{e^{ax}}{b^2} \cdot [-b \cdot \cos(bx) + a \cdot \sin(bx)] - \frac{a^2}{b^2} \int e^{ax} \cdot \sin(bx) dx \\ &= \frac{e^{ax}}{a^2 + b^2} \cdot [a \cdot \sin(bx) - b \cdot \cos(bx)] + C \end{aligned} \quad (\text{C.18})$$

Determining the constants  $B_1$  and  $B_2$  from equations C.15 and C.16, and substituting them into equations C.10, C.11 and C.12 (considering  $a = -\eta_1 z$  or  $-\eta_2 z$  and

$b = x$  in equations C.17 and C.18), then the stresses  $\sigma_z$ ,  $\sigma_x$  and  $\tau_{xz}$  can be calculated.

For  $\sigma_z$  expression, the mathematical derivation is as follows

$$\begin{aligned}
\sigma_z &= - \int_0^\infty (B_1 e^{-\eta_1 m z} + B_2 e^{-\eta_2 m z}) \times m^2 \cos mx \, dm \\
&= \frac{1}{\pi(B_1 + B_2)} \int_0^\infty (B_1 e^{-\eta_1 m z} + B_2 e^{-\eta_2 m z}) \cdot \cos mx \, dm \\
&= \frac{1}{\pi(B_1 + B_2)} \left\{ B_1 \left[ \frac{e^{-\eta_1 z m}}{\eta_1^2 z^2 + x^2} (x \cdot \sin xm - \eta_1 z \cdot \cos xm) \right]_0^\infty \right. \\
&\quad \left. + B_2 \left[ \frac{e^{-\eta_2 z m}}{\eta_2^2 z^2 + x^2} (x \cdot \sin xm - \eta_2 z \cdot \cos xm) \right]_0^\infty \right\} \\
&= \frac{1}{\pi(B_1 + B_2)} \left( \frac{B_1 \eta_1 z}{\eta_1^2 z^2 + x^2} + \frac{B_2 \eta_2 z}{\eta_2^2 z^2 + x^2} \right) \\
&= \frac{1}{\pi(B_1 + B_2)} \frac{\eta_1 \eta_2 z^3 (B_1 \eta_2 + B_2 \eta_1)}{[(\eta_1 z)^2 + x^2] [(\eta_2 z)^2 + x^2]} \tag{C.19} \\
&= \frac{1}{\pi \left( \frac{\eta_2 B_2}{-\eta_1} + B_2 \right)} \frac{\eta_1 \eta_2 z^3 \left( \frac{\eta_2 B_2}{-\eta_1} \eta_2 + B_2 \eta_1 \right)}{[(\eta_1 z)^2 + x^2] [(\eta_2 z)^2 + x^2]} \\
&= \frac{1}{\pi \left( \frac{\eta_2 - \eta_1}{-\eta_1} \right)} \frac{\eta_1 \eta_2 z^3 \left( \frac{\eta_2^2 - \eta_1^2}{-\eta_1} \right)}{[(\eta_1 z)^2 + x^2] [(\eta_2 z)^2 + x^2]} \\
&= \frac{1}{\pi} \frac{\eta_1 \eta_2 z^3 (\eta_2 + \eta_1)}{[(\eta_1 z)^2 + x^2] [(\eta_2 z)^2 + x^2]}
\end{aligned}$$

For  $\sigma_x$  expression, the mathematical derivation gives

$$\begin{aligned}
\sigma_x &= \int_0^\infty (B_1 \eta_1^2 e^{-\eta_1 m z} + B_2 e^{-\eta_2 m z}) \times m^2 \cos mx \, dm \\
&= \frac{-1}{\pi(B_1 + B_2)} \int_0^\infty (B_1 e^{-\eta_1 m z} + B_2 e^{-\eta_2 m z}) \cdot \cos mx \, dm \\
&= \frac{-1}{\pi(B_1 + B_2)} \left\{ B_1 \eta_1^2 \left[ \frac{e^{-\eta_1 z m}}{\eta_1^2 z^2 + x^2} (x \cdot \sin xm - \eta_1 z \cdot \cos xm) \right]_0^\infty \right. \\
&\quad \left. + B_2 \left[ \frac{e^{-\eta_2 z m}}{\eta_2^2 z^2 + x^2} (x \cdot \sin xm - \eta_2 z \cdot \cos xm) \right]_0^\infty \right\} \tag{C.20} \\
&= \frac{-1}{\pi(B_1 + B_2)} \left( \frac{B_1 \eta_1^2 \eta_1 z}{\eta_1^2 z^2 + x^2} + \frac{B_2 \eta_2 z}{\eta_2^2 z^2 + x^2} \right) \\
&= \frac{-1}{\pi(B_1 + B_2)} \frac{z^3 (B_1 \eta_1^3 \eta_2^2 + B_2 \eta_2 \eta_1^2) + x^2 z (B_1 \eta_1^3 + B_2 \eta_2)}{[(\eta_1 z)^2 + x^2] [(\eta_2 z)^2 + x^2]} \\
&= \frac{-1}{\pi(B_1 + B_2)} \frac{z^3 (-B_2 \eta_1^2 \eta_2^3 + B_2 \eta_2 \eta_1^2) + x^2 z (-B_2 \eta_1^2 \eta_2 + B_2 \eta_2)}{[(\eta_1 z)^2 + x^2] [(\eta_2 z)^2 + x^2]}
\end{aligned}$$

Since  $\eta_2 = 1$ , then  $\sigma_x$  in equation C.20 can be simplified as

$$\begin{aligned}
\sigma_x &= \frac{-1}{\pi(B_1 + B_2)} \frac{z^3(-B_2\eta_1^2\eta_2^3 + B_2\eta_2\eta_1^2) + x^2z(-B_2\eta_1^2\eta_2 + B_2\eta_2)}{[(\eta_1z)^2 + x^2][(\eta_2z)^2 + x^2]} \\
&= \frac{-1}{\pi\left(\frac{\eta_2B_2}{-\eta_1} + B_2\right)} \frac{z^3(-B_2\eta_1^2\eta_2^3 + B_2\eta_2\eta_1^2) + x^2z(-B_2\eta_1^2\eta_2 + B_2\eta_2)}{[(\eta_1z)^2 + x^2][(\eta_2z)^2 + x^2]} \\
&= \frac{1}{\pi B_2\left(\frac{\eta_2 - \eta_1}{\eta_1}\right)} \frac{z^3(-B_2\eta_1^2 + B_2\eta_1^2) + x^2zB_2\eta_2(-\eta_1^2 + 1)}{[(\eta_1z)^2 + x^2][(\eta_2z)^2 + x^2]} \tag{C.21} \\
&= \frac{1}{\pi\left(\frac{\eta_2 - \eta_1}{\eta_1}\right)} \frac{x^2z(\eta_2^2 - \eta_1^2)}{[(\eta_1z)^2 + x^2][(\eta_2z)^2 + x^2]} \\
&= \frac{1}{\pi} \frac{\eta_1\eta_2x^2z(\eta_2 + \eta_1)}{[(\eta_1z)^2 + x^2][(\eta_2z)^2 + x^2]}
\end{aligned}$$

For  $\tau_{xz}$  expression, the mathematical derivation gives

$$\begin{aligned}
\tau_{xz} &= \int_0^\infty (B_1\eta_1e^{-\eta_1mz} + B_2\eta_2e^{-\eta_2mz}) \times m^2 \sin mx \, dm \\
&= \frac{-1}{\pi(B_1 + B_2)} \int_0^\infty (B_1e^{-\eta_1mz} + B_2e^{-\eta_2mz}) \cdot \sin mx \, dm \\
&= \frac{-1}{\pi(B_1 + B_2)} \left\{ B_1\eta_1 \left[ \frac{e^{-\eta_1zm}}{\eta_1^2z^2 + x^2} (-\eta_1z \cdot \sin xm - x \cdot \cos xm) \right]_0^\infty \right. \\
&\quad \left. + B_2\eta_2 \left[ \frac{e^{-\eta_2zm}}{\eta_2^2z^2 + x^2} (-\eta_2z \cdot \sin xm - x \cdot \cos xm) \right]_0^\infty \right\} \\
&= \frac{-1}{\pi(B_1 + B_2)} \left( \frac{B_1\eta_1x}{\eta_1^2z^2 + x^2} + \frac{B_2\eta_2x}{\eta_2^2z^2 + x^2} \right) \\
&= \frac{-1}{\pi(B_1 + B_2)} \frac{(B_1\eta_1\eta_2^2z^2x + B_1\eta_1x^3) + (B_2\eta_2\eta_1^2z^2x + B_2\eta_2x^3)}{(\eta_1^2z^2 + x^2)(\eta_2^2z^2 + x^2)} \tag{C.22} \\
&= \frac{-1}{\pi(B_1 + B_2)} \frac{z^2x(B_1\eta_1\eta_2^2 + B_2\eta_2\eta_1^2) + x^3(B_1\eta_1 + B_2\eta_2)}{(\eta_1^2z^2 + x^2)(\eta_2^2z^2 + x^2)} \\
&= \frac{-1}{\pi(B_1 + B_2)} \frac{z^2x(B_1\eta_1\eta_2^2 + B_2\eta_2\eta_1^2)}{(\eta_1^2z^2 + x^2)(\eta_2^2z^2 + x^2)} \\
&= \frac{-1}{\pi(B_1 + B_2)} \frac{z^2x(-B_2\eta_2)(\eta_2^2 - \eta_1^2)}{(\eta_1^2z^2 + x^2)(\eta_2^2z^2 + x^2)} \\
&= \frac{1}{\pi\left(\frac{\eta_2 - \eta_1}{\eta_1}\right)} \frac{z^2x\eta_2(\eta_2^2 - \eta_1^2)}{(\eta_1^2z^2 + x^2)(\eta_2^2z^2 + x^2)} \\
&= \frac{1}{\pi} \frac{\eta_1\eta_2z^2x(\eta_2 + \eta_1)}{[(\eta_1z)^2 + x^2][(\eta_2z)^2 + x^2]}
\end{aligned}$$

Thus the expressions of  $\sigma_z$ ,  $\sigma_x$  and  $\tau_{xz}$  in the case of unit load can be summarised as

$$\begin{cases} \sigma_z = \frac{\eta_1 \eta_2 (\eta_1 + \eta_2)}{\pi} \frac{z^3}{[(\eta_1 z)^2 + x^2][(\eta_2 z)^2 + x^2]} \\ \sigma_x = \frac{\eta_1 \eta_2 (\eta_1 + \eta_2)}{\pi} \frac{x^2 z}{[(\eta_1 z)^2 + x^2][(\eta_2 z)^2 + x^2]} \\ \tau_{xz} = \frac{\eta_1 \eta_2 (\eta_1 + \eta_2)}{\pi} \frac{x z^2}{[(\eta_1 z)^2 + x^2][(\eta_2 z)^2 + x^2]} \end{cases} \quad (\text{C.23})$$

In the case that uniformly load is applied vertically at the  $x$ -direction of the coordinates (Figure C.1(b)), multiplying equation C.23 by  $q \cdot dx$  and integrating from  $(l - x)$  to  $-(l + x)$ , the stress formulae under uniformly distributed load can be derived.

For  $\sigma_z$  expression, the mathematical derivation is as follows

$$\begin{aligned} \sigma_z &= \int_{-(l+x)}^{l-x} \frac{\eta_1 \eta_2 (\eta_1 + \eta_2)}{\pi} \frac{z^3 \cdot q \cdot dx}{[(\eta_1 z)^2 + x^2][(\eta_2 z)^2 + x^2]} \\ &= \frac{\eta_1 \eta_2 (\eta_1 + \eta_2) z^3 \cdot q}{\pi} \int_{-(l+x)}^{l-x} \frac{dx}{[(\eta_1 z)^2 + x^2][(\eta_2 z)^2 + x^2]} \\ &= \frac{q}{\pi} \cdot \frac{1}{\eta_2 - \eta_1} \left[ \eta_2 \cdot \tan^{-1} \left( \frac{x}{\eta_1 z} \right) - \eta_1 \cdot \tan^{-1} \left( \frac{x}{\eta_2 z} \right) \right]_{-(l+x)}^{l-x} \\ &= \frac{q}{\pi} \cdot \frac{1}{\eta_2 - \eta_1} \left\{ \left[ \eta_2 \cdot \tan^{-1} \left( \frac{l-x}{\eta_1 z} \right) - \eta_1 \cdot \tan^{-1} \left( \frac{l-x}{\eta_2 z} \right) \right] \right. \\ &\quad \left. - \left[ \eta_2 \cdot \tan^{-1} \left( \frac{-(l+x)}{\eta_1 z} \right) - \eta_1 \cdot \tan^{-1} \left( \frac{-(l+x)}{\eta_2 z} \right) \right] \right\} \\ &= \frac{q}{\pi} \cdot \frac{1}{\eta_2 - \eta_1} \left\{ \eta_2 \left[ \tan^{-1} \left( \frac{l-x}{\eta_1 z} \right) - \tan^{-1} \left( \frac{-(l+x)}{\eta_1 z} \right) \right] \right. \\ &\quad \left. - \eta_1 \left[ \tan^{-1} \left( \frac{l-x}{\eta_2 z} \right) - \tan^{-1} \left( \frac{-(l+x)}{\eta_2 z} \right) \right] \right\} \\ &= \frac{q}{\pi} \cdot \frac{1}{\eta_2 - \eta_1} \left\{ \eta_2 \cdot \tan^{-1} \left[ \frac{\frac{l-x}{\eta_1 z} - \frac{-(l+x)}{\eta_1 z}}{1 + \frac{l-x}{\eta_1 z} \cdot \frac{-(l+x)}{\eta_1 z}} \right] \right. \\ &\quad \left. - \eta_1 \cdot \tan^{-1} \left[ \frac{\frac{l-x}{\eta_2 z} - \frac{-(l+x)}{\eta_2 z}}{1 + \frac{l-x}{\eta_2 z} \cdot \frac{-(l+x)}{\eta_2 z}} \right] \right\} \\ &= \frac{q}{\pi} \cdot \frac{1}{\eta_2 - \eta_1} \left[ \eta_2 \tan^{-1} \frac{2l\eta_1 z}{(\eta_1 z)^2 + x^2 - l^2} - \eta_1 \tan^{-1} \frac{2l\eta_2 z}{(\eta_2 z)^2 + x^2 - l^2} \right] \end{aligned} \quad (\text{C.24})$$

For  $\sigma_x$  expression, the mathematical derivation gives

$$\begin{aligned}
\sigma_x &= \int_{-(l+x)}^{l-x} \frac{\eta_1 \eta_2 (\eta_1 + \eta_2)}{\pi} \frac{zx^2 \cdot q \cdot dx}{[(\eta_1 z)^2 + x^2][(\eta_2 z)^2 + x^2]} \\
&= \frac{\eta_1 \eta_2 (\eta_1 + \eta_2) z \cdot q}{\pi} \int_{-(l+x)}^{l-x} \frac{x^2 \cdot dx}{[(\eta_1 z)^2 + x^2][(\eta_2 z)^2 + x^2]} \\
&= \frac{q}{\pi} \cdot \frac{\eta_1 \eta_2}{\eta_2 - \eta_1} \left[ -\eta_1 \cdot \tan^{-1} \left( \frac{x}{\eta_1 z} \right) + \eta_2 \cdot \tan^{-1} \left( \frac{x}{\eta_2 z} \right) \right]_{-(l+x)}^{l-x} \\
&= \frac{q}{\pi} \cdot \frac{\eta_1 \eta_2}{\eta_2 - \eta_1} \left\{ -\eta_1 \left[ \tan^{-1} \left( \frac{l-x}{\eta_1 z} \right) - \tan^{-1} \left( \frac{-(l+x)}{\eta_1 z} \right) \right] \right. \\
&\quad \left. + \eta_2 \left[ \tan^{-1} \left( \frac{l-x}{\eta_2 z} \right) - \tan^{-1} \left( \frac{-(l+x)}{\eta_2 z} \right) \right] \right\} \tag{C.25} \\
&= \frac{q}{\pi} \cdot \frac{\eta_1 \eta_2}{\eta_2 - \eta_1} \left\{ -\eta_1 \cdot \tan^{-1} \left[ \frac{\frac{l-x}{\eta_1 z} - \frac{-(l+x)}{\eta_1 z}}{1 + \frac{l-x}{\eta_1 z} \cdot \frac{-(l+x)}{\eta_1 z}} \right] \right. \\
&\quad \left. + \eta_2 \cdot \tan^{-1} \left[ \frac{\frac{l-x}{\eta_2 z} - \frac{-(l+x)}{\eta_2 z}}{1 + \frac{l-x}{\eta_2 z} \cdot \frac{-(l+x)}{\eta_2 z}} \right] \right\} \\
&= \frac{q}{\pi} \cdot \frac{\eta_1 \eta_2}{\eta_2 - \eta_1} \left[ -\eta_1 \tan^{-1} \frac{2l\eta_1 z}{(\eta_1 z)^2 + x^2 - l^2} + \eta_2 \tan^{-1} \frac{2l\eta_2 z}{(\eta_2 z)^2 + x^2 - l^2} \right]
\end{aligned}$$

For  $\tau_{xz}$  expression, the mathematical derivation gives

$$\begin{aligned}
\tau_{xz} &= \int_{-(l+x)}^{l-x} \frac{\eta_1 \eta_2 (\eta_1 + \eta_2)}{\pi} \frac{z^2 x \cdot q \cdot dx}{[(\eta_1 z)^2 + x^2][(\eta_2 z)^2 + x^2]} \\
&= \frac{\eta_1 \eta_2 (\eta_1 + \eta_2) z^2 \cdot q}{\pi} \int_{-(l+x)}^{l-x} \frac{x \cdot dx}{[(\eta_1 z)^2 + x^2][(\eta_2 z)^2 + x^2]} \\
&= \frac{q}{2\pi} \cdot \frac{\eta_1 \eta_2}{\eta_2 - \eta_1} \left[ \ln \frac{(\eta_1 z)^2 + x^2}{(\eta_2 z)^2 + x^2} \right]_{-(l+x)}^{l-x} \\
&= \frac{q}{\pi} \cdot \frac{\eta_1 \eta_2}{\eta_2 - \eta_1} \left\{ -\eta_1 \left[ \tan^{-1} \left( \frac{l-x}{\eta_1 z} \right) - \tan^{-1} \left( \frac{-(l+x)}{\eta_1 z} \right) \right] \right. \\
&\quad \left. + \eta_2 \left[ \tan^{-1} \left( \frac{l-x}{\eta_2 z} \right) - \tan^{-1} \left( \frac{-(l+x)}{\eta_2 z} \right) \right] \right\} \tag{C.26} \\
&= \frac{q}{\pi} \cdot \frac{\eta_1 \eta_2}{\eta_2 - \eta_1} \left\{ -\eta_1 \cdot \tan^{-1} \left[ \frac{\frac{l-x}{\eta_1 z} - \frac{-(l+x)}{\eta_1 z}}{1 + \frac{l-x}{\eta_1 z} \cdot \frac{-(l+x)}{\eta_1 z}} \right] \right. \\
&\quad \left. + \eta_2 \cdot \tan^{-1} \left[ \frac{\frac{l-x}{\eta_2 z} - \frac{-(l+x)}{\eta_2 z}}{1 + \frac{l-x}{\eta_2 z} \cdot \frac{-(l+x)}{\eta_2 z}} \right] \right\} \\
&= \frac{q}{2\pi} \cdot \frac{\eta_1 \eta_2}{\eta_2 - \eta_1} \cdot \ln \left[ \frac{(l+x)^2 + (\eta_1 z)^2}{(l+x)^2 + (\eta_2 z)^2} \cdot \frac{(l-x)^2 + (\eta_2 z)^2}{(l-x)^2 + (\eta_1 z)^2} \right]
\end{aligned}$$

Thus the expressions of  $\sigma_z$ ,  $\sigma_x$  and  $\tau_{xz}$  in the case of uniformly load can be summarised as

$$\left\{ \begin{array}{l} \sigma_z = \frac{q}{\pi} \frac{1}{\eta_2 - \eta_1} \left[ \eta_2 \tan^{-1} \frac{2l\eta_1 z}{(\eta_1 z)^2 + x^2 - l^2} - \eta_1 \tan^{-1} \frac{2l\eta_2 z}{(\eta_2 z)^2 + x^2 - l^2} \right] \\ \sigma_x = \frac{q}{\pi} \frac{\eta_1 \eta_2}{\eta_2 - \eta_1} \left[ -\eta_1 \tan^{-1} \frac{2l\eta_1 z}{(\eta_1 z)^2 + x^2 - l^2} + \eta_2 \tan^{-1} \frac{2l\eta_2 z}{(\eta_2 z)^2 + x^2 - l^2} \right] \\ \tau_{xz} = \frac{q}{2\pi} \frac{\eta_1 \eta_2}{\eta_2 - \eta_1} \ln \left[ \frac{(l+x)^2 + (\eta_1 z)^2}{(l+x)^2 + (\eta_2 z)^2} \cdot \frac{(l-x)^2 + (\eta_2 z)^2}{(l-x)^2 + (\eta_1 z)^2} \right] \end{array} \right. \quad (\text{C.27})$$

## Appendix D

# Formulations in Lateral Earth Pressure Coefficient

In accordance with lower bound theorems, a combined stress fields must not yield. The conventional Mohr-Coulomb yield condition is considered and can be expressed as

$$\frac{(\sigma_1 + \sigma_3)}{2} \sin \phi = \frac{(\sigma_1 - \sigma_3)}{2} - c \cos \phi \quad (D.1)$$

where

$$\begin{cases} \sigma_1 = \frac{1}{2}(\sigma_x + \sigma_z) + \sqrt{\frac{1}{4}(\sigma_x - \sigma_z)^2 + \tau_{xz}^2} \\ \sigma_3 = \frac{1}{2}(\sigma_x + \sigma_z) - \sqrt{\frac{1}{4}(\sigma_x - \sigma_z)^2 + \tau_{xz}^2} \end{cases} \quad (D.2)$$

The 'Boussinesq' stress fields and backfill self-weight stresses can be combined to generate a stress field. The combined vertical stress  $\sigma_z$ , horizontal stress  $\sigma_x$  and shear stress  $\tau_{xz}$  can be given by

$$\begin{cases} \sigma_z = \Delta\sigma_z + \gamma z \\ \sigma_x = \Delta\sigma_x + K(z)\gamma z \\ \tau_{xz} = \Delta\tau_{xz} \end{cases} \quad (D.3)$$

Introduce two parameters as follows

$$\begin{cases} D_1 = \Delta\sigma_x + \Delta\sigma_z \\ D_2 = \Delta\sigma_x - \Delta\sigma_z \end{cases} \quad (D.4)$$

To automatically compute required lateral earth pressure coefficient  $K(z)$ , it can be derived by substituting equations D.3 and D.4 into equation D.1, using  $c = 0$ , then

$$\frac{1}{2}[D_1 + (K + 1)\gamma z] \sin \phi = \sqrt{\frac{1}{4}[D_2 + (K - 1)\gamma z]^2 + \Delta\tau_{xz}^2} \quad (D.5)$$

Equation (D.5) can be rewritten as

$$\begin{aligned} & [D_1^2 + 2D_1(K + 1)\gamma z + (K + 1)^2\gamma^2 z^2] \sin^2 \phi \\ & = [D_2^2 + 2D_2(K - 1)\gamma z + (K - 1)^2\gamma^2 z^2] + 4\Delta\tau_{xz}^2 \end{aligned} \quad (D.6)$$

expanding,

$$\begin{aligned} & D_1^2 \sin^2 \phi + K(2D_1\gamma z \sin^2 \phi) + 2D_1\gamma z \sin^2 \phi + K^2(\gamma^2 z^2 \sin^2 \phi) \\ & + K(2\gamma^2 z^2 \sin^2 \phi) + \gamma^2 z^2 \sin^2 \phi = D_2^2 + K(2D_2\gamma z) - 2D_2\gamma z \\ & + K^2(\gamma^2 z^2) - K(2\gamma^2 z^2) + \gamma^2 z^2 + 4\Delta\tau_{xz}^2 \end{aligned} \quad (D.7)$$

Combining similar terms, equation (D.7) can be written as

$$\begin{aligned} & K^2(\gamma^2 z^2 \sin^2 \phi - \gamma^2 z^2) + K(2D_1\gamma z \sin^2 \phi + 2\gamma^2 z^2 \sin^2 \phi \\ & - 2D_2\gamma z + 2\gamma^2 z^2) + (D_1^2 \sin^2 \phi + 2D_1\gamma z \sin^2 \phi + \gamma^2 z^2 \sin^2 \phi \\ & - \gamma^2 z^2 - D_2^2 + 2D_2\gamma z - 4\Delta\tau_{xz}^2) = 0 \end{aligned} \quad (D.8)$$

The coefficients of equation (D.8) in  $K^2$ ,  $K$  and 1 can be given as

$$\begin{cases} \psi = \gamma^2 z^2 (\sin^2 \phi - 1) \\ \chi = 2\gamma^2 z^2 (\sin^2 \phi + 1) + 2\gamma z (D_1 \sin^2 \phi - D_2) \\ \kappa = \gamma^2 z^2 (\sin^2 \phi - 1) + 2\gamma z (D_1 \sin^2 \phi + D_2) + D_1 \sin^2 \phi - D_2^2 - 4\Delta\tau_{xz}^2 \end{cases} \quad (D.9)$$

Then solve equation (D.8), and obtain the lateral earth pressure coefficient expression at any depth

$$K(z) = \frac{-\chi \pm \sqrt{\chi^2 - 4\psi\kappa}}{2\psi} \quad (D.10)$$